AVERTISSEMENT

Ce document est le fruit d'un long travail approuvé par le jury de soutenance et mis à disposition de l'ensemble de la communauté universitaire élargie.

Il est soumis à la propriété intellectuelle de l'auteur. Ceci implique une obligation de citation et de référencement lors de l'utilisation de ce document.

D'autre part, toute contrefaçon, plagiat, reproduction illicite encourt une poursuite pénale.

Contact : ddoc-theses-contact@univ-lorraine.fr

LIENS

Code de la Propriété Intellectuelle. articles L 122. 4
Code de la Propriété Intellectuelle. articles L 335.2- L 335.10
http://www.cfcopies.com/V2/leg/leg_droi.php
http://www.culture.gouv.fr/culture/infos-pratiques/droits/protection.htm

UNIVERSITÉ DE LORRAINE NORTHEASTERN UNIVERSITYSITY

# DISSERTATION

## Presented at
## Université de Lorraine and Northeastern University

**Bo YANG 杨 波**

**To obtain the doctor’s degree of**
**University of Lorraine and Northeastern University**

SPECIAL FIELD: Engineering Sciences
OPTION: Materials Science

# *Fabrication and crystallographic features of epitaxial NiMnGa ferromagnetic shape memory alloy thin films*

**Defended on the 1st August, 2014 in front of the jury:**

| | | | |
|---|---|---|---|
| Tadao WATANABE | Professor | Tohoku University, Japan | Reviewer& Jury member |
| Zhidong ZHANG | Professor | Institute of metal research, Chinese academy of sciences, China | Reviewer& Jury member |
| Zhanjie WANG | Professor | Institute of metal research, Chinese academy of sciences, China | Jury member |
| Claude ESLING | Professor | Université de Lorraine, France | Supervisor |
| Liang ZUO | Professor | Northeastern University, China | Supervisor |
| Philippe MARTINEAU | Doctor | Service pour la Science et la Technologie Ambassade de France en Chine, France | Jury member |
| Yudong ZHANG | Doctor HDR | Université de Lorraine, France | Co-Supervisor |
| Gaowu QIN | Professor | Northeastern University, China | Co-Supervisor |

Laboratoire d'Étude des Microstructures et de Mécanique des Matériaux, LEM3
Ile du Saulcy 57012 Metz Cedex 1

# Acknowledgements

This work is supported by the Sino-French Cai Yuanpei Program (N°24013QG), the Northeastern University Research Foundation for Excellent Doctor of Philosophy Candidates (No. 200904), and the French State through the program "Investment in the future" operated by the National Research Agency (ANR) and referenced by ANR-11-LABX-0008-01 (LabEx DAMAS). The work presented in this thesis is completed at LEM3 (former LETAM, University of Lorraine, France) and the Key Laboratory for Anisotropy and Texture of Materials (Northeastern University, China). I had the honor to work with numerous colleagues in two labs and I would like to give my hearted thanks for their kind help.

First of all, I would like to sincerely appreciate all the jury members for taking time out of their busy schedules to achieve the defense of my dissertation. Special gratitude was expressed to Professor Tadao WATANABE and Professor Zhidong ZHANG for their evaluation of my dissertation and for the constructive suggestions and comments.

I sincerely extend my deepest gratitude to my advisors, Professor Claude Esling, Dr. Yudong Zhang at University of Lorraine, Professor Liang Zuo and Professor Gaowu QIN at Northeastern University, who granted me this project. Without their endless encouragement and support this work would not have been completed. I have benefitted tremendously from their knowledge and experiences, their persistence and strive for excellence. I would like to express special appreciations to Dr. Yudong Zhang and Professor Gaowu QIN for their constant and selfless help in my academic study and daily life.

I would like to express my gratefulness to Dr. Perroud Olivier for his technical assistance, especially with X-ray diffraction. I would like to express my appreciation to Dr. Zongbin LI for his helpful and inspiring discussions as he shared his knowledge on ferromagnetic shape memory alloys with me.

I am grateful to all the staffs and students who shared their experiences with me and offered helps to my study, including Dr. Yuping REN, Dr. Song LI, Dr. Na XIAO, Dr. Jing BAI, Ms Nan XU, Ms Shiying WANG, Dr. Zhangzhi SHI, Mr. Haile YAN, Ms Xiaorui LIU, and Ms. Jianshen WANG.

Last but not least, I would like to thank my parents who have loved, supported and

trusted me throughout my life. I always feel very lucky being their son. Also, I would like to thank to my sister for her endless support throughout my life. I feel happy knowing that my family supports me and loves me unconditionally.

# Abstract

Epitaxial Ni-Mn-Ga thin films have attracted considerable attention, since they are promising candidates for magnetic sensors and actuators in micro-electro-mechanical systems. Comprehensive information on the microstructural and crystallographic features of the NiMnGa films and their relationship with the constraints of the substrate is essential for further property optimization. In the present work, epitaxial Ni-Mn-Ga thin films were produced by DC magnetron sputtering and then characterized by x-ray diffraction technique (XRD) and backscatter electron diffraction equipped in scanning electron microscope (SEM-EBSD).

Epitaxial NiMnGa thin films with nominal composition of $Ni_{50}Mn_{30}Ga_{20}$ and thickness of 1.5 μm were successfully fabricated on MgO monocrystalline substrate by DC magnetron sputtering, after the optimization of sputtering parameters such as sputtering power, substrate temperature and seed layer by the present work.

XRD diffraction measurements demonstrate that the epitaxial NiMnGa thin films are composed of three phases: austenite, NM martensite and 7M martensite. With the optimized measurement geometries, maximum number of diffraction peaks of the concerning phases, especially of the low symmetrical 7M martensite, are acquired and analyzed. The lattice constants of all the three phases under the constraints of the substrate in the films are fully determined. These serve as prerequisites for the subsequent EBSD crystallographic orientation characterizations.

SEM-EBSD in film depth analyses further verified the co-existence situation of the three constituent phases: austenite, 7M martensite and NM martensite. NM martensite is located near the free surface of the film, austenite above the substrate surface, and 7M martensite in the intermediate layers between austenite and NM martensite.

Microstructure characterization shows that both the 7M martensite and NM martensite are of plate morphology and organized into two characteristic zones featured with low and high relative second electron image contrast. Local martensite plates with similar plate morphology orientation are organized into plate groups or groups or variant colonies.

Further EBSD characterization indicates that there are four distinct martensite plates in each variant groups for both NM and 7M martensite. Each NM martensite plate is composed of paired major and minor lamellar variants in terms of their thicknesses having a coherent interlamellar interface, whereas, each 7M martensite plate contains one orientation variant. Thus, there are four orientation 7M martensite variants and eight orientation NM martensite variants in one variant group.

According to the crystallographic orientation of martensites and the crystallographic calculation, for NM martensite, the inter-plate interfaces are composed of compound twins in adjacent NM plates. The symmetrically distribution of compound twins results in the long and straight plate interfaces in the low relative contrast zone. The asymmetrically distribution leads to the change of inter-plate interface orientation in the high relative contrast zone.

For 7M martensite, both Type-I and Type-II twin interfaces are nearly perpendicular to the substrate surface in the low relative contrast zones. The Type-I twin pairs appear with much higher frequency, as compared with that of the Type-II twin pairs. However, there are two Type-II twin interface trace orientations and one Type-I twin interface trace orientation in the high relative contrast zones. The Type-II twin pairs are more frequent than the Type-I twin pairs. The inconsistent occurrences of the different types of twins in different zones are originated from the substrate constrain.

The crystallographic calculation also indicates that the martensitic transformation sequence is from Austenite to 7M martensite and then transform into NM martensite (A→7M→NM). The present study intends to offer deep insights into the crystallographic features and martensitic transformation of epitaxial NiMnGa thin films.

***Keywords:*** ferromagnetic shape memory alloys (FSMAs); Ni-Mn-Ga thin films; martensitic transformation; EBSD; misorientation; Texture

# Résumé

Les couches minces épitaxiales de Ni-Mn-Ga ont attiré une attention considérable, car ils sont des candidats prometteurs pour les capteurs et actionneurs magnétiques dans des microsystèmes électromécaniques. Des informations complètes sur les caractéristiques de la microstructure et de la cristallographie des films NiMnGa et leur relation avec les contraintes du substrat sont essentielles à l'optimisation des propriétés. Dans le présent travail, les couches minces épitaxiale de Ni-Mn-Ga ont été produites par pulvérisation cathodique magnétron à courant continu et ensuite caractérisées par la technique de diffraction des rayons X (XRD) et la diffraction d'électrons rétrodiffusés dans un microscope électronique à balayage équipé d'analyse EBSD (MEB-EBSD).

Des couches minces épitaxiales avec NiMnGa de composition nominale $Ni_{50}Mn_{30}Ga_{20}$ et d'épaisseur 1,5 µm ont été fabriquées avec succès sur le substrat monocristallin de MgO par pulvérisation cathodique magnétron DC, après l'optimisation des paramètres tels que la puissance de pulvérisation cathodique, la température du substrat et de la couche d'ensemencement dans le cadre du présent travail.

Les mesures de diffraction DRX montrent que les couches minces épitaxiales NiMnGa sont composées de trois phases: austénite, martensite NM et martensite modulée 7M. Avec les géométries de mesure optimisées, le nombre maximum possible de pics de diffraction des phases relatives, en particulier compte tenu de la basse symétrie de la martensite 7M, sont acquis et analysés. Les constantes de réseau de l'ensemble des trois phases dans le cadre des contraintes du substrat dans les films sont entièrement déterminées.

L'analyse SEM-EBSD en profondeur du film a permis en outre de vérifier la situation de coexistence de trois phases constitutives: austénite, 7M martensite et martensite NM. La martensite NM se trouve près de la surface libre du film, l'austénite au-dessus de la surface du substrat, et la martensite 7M dans les couches intermédiaires entre l'austénite et la martensite NM. La caractérisation de microstructure montre que la martensite 7M et la martensite NM ont une morphologie de plaque et sont organisées en deux zones caractéristiques décrites avec des bas et haut contraste en images d'électrons secondaires. Des plaques de martensite locales similaire en orientation morphologique sont organisées en groupes de plaques ou colonies ou variantes de colonies.

Une caractérisation plus poussée en EBSD indique qu'il existe quatre plaques de martensite distinctes dans chaque colonie de variante à la fois pour la martensite NM et 7M. Chaque plaque de martensite NM est composée de variantes lamellaires majeures et mineures en termes d’épaisseurs appariées et ayant une interface interlamellaire cohérente, alors que chaque plaque de martensite 7M contient une variante d'orientation. Ainsi, il existe quatre variantes d'orientation de martensite 7M et huit variantes d’orientation de martensite NM dans une colonie de variantes.

Selon l'orientation cristallographique des martensites et des calculs cristallographiques, pour la martensite NM, les interfaces inter-plaques sont constituées de macles de type composées dans des plaques adjacentes de martensite NM. La distribution symétrique des macles composées résulte dans des interfaces de plaques longues et droites dans la zone de contraste relatif faible. La répartition asymétrique conduit à la modification de l’orientation d'interface entre les plaques de la zone de contraste relativement élevéPour la martensite 7M, à la fois les interfaces de type I et de type II sont à peu près perpendiculaires à la surface du substrat dans les zones à faible contraste relatif. Les paires de macles de type-I apparaissent avec une fréquence beaucoup plus élevée, par comparaison avec celle des macles de type II. Cependant, il ya deux traces d’interface de macles de type II et une trace d’interface de macles de type I dans les zones de contraste relatifs élevés. Les paires de macles de type II sont plus fréquentes que les paires de macles de type-I. Les apparitions incohérentes des différents types de macles dans les différentes zones sont dues à la contrainte du substrat.

Le calcul cristallographique montre également que la séquence de la transformation martensitique est d'austénite en martensite 7M qui est ensuite transformée en martensite NM (A →7M→NM). La présente étude se propose d'offrir une étude approfondie des caractéristiques cristallographiques et de la transformation martensitique de films minces de NiMnGa préparés par épitaxie.

***Mots clés:*** Alliages ferromagnétique à mémoire de forme (FSMAs); Films minces de Ni-Mn-Ga; transformation martensitique; EPCA; désorientation; texture。

# 摘 要

NiMnGa 薄膜是微机电系统中微传感器和微驱动器的优选材料，已经引起了许多研究者的广泛关注。然而，目前制备出的 NiMnGa 薄膜中包含多种晶体结构的相、多种取向的马氏体变体和复杂的微观组织，导致其很难获得较大的磁场诱发应变。揭示 NiMnGa 薄膜中微观组织与晶体学取向之间的内在联系、探究 NiMnGa 薄膜中马氏体相变过程，是通过训练消除不利的马氏体变体，获得较大磁场诱发应变的前提。但是，NiMnGa 薄膜中的马氏体板条尺寸远远小于块体材料的板条尺寸，使得马氏体相的晶体学取向表征异常困难，因此在 NiMnGa 薄膜种，局部马氏体变体的详细取向信息尚未报道。本论文针对这一科学难题，利用 X-射线衍射（XRD），扫描电镜，电子背散射衍射（EBSD）和透射电镜（TEM），对外延生长 NiMnGa 薄膜进行了系统全面的晶体学分析和研究。结果如下：

首先，通过调控磁控溅射的工艺参数（溅射功率、气压、基板温度），薄膜的成分、厚度等，成功制备出柱状晶和强取向的外延生长 NiMnGa 薄膜。由于柱状晶薄膜的晶界会限制磁诱导形状变化的效果，导致其磁场诱发应变受到限制，因此本论文重点研究外延生长 NiMnGa 薄膜。

XRD 结果表明，外延生长 NiMnGa 薄膜由奥氏体、非调制马氏体（NM）和七层调制马氏体（7M）三相组成。其中七层调制马氏体的晶体结构为单斜结构。在薄膜中，七层调制马氏体有三种择优取向的马氏体变体，分别是 $(2\,0\,\overline{20})_{\mathrm{mono}}$，$(2\,0\,20)_{\mathrm{mono}}$ 和 $(0\,4\,0)_{\mathrm{mono}}$ 面平行于基板平面。非调制马氏体具有两种择优取向的马氏体变体，分别是 $(220)_{\mathrm{Tetr}}$ 和 $(004)_{\mathrm{Tetr}}$ 平行于基板平面。

扫描电镜的微观照片表面薄膜由两种特征组织组成：一种是平行于基板边界的平直马氏体板条，另一种是与基板边界成 45°夹角的弯曲马氏体板条。利用控制厚度的电解抛光技术研究薄膜微观组织随厚度的变化发现：随着抛光时间的延长，薄膜马氏体板条的宽度突然降低。这表明在表层部分为粗大的马氏体板条，底层靠近基板的部分为细小的马氏体板条，少量残余奥氏体与基板接触。通过分析 EBSD 的 Kikuchi 花样，发现表层粗大的马氏体板条为 NM 马氏体，底层细小的马氏体板条为 7 层调制马氏体结构。

每个马氏体变体团由 4 种不同取向的马氏体板条组成，且每个板条中由两种取向的

NM 马氏体变体或一种取向的 7M 马氏体变体。因此，在每个马氏体变体团中共有 8 种取向的 NM 马氏体变体，或者 4 种取向的 7M 马氏体变体。

根据 EBSD 获得马氏体变体的取向和晶体学计算可知，在一个板条内部的两个 NM 马氏体变体为复合孪生关系。在平直的低反差区域，复合孪生的 NM 马氏体变体关于板条界面对称分布。然而在弯曲的高反差区域，复合孪生的 NM 马氏体变体关于板条界面不对称分布。对于七层调制马氏体，在平直的低反差区域，一型孪晶界面占据主要板条界面，在弯曲的高反差区域，二型孪晶界面占据主要板条界面。形成这种分布的原因是由于在相变过程中这两个区域受到基板的阻碍不同。

深入的 EBSD 研究结果表明，在 NiMnGa 薄膜中存在 6 个 NM 马氏体变体团，每个 NM 马氏体变体团有 8 种 NM 马氏体变体，因此在整个 NiMnGa 薄膜中，有 48 种不同取向的 NM 马氏体变体。对于 7M 马氏体，同样存在 6 个变体团，不过每个变体团有 4 种取向的 7M 马氏体变体，总共有 24 种取向的 7M 马氏体变体。这说明，NiMnGa 薄膜中 NM 马氏体变体必须经过 7M 才能获得 48 个变体。每种 7M 马氏体变体转变为两种取向的 NM 马氏体变体。

综上所述，本研究给出了 NiMnGa 薄膜中马氏体变体取向分布与微观组织之间的内在联系，并验证了马氏体相变和中间马氏体相变的晶体学取向关系，更进一步丰富了 NiMnGa 合金中的马氏体相变理论。

**关键词**：铁磁形状记忆合金；NiMnGa 薄膜；马氏体相变；电子背散射衍射；取向关系；织构

# Contents

# Chapter 1 Introduction

## 1.1 General introduction

The miniaturization of electronic systems and the increase of their functionality require the implementation of active and sensitive devices on a small scale [1]. Micro-electro-mechanical systems (MEMS) or nano-electro-mechanical systems (NEMS) are one of the potential technologies for decreasing size of these devices and have been established in wide domains such as information technology, automotive, aerospace and bio-medical applications [2, 3]. Developing excellent active and sensitive materials are of technological interest and also represent dominating challenges for the design of MEMS and NEMS. In particular, active and sensitive materials that can exhibit large strains with rapid response (also referred to smart materials) are desirable [4, 5].

A number of active materials such as magnetostrictive materials, piezoelectric ceramics and shape memory alloys that show a few percent strains under an applied external field have been proposed as these kinds of actuator and sensor materials [6-11]. Among the numerous advanced materials, the ferromagnetic shape memory alloys (FSMAs), also referred to magnetic shape memory alloys (MSMAs), are a group of fascinating material, which can provide a significant and reversible strain at high frequency driven by external magnetic field [12-18]. FSMAs not only overcome the low potential efficiency of thermally controlled shape memory actuators, but also exhibit much larger output strains than those of the magnetostrictive, the piezoelectric or the electrostrictive materials. The unique properties of FSMAs have attracted extensive research interest during the past few years.

The discovery of ferromagnetic Ni-Mn-based Heusler alloys quickly promoted a breakthrough in the application of ferromagnetic shape memory alloys [19-21]. To date, magnetic field induced strain as high as 12% has been achieved recently in the bulk NiMnGa single crystals. Whereas, although extensive research has been centered on bulk polycrystalline NiMnGa alloys to understand their mechanical, magnetic properties and phase transformation behaviors [22-32], magnetic field induced strains in bulk NiMnGa polycrystals are still in the magnitude order of 1%, owing to the complex microstructure. In addition, bulk NiMnGa alloys are very brittle in polycrystalline state, making them difficult to deform into desirable shape.

Ductility can be improved in a single crystal or thin film form. NiMnGa thin films deposited with various physical vapor deposition methods have shown superior mechanical properties [3, 33-41]. However, most of the as-deposited NiMnGa thin films are composed of complex microstructure and several phases, which are the main obstacles to achieve huge magnetic field induced strain [42-47]. Revelation of the local crystallographic orientation and interfaces between microstructural constituents in epitaxial NiMnGa thin films have been an essential issue, in order to provide useful guidance for post treatments to eliminate the undesired martensite variants [48-52].

## 1.2 Ferromagnetic shape memory effect

Of all shape memory effects discovered, magnetic field induced shape memory effect is the most conducive to application, due to its high response frequency and giant actuation strain. The nature of giant magnetic-field-induced strain is due to either orientation rearrangements of martensite variants or the structural transition of these materials [18, 53, 54].

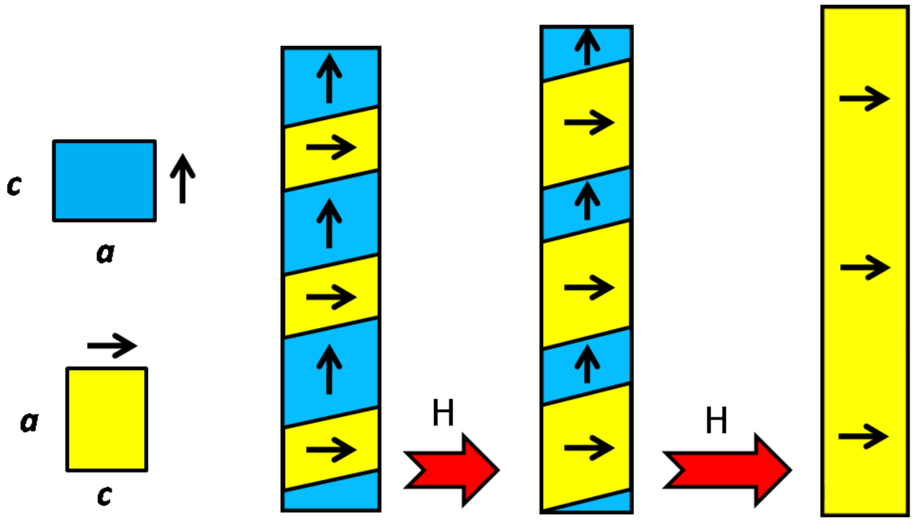

**Fig.1.1** Schematic illustration of the magnetic field induced deformation due to the rearrangements of martensite variants.

Orientation rearrangements of martensite variants, also referred to magnetic field induced re-orientation, is based on magnetostructural coupling which takes advantage of the larger uniaxial magnetocrystalline anisotropy of the martensite phase [18, 55]. Normally, the *c*-axis (short axis) is the easy axis in the modulated martensites, while it is the hard-axis in non-modulated martensite which displays easy magnetization planes perpendicular to the *c*-axis. As shown Fig.1.1, in the practical materials, twin variants in martensite have magnetic moments in different directions. On the application of magnetic field, the variants that are not aligned with the applied field, will de-twin to align their moments with the external magnetic field. This movement results in a macroscopic change in length resulting in strain.

The unique mechanism of magnetic field induced reorientation has been observed in NiMnGa alloys [55, 56]. Fig.1.2 shows magnetic field-induced variant rearrangement occurring in a rectangular bar specimen under the applied field along the [100] direction of the specimen. The twinned microstructure is visible using polarized microscopy on a polished (001) surface of the specimen.

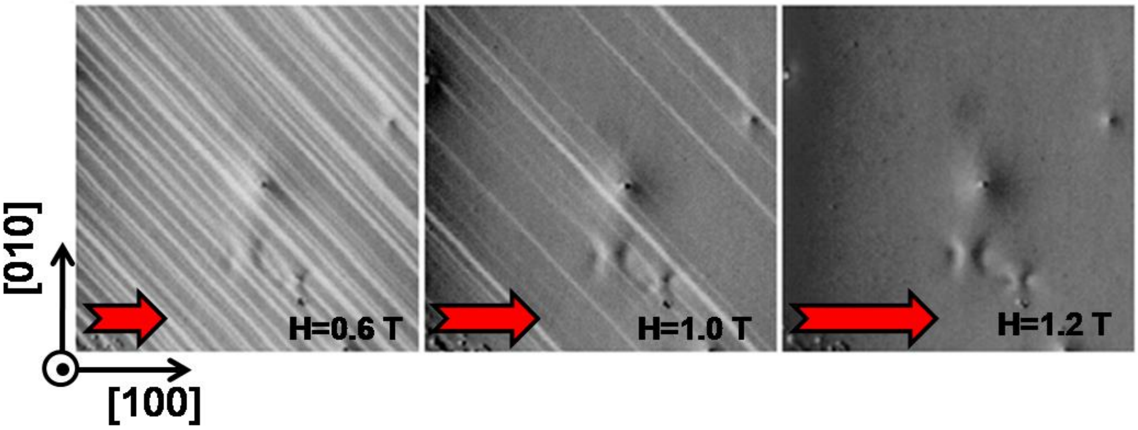

**Fig.1.2** The microstructure evolution due to magnetic field induced variant rearrangement [56].

The other mechanism to achieve giant magnetic field induced strain is the structural transitions under external magnetic field. The structural transitions contains the transition from paramagnetic parent phase to ferromagnetic martensite observed in Fe-Mn-Ga alloys[57] and the reverse transition from antiferromagnetic martensite to ferromagnetic parent phase observed in Ni-Mn-In(Sn) alloys [58, 59]. Since the required external magnetic field to induce structural transition is much larger than that to induce the reorientation of martensite variants, the NiMnGa Heusler alloys are more preferable to be applied in the practical actuators and sensors.

## 1.3 Bulk NiMnGa Heusler alloys

NiMnGa alloys are one of the typical Heusler alloys and exhibit magnetic field induced strain as large as 6%～12% in the order of kHz [19, 32], even under relatively low bias magnetic fields. However, the phase constituents, crystal structure of various phases, crystallographic features and mechanical properties of the Ni-Mn-Ga alloys are highly sensitive to the chemical composition and temperature. A deep and complete understanding of NiMnGa alloys is crucial to deal with the magnetic field induced reorientation of NiMnGa martensite variants. Their crystal structures, and crystallographic features and some specific properties are introduced here.

### 1.3.1 Phase constituents and their crystal structures of NiMnGa alloys

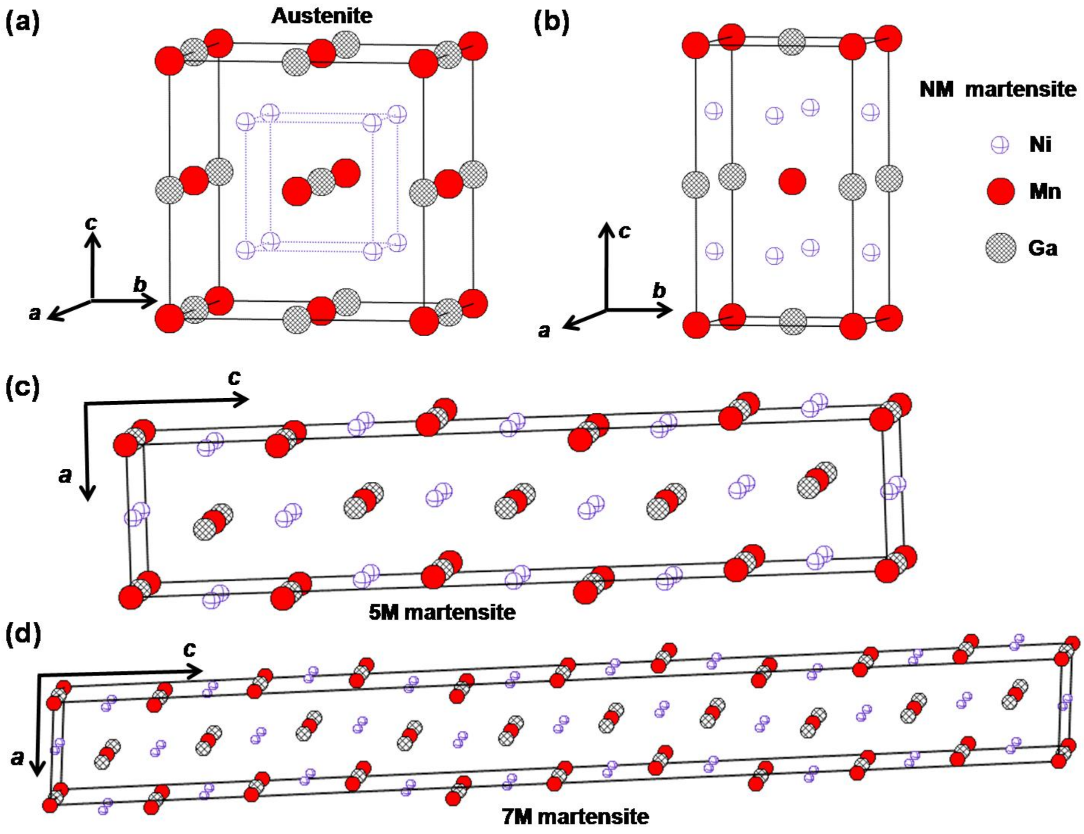

**Fig.1.3** The illustration of crystal structure of NiMnGa alloys in austensite(a), non modulated martensite (b) and modulated martensite (c,d)

NiMnGa alloys have an $L2_1$ structure in the austenite state, which is based on the bcc structure and consists of four interpenetrating face centered cubic (FCC) sublattices as shown for $Ni_2MnGa$ in Fig. 1.3(a). When the temperature is decreased, $Ni_2MnGa$ and off-stoichiometric Ni–Mn–Ga Heusler alloys undergoes martensitic transformations and transforms to the $L1_0$ tetragonal structure at low-enough Ga concentrations, as shown in Fig.1.3(b) [60-62]. Modulated structures other than the tetragonal structure can also be found in the martensite state especially at higher Ga concentrations. The most common crystal structure of modulated martensites are the 5M and 7M modulated structures (also denoted as 10M and 14M), as shown Fig.1.3(c) and Fig.1.3(d) [63-65].

From Fig.1.3(c) and Fig.1.3(d), the generated modulations can be seen for the 5M and 7M cases. The letter ‘M’ refers to the monoclinic resulting from the distortion associated with the modulation. Although this particular example is given for $Ni_2MnGa$, similar modulated states are observed in off-stoichiometric martensitic Heusler alloys incorporating other Z(Z=Ga, In, Sn) elements as well. The crystal structures of martensite given here are only typical examples, as for the individual alloys, the structure parameters of martensite depends on their particular composition.

### 1.3.2 Twin boundaries of martensites in NiMnGa alloys

For the shape memory performances, low twinning stress is the key property of the ferromagnetic shape memory alloys, since magnetically induced rearrangement is mediated by twin boundary motion. In the 5M and 7M modulated NiMnGa martensite, magnetically induced rearrangement can be realized by the motion of type I or type II twin boundaries. However, Type I twin boundaries exhibits a strong temperature-dependent twinning stress typically of about 1 MPa at room temperature. Type II twin boundaries exhibit a much lower and almost temperature independent twinning stress of 0.05–0.3 MPa [29, 66-68]. Therefore, the Type II twin boundaries are preferred to achieve giant magnetic field induced strain at lower external magnetic field.

### 1.3.3 Orientation relationship between martensite variants in NiMnGa alloys

Clarification of the orientation relationship between the martensitic variants is quite helpful to understand the rearrangement of martensitic variants and to find a training process or loading scheme which will eliminate or control the twin boundaries. To date, both the orientation relationships between martensite variants of non-modulated and modulated martensite were successfully determined, based on electron backscatter diffraction (EBSD) [69, 70] orientation determination, using the accurate crystal structure information.

For NM martensite, it is shown that there are two martensite variants with compound twin relationships existing in each martensite plate and in total eight martensite variants in each variant group. The twin related variants have a minimum misorientation angle of ~79 ° around the $<110>_{Tetr}$ axis [69, 70]. For modulated martensites (5M and 7M), four types of alternately distributed martensite variants (A, B, C, and D) in one martensite variant group were determined to be twin-related: A and C (or B and D) possess type I twin relation, A and B (or C and D) type II twin, and A and D (or B and C) compound twin. All the twin interfaces are in coincidence with the respective twinning plane ($K_1$) [26-28, 71-74].

### 1.3.4 Orientation relationship of martensitic transformation in NiMnGa alloys

The martensitic transformation is a diffusionless, displacive phase transformation under a specific orientation relationship between the parent phases and the product phase. Determination of the orientation relationship during martensitic transformation enables us to not only predict the microstructural configuration of martensite variants and their crystallographic correlation, but also control the microstructure of martensite via thermal treatment. Dependent on the chemical composition, there are three possible transformation sequences for NiMnGa alloys, which are A-5M-7M-NM, A-7M-NM and A-NM. Thus, the martensitic transformation may result in three different types of martensite (i.e. 5M, 7M, and NM martensites), which also depends on the chemical composition.

Up to now, Li *et.al* [73] revealed the favorable orientation relationship governing the austenite to incommensurate 7M martensite transformation is the Pitsch orientation relationship with $(101)_A \| (1\bar{2}\overline{10})_{mono}$ and $[10\bar{1}]_A \| [\overline{10}\,\overline{10}\,1]_{mono}$, as shown in table 1.1. The results of Cong *et.al* [70]indicates that the main orientation relationship between austenite and NM martensite is of the Kurdjumov–Sachs (K–S) relationship with $(111)_A \| (101)_{Tetr}$ and $[1\bar{1}0]_A \| [11\bar{1}]_{Tetr}$. Furthermore, the orientation relationship of intermartensitic transformation from 7M to NM martensite is of $(001)_{mono} \parallel (112)_{Tetr}$ and $[100]_{mono} \parallel [11\bar{1}]_{Tetr}$, as well as $(001)_{mono} \parallel (112)_{Tetr}$ and $[\bar{1}00]_{mono} \parallel [11\bar{1}]_{Tetr}$ determined by Li *et.al.* [71]

Table1.1 determined orientation relationship for martensitic and intermartensitic transformation in bulk NiMnGa alloys

| | Planes | Direction | Ref. |
|---|---|---|---|
| A→7M | $(101)_A \parallel (1\bar{2}\overline{10})_{mono}$ | $[10\bar{1}]_A \parallel [\overline{10}\,\overline{10}1]_{mono}$ | [73] |
| A→NM | $(111)_A \parallel (101)_{Tetr}$ | $[1\bar{1}0]_A \parallel [11\bar{1}]_{Tetr}$ | [70] |
| 7M→NM | $(001)_{mono} \parallel (112)_{Tetr}$ | $[100]_{mono} \parallel [11\bar{1}]_{Tetr}$ | [71] |
| | $(001)_{mono} \parallel (112)_{Tetr}$ | $[\bar{1}00]_{mono} \parallel [11\bar{1}]_{Tetr}$ | |

## 1.4 NiMnGa thin films

Shape memory material in thin films appears with the advancement of fabrication technology, where shape memory alloys are deposited directly onto micromachined materials or as stand-alone thin films. Micro-actuation models taking advantage of magnetic field induced reorientation have been proposed in NiMnGa thin films. Magnetically induced re-orientation in constrained NiMnGa film has been reported by Thomas *et al*. [55, 75]. With magnetic field operation, they are bound to have the advantage of fast response and high frequency operation. To date, since Ni-Mn-Ga thin films are promising candidates for magnetic sensors and actuators in MEMS, they have attracted considerable attention that focused on fabrication and freestanding, characterization of crystallographic features and microstructure, as well as martensitic transformation of NiMnGa thin films.

### 1.4.1 Fabrication process

The fabrication method needs to tune both microstructure and composition well, since microstructure and chemistry of NiMnGa films affects the phase constituent, the mobility of martensite variants and the critical stress. To date, a variety of techniques like sputtering, melt-spinning, pulsed laser deposition, molecular beam epitaxial and flash evaporation, have been used to deposit NiMnGa thin films [38-41, 76].

Via the sputtering, it is easy to tailor the composition which is a critical parameter for many desired properties related to actuation and shape memory effect. For instance, using co-sputtering, the composition of NiMnGa can be finely tuned by adding Ni or Mn to vary the overall composition. Because the NiMnGa thin film is found to have ~ 3-5% increase in Ni with respect to that in the targets and a corresponding decrease in Mn and Ga depending upon the deposition parameters, desired thin film composition can also be obtained by appropriate adjustment of target alloy composition.

As significant texturation through reducing the number of variant colonies or groups in the film could be realized by epitaxial growth. Preparation of Epitaxial NiMnGa thin films on single crystal substrates such as MgO , $Al_2O_3$ , GaAs [37, 40] by magnetron sputtering has been performed. To date, the procedure to fabricate continuous films with homogeneous chemical composition and controllable thicknesses has been parameterized [42, 44, 45, 55, 77, 78]. For instance, Heczko *et al*. [79] showed that thin films deposited on $SrTiO_3$ substrate showed epitaxial structure with a twinned orthorhombic martensite. Khelfaoui *et al*. [80] reported epitaxial thin film deposition on MgO (100) substrate using DC magnetron sputtering at substrate temperature of 350 ℃.

### 1.4.2 Phase constituent, microstructural and crystallographic features

In spite of the progress made in studying epitaxial NiMnGa alloys, the microstructural and crystallographic characterization of the produced films has been challenging due to the specific constrains from the substrate, the specific geometry of the film, and the ultra fineness of the microstructural constituents. Many pioneer efforts [34, 42-44, 55, 77, 81-88] have been made to characterize the phase constituent, microstructural and crystallographic features to advance the understanding of their physical and mechanical behaviors. The significant scientific and technical challenges remain.

#### 1.4.2.1 Crystal structure of phases in epitaxial NiMnGa thin films

X-ray diffraction (XRD) [42, 45, 55, 87] was first used to analyze phase constituents and texture components of epitaxial NiMnGa films. Multiphase (austenite, modulated martensite and non-modulated martensite) have been identified in most of the epitaxial NiMnGa films and strong textures of each phase have been revealed. For austenite and the non-modulated martensite that have relative simple crystal structure, the lattice constants have been unambiguously determined from the limited XRD reflection peaks [45, 55, 84, 88]. For the modulated martensite (7M or 14M), the maximum attainable number of observed reflection peaks in most cases has not been sufficient [42, 44, 45, 55, 89], thus the complete lattice constant determination is not possible. Without information on the monoclinic angle, the modulated martensite has to be simplified as pseudo-orthorhombic other than the monoclinic structure that has been identified in the bulk materials [42, 44, 45, 55, 89]. However, it is commonly accepted that 7M (or 14M) modulated NiMnGa martensite are of monoclinic crystal structure as in bulk NiMnGa materials [63-65].

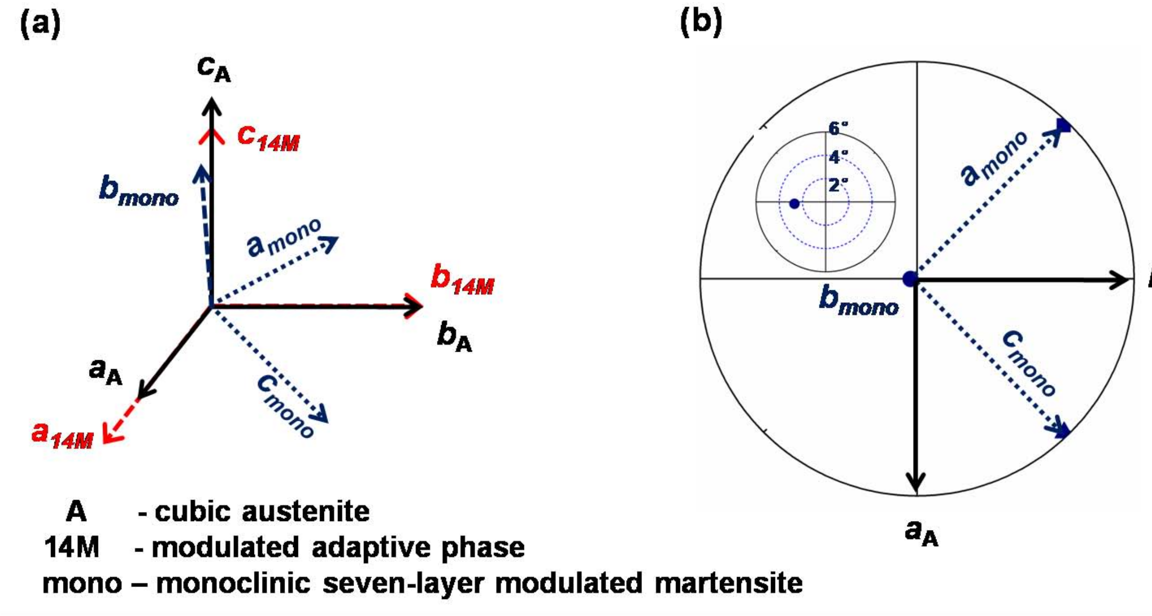

**Fig.1.4** (a) the relationship of crystal coordinate systems of austenite, adaptive phase and monoclinic seven layer modulated martensite. (b) The pole figure presents the projection of monoclinic seven layer modulated martensite coordinate system along $c_A$ ($[001]_A$) direction.

Generally, to describe the lattice parameters of 7M martensite, two different coordinate reference systems are frequently used in the literature, *i.e.* an orthogonal coordinate system attached to the original cubic austenite lattice and a non-orthogonal coordinate system attached to the conventional monoclinic Bravais lattice [27, 28, 63-65, 72, 73]. Since the monoclinic angle is very close to 90°, the modulated structure may be approximated as a pseudo-orthorhombic structure under the former scheme [55, 82, 89].

Fig.1.4(a) illustrates the settings of the cubic coordinate system for austenite, the pseudo-orthorhombic coordinate system [44, 89] for 14M modulated martensite under the adaptive phase model [89], and the monoclinic coordinate system for 7M modulated martensite [28, 72-74]. It is seen from Fig.1.4(b) that the deviations of the respective monoclinic basis vectors ($\boldsymbol{a}_{mono}$, $\boldsymbol{b}_{mono}$ and $\boldsymbol{c}_{mono}$) from the corresponding directions in the cubic coordinate system ($[\bar{1}10]_A$, $[001]_A$ and $[110]_A$) are very small (ranging from 1° to 3°), depending on the lattice constants of materials with different chemical compositions. The two settings have their own disadvantages. Apparently, a direct atomic or lattice correspondence between the austenite structure and the martensite structure is not so conveniently accessible under the monoclinic coordinate system.

**Table.1.2** the comparison of twinning elements of NiMnGa alloys in 14M-adaptive and 7M monoclinic crystal reference system

| | Austenite | 14M-adaptive | 7M modulated super cell | 7M-average unit cell |
|---|---|---|---|---|
| Crystal structure | Cubic | Pseudo orthorhombic | monoclinic incommensurate | monoclinic |
| Lattice parameter | $a$=0.578 nm | $a_{14M}$=0.618 nm<br>$b_{14M}$=0.578 nm<br>$c_{14M}$=0.562 nm | $a_{mono}$=0.4262 nm<br>$b_{mono}$=0.5442 nm<br>$c_{mono}$=4.1997 nm<br>β=93.7° | $a_{mono}$=0.4262 nm<br>$b_{mono}$=0.5442 nm<br>$c_{mono}$=0.41997 nm<br>β=93.7° |
| Type I twin | $\{101\}_A$ | $\{101\}_{4M}$<br>$a_{14M}$ -$c_{14M}$ *twin* | $\{1\ \bar{2}\ \overline{10}\}_{mono}$ | $\{1\ \bar{2}\ \bar{1}\}_{mono}$ |
| Type II twin | Close to $\{101\}_A$ | Close to $\{101\}_{14M}$<br>$a_{14M}$ -$c_{14M}$ *twin* | $\{1.124\ \bar{2}\ \overline{8.762}\}_{mono}$ | $\{1.124\ \bar{2}\ \overline{0.8762}\}_{mono}$ |
| Compound twin | $\{010\}_A$ | Un-determined in thin film | $\{1\ 0\ \overline{10}\}_{mono}$ | $\{1\ 0\ \bar{1}\}_{mono}$ |
| Invariant plane | $\{101\}_A$ | $(101\}_{14M}$ | $\{1\ \bar{2}\ \overline{10}\}_{mono}$ | $\{1\ \bar{2}\ \bar{1}\}_{mono}$ |

However, in the pseudo-orthorhombic setting, the basis vectors shown in Fig. 1.4(a) are not true lattice vectors, because the basis vectors of the original cubic cell become irrational in the newly formed structure after the martensitic transformation. This makes the precise description of the twin relationships of martensitic variants using well-defined twinning elements (such as twinning plane, twinning direction, and *etc.*) particularly difficult, especially when there are irrational twinning elements, as presented in table 1.2, the description of twinning elements in both 14M-adaptive and 7M monoclinic crystal reference system. It can be clearly seen that the precise twinning elements of Type II twin and compound twin have not been determined in the 14M-adaptive crystal system. Moreover, the pseudo-orthorhombic cell does not possess the same symmetry group as that of the monoclinic Bravais lattice. This affects the determination of the number of martensitic variants and the orientation relationships between adjacent variants.

#### 1.4.2.2 Microstructure and crystallographic features of epitaxial NiMnGa thin films

For epitaxial NiMnGa thin films, so far microstructure examinations have been made mainly using scanning electron microscopy (SEM), atomic force microscopy (AFM) and high resolution scanning tunneling microscopy (STM). The crystallographic aspects have been deduced by examining the surface corrugations of the films.

Microstructure analyses by scanning electron microscopy (SEM) revealed that martensite is in plate shaped and organized in groups as is the case in bulk material but much finer. The important feature found is that there are two kinds of martensite groups in terms of secondary electron (SE) image contrast. One is with relative homogeneous contrast that consists of long strips running parallel to the two edge directions ($[100]_{\mathrm{MgO}}$ and $[010]_{\mathrm{MgO}}$) of the substrate. The other is with relatively high contrast that contains plates with their length direction running roughly in 45 ° with respect to the substrate edges [44]. Close observations using atomic force microscopy [43, 44, 82] revealed that the different SE contrasts correspond to different surface corrugations of the films: the low SE relative contrast zones to low surface corrugation, whereas the high SE contrast zones to high surface relief.

According to the height profile of the surface relief in the high surface corrugation zones that are considered to be of 7M martensite, twin relationship between the adjacent martensite plates has been deduced – the so-called ***a*-*c*** twin relationship [44, 55]. It means that the pseudo-orthorhombic unit cells from the neighboring plates share a common ***b*** axis. The plate boundaries correspond to the $(101)_{orth}$ and they are inclined roughly 45 °to the substrate surface.

Later high resolution scanning tunneling microscopy (STM) examination indicated that within the 7M martensite plates, there are still fine periodic corrugations [43]. The fine corrugations have been considered to be related to the structure modulation of the 7M martensite [43] and preferentially, the 7M modulated martensite was considered to be composed of nano-twinned NM martensite (the so-called adaptive phase), as the lattice constants of the three phases fulfill the relation proposed by the adaptive phase theory ($a_{14M}=c_{NM}+a_{NM}-a_A$, $a_A=b_{14M}$, $c_{14M}=a_{NM}$ [89]). For the low contrast zones (composed of strips running parallel to the edges of the substrate ($[100]_{MgO}$ and the $[010]_{MgO}$)), the nature of the martensite has not been clearly revealed. Some consider that they are of NM tetragonal martensite [44] but others thought that they are of 7M martensite [42, 82]. The neighboring plates were deduced to also be ***a-c*** twin related with the plate interfaces ($(101)_{orth}$) perpendicular to the substrate surface, according to the epitaxial relationship between the substrate MgO and the austenite and the Bain relationship between the austenite and the NM martensite. For the substructure within the NM plate, as there are no significant corrugations detected, the microstructure and crystallographic features in the NM plates remains unclear.

Recently, further attempts have been made in further revealing the characteristic microstructures of NiMnGa films [90]. Two types of twins have been proposed, namely type I and type II twins, and build as paper models. Apparently, the type I twin is the so-called ***a-c*** twin with $(101)_A$ as twinning plane. However, it is not easy to correlate the proposed “type II twin” with yet published twin relationships in NiMnGa in literature, as there is no clear crystallographic description (such as twinning plane and twinning direction)) [90]. It has been found that the type I twins are mainly in low surface corrugation zones (the so-called Y pattern) and the type II twins mainly in high surface corrugation zones (the so-called X pattern) [91]. Cross section observations [91] of the film have evidenced that in the low surface corrugation zones there are two interface orientations, one being perpendicular to the substrate surface and the other parallel to the substrate surface. In the high corrugation zones, there is only one interface orientation that is tilted to the substrate surface by roughly 45 ° [91]. The apparent different occurrences of different twins in the two different variants zones are due to the constraints of the substrate [44, 91]. So far the short intra-plate interfaces in NiMnGa films have not been identified and the orientation relationship between the variants connected by such interfaces is not known.

Clearly, due to the lack of direct microstructure and crystallographic orientation correlation on the martensite variants (either 7M or NM martensite) and the inaccuracy of the orientation relationship between the parent austenite and the martensite, the precise information on the crystallographic configurations of the martensite lamellae inside each martensite plate and further the crystallographic organization of the martensite plates in each colony or group, especially the lamellar interfaces and plate interfaces, is still unavailable. In consequence, the possible number of variants in one variant group, their precise orientation relationships and interface planes stay unclear, which hinder the uncovering of microstructural singularities of NiMnGa films with respect to their counterparts in bulk materials.

## 1.5 Content of the present work

Based on the state of art mentioned above, epitaxial Ni-Mn-Ga thin films were produced by DC magnetron sputtering and then characterized by x-ray diffraction technique (XRD) and backscatter electron diffraction equipped in scanning electron microscope (SEM-EBSD). The scientific aim of the present work is first to produce qualified NiMnGa films with designed chemical compositions and film thicknesses and then to clarify the crystal structures of phase constituents, the configurations of martensite variants and their orientation correlations. The followings are the main content of the present work:

(1) Produce NiMnGa thin films with designed chemical composition and film thicknesses by magneto sputtering through optimizing the deposition parameters, such as sputtering power, substrate materials and seed layer materials..

(2) Determination of the phase constituents, their crystal structures and macroscopic crystallographic features of various types of martensite in NiMnGa thin films by X-ray diffraction technique.

(3) Correlation the microstructure with local crystallographic orientation of NM martensite and 7M modulated martensite by means of EBSD. Investigation of the orientation relationships between martensite variants and the orientation relationship

for martensitic transformation by determined local crystallographic orientations and crystallographic calculation.

(4) Examination of the influence of substrate constraint on martensitic transformation and preferential selection of martensite variants in NiMnGa thin films based on crystallographic analyses.

# Chapter 2 Experimental and crystallographic calculation

In this chapter, the techniques used to prepare and characterize Ni-Mn-Ga thin films are summarized. The essential crystallographic calculation methods are also described in details.

## 2.1 Sample preparation

### 2.1.1 Preparation of sputtering target

In order to obtain NiMnGa thin films with different phases at ambient temperature, NiMnGa alloys with various nominal composition were dedicatedly prepared by arc melting using high purity elements Ni (99.97 wt. %), Mn (99.9 wt. %) and Ga (99.99 wt. %). The ingots with designed nominal composition were melted by arc-melting in water cooled copper crucible under argon atmosphere. In order to obtain ingots with homogenous composition, each ingot was re-melted for four times and electromagnetic stirring was applied during the melting process. For further reducing the composition inhomogeneity of the as-cast ingots, the ingots were homogenized at 900 $^{o}$C for 12 h in a vacuum quartz tube, and then cooled within the furnace.

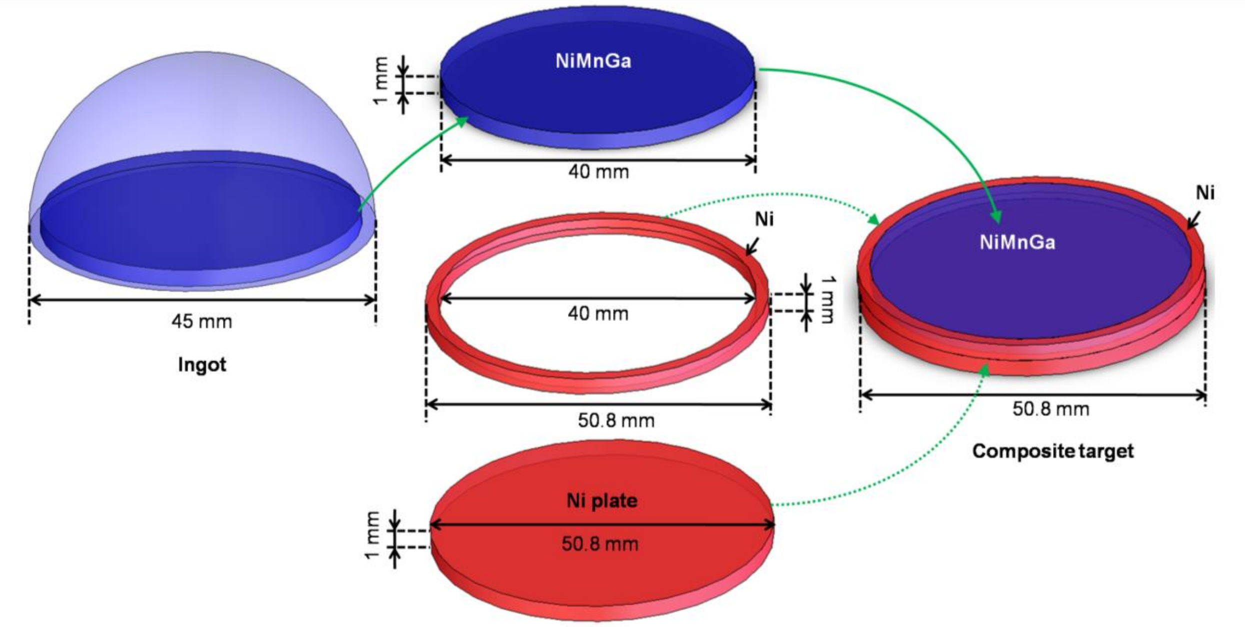

**Fig. 2.1** the schematics of fabrication process for NiMnGa target

Since the maximum diameter of each ingot melted in our arc-melting furnace is 45 mm, the dimension of the ingot is not large enough for preparing sputtering target (2-inch=50.8 mm). The NiMnGa plate with diameter of 40 mm and thickness of 1 mm was cut off out each ingot. The composite NiMnGa targets were prepared by assembling the NiMnGa plate, one pure Ni ring and one pure Ni plate, as shown in Fig.2.1.

As is well known, the manganese is a volatile element. Due to the volatilization during sputtering, the concentration of Manganese in NiMnGa thin films is less than that in the NiMnGa target. The phase consistent of NiMnGa alloys is very sensitive to the chemical composition. Thus, in order to obtain NiMnGa thin films with pertinent phases and microstructure at room temperature, several NiMnGa targets with various chemical compositions were selected to deposit thin films, as listed in Table 2.1.

**Table 2.1** List of NiMnGa targets with various compositions for deposition

| No. | Nominal composition of the targets | phase of targets at room temperature | Targeted composition in thin films | Targeted phase of thin film at room temperature |
|---|---|---|---|---|
| A | Ni46at.%-Mn32at.%-Ga-22at.% | A | Ni50at.%-Mn30at.%-Ga-20at.% | 7M |
| B | Ni48at.%-Mn30at.%-Ga-22at.% | A | Ni50at.%-Mn28at.%-Ga-22at.% | 5M |
| C | Ni50at.%-Mn28at.%-Ga-22at.% | 5M | Ni52at.%-Mn26at.%-Ga-22at.% | 7M |
| D | Ni50at.%-Mn30at.%-Ga-20at.% | 7M | Ni52at.%-Mn28at.%-Ga-20at.% | NM |

### 2.1.2 Thin film deposition

Several deposition methods have been developed to deposit thin films with the thickness ranging from several nanometers to several microns. Comparing with other depositing techniques, magnetron sputtering process has a number of advantages. First of all, plasma can be sustained at lower Argon pressures and hence resulting in low level of impurities. In addition, since the sputtering mechanism is not a thermal evaporation process, even the material with highest melting point can be deposited at ambient temperature. Usually, the deposited alloy films have a composition close to their target composition. Moreover, sputtering technique also produces films with a better adhesion than films produced by evaporation techniques. Substrate heating can be done by attaching a heater to the sample holder for epitaxial depositions. Thermal energy imparted to the deposition atoms increases the mobility of atoms forming thin film that have a nearly perfect atomic stacking during deposition.

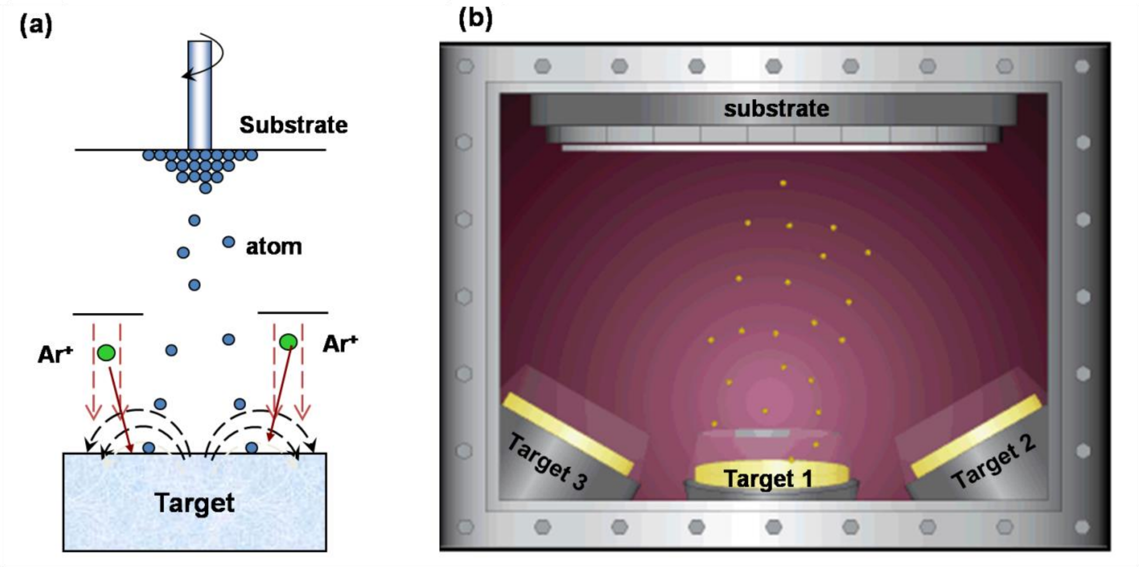

**Fig.2.2** illustration of direct current magnetron sputtering process (a) and the confocal magnetron sputtering system (b).

Magnetron sputtering is a physical vapor deposition technique by which ions accelerated under certain high voltage bombard the target surface to eject atoms towards the substrate to be deposited, as illustrated in Fig.2.2 (a). In a typical deposition, substrate with clean surface is attached to the substrate holder. Sputtering is done under high vacuum conditions to avoid contamination of the film. Base pressure is pumped down to $10^{-6}$ – $10^{-9}$ Torr using turbo and molecular pumps. On realizing a very high negative potential to the cathode target, plasma is generated. The Argon atoms in the plasma are ionized and accelerated towards the target at very high velocities. Due to the collision cascade, sputtered atoms with enough velocity get deposited on the substrate surface. The residual kinetic energy in target atoms is converted to thermal energy which increases their mobility and facilitates surface diffusion. Hence a continuous chain of atoms are formed resulting in a high quality film. Magnetic field produced by a permanent magnet referred is used to increase the path of the electron and hence the number of ionized inert atoms. It also can change the path of accelerated ions, which results in ring-like ejection zones on the surface of target.

In the present thesis, a custom-built multi-source magnetron sputtering system (JZCK-400DJ) was used for thin film deposition. As illustrated in Fig.2.2(b), the magnetron sputtering system has three sputtering sources arranged in confocal symmetry, which is capable of multilayer deposition, co-sputtering and deposition with a seed layer or cap layer. The base pressure before depositing is pumped below $9.0\times10^{-5}$ Pa. In order to obtain a continuous NiMnGa thin film, the working Ar pressure is fixed at 0.15 Pa during the whole deposition process. The deposition parameters, such as sputtering power, substrate materials, substrate temperature, time and seedlayer have been optimized through examining their effects on film thickness, film composition, and phase constituents and their microstructures.

## 2.2 Characterization

### 2.2.1 X-ray diffraction

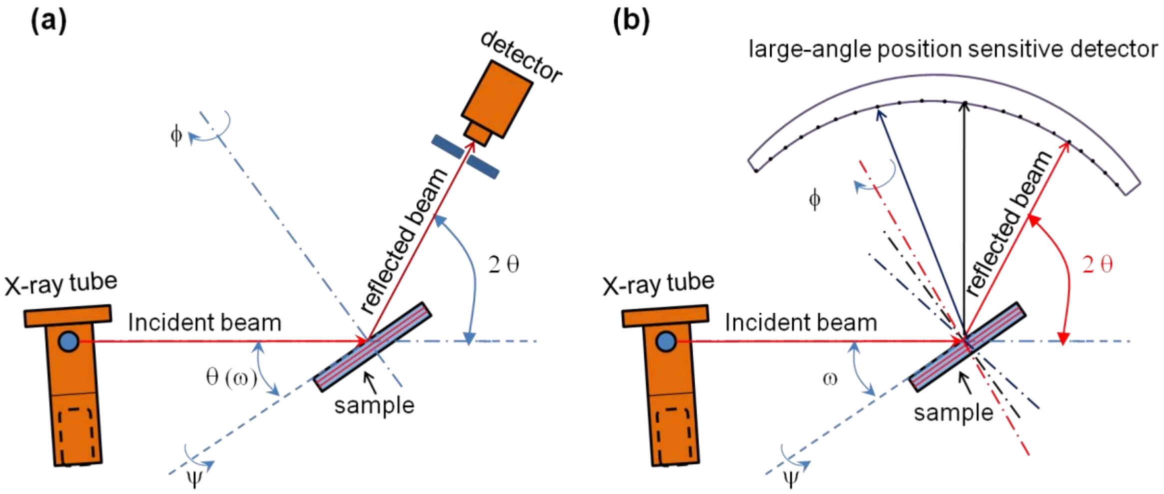

**Fig.2.3** schematic illustration of X-ray diffractometers. (a) the conventional four-circle x-ray diffractometer. (b) The x-ray diffractometer equipped with a curved position sensitive detector. Here, ω is the angle between incidence beam and sample surface. θ is the angle between incidence beam and diffraction plane. 2θ is the angle of incidence beam and reflected beam. ψ is the tilting angle with respect to the substrate surface. ϕ is the rotation angle along the film normal. ϕ=0, represents that the sample is not rotated.

X-ray diffraction is well developed technique for determining the crystal structure and macroscopic crystallographic features of crystalline materials. In the present study, three X-ray diffractometers were employed to determine both the crystal structure and macroscopic crystallographic orientations. All the diffractometers are of four circle X-ray diffractometer with Cobalt cathode source (Co $K_\alpha$ , $\lambda$ = 0.178897 nm).

For the determination of the crystal structure of the phases in NiMnGa thin films, two X-ray diffractometers were employed. One is of conventional diffractometer with point detector (Fig.2.3a) and the other is of X-ray diffractometer with curved position sensitive (CPS) detector (Fig.2.3b). Compared with the conventional diffractometers, X-ray diffractometer with curved position-sensitive offers fast data collection over a wide $2\theta$ range. As illustrated in Fig.2.3(b), the reflection-mode Debye-Scherrer geometry for CPS detectors is unique in the sense that the angle for the incident X-ray beam is kept fixed with respect to the normal of a flat diffracting sample, while the reflected beams are measured at multiple angles with respect to the sample normal. Considering that the thin film possesses in-plane texture, X-ray diffractometer with curved position-sensitive detector was used to obtain maximum numbers of diffraction peaks from the NiMnGa film.

### 2.2.2 SEM and SEM-EBSD

The microstructure, composition and microscopic crystallographic features of NiMnGa thin films were investigated by the field emission gun scanning electron microscope (FEG-SEM, JEOL-6500F). The composition of the NiMnGa films were investigated by the energy dispersive X-ray spectrometry system (EDS, Bruker) attached this SEM. The morphology and microstructure of the NiMnGa thin films were characterized by the secondary electron image and backscattered electron image. The microstructure and the microscopic crystallographic orientations of the NiMnGa martensite variants were analyzed using the same SEM equipped with an EBSD acquisition camera (Oxford HKL) and acquisition software (Oxford Channel 5). The EBSD patterns from the martensite variants were manually acquired using Channel 5 Flamenco’s interactive option.

The sample for SEM-EBSD analysis was electrolytically polished with the solution of 20%$HNO_3$ in volume in $CH_3OH$ at room temperature.

### 2.2.3 TEM

Philips CM 200 TEM with 200 kV accelerating voltage and $LaB_6$ filaments has been used to observe fine martensite variants in NiMnGa thin films. JEOL-2100F HR-TEM with field-emission gun was used to investigate the atomic-level stacking faults between variants within martensite plates.

Specimens for TEM investigation were cut off out the freestanding NiMnGa thin film and further thinned using twin-jet electrolytic polishing with an electrolyte of 20% $HNO_3$ in volume in $CH_3OH$ at ambient temperature.

## 2.3 Crystallographic calculations

With the precise crystallographic orientations of martensite variants, the orientation relationships between the martensite variants and their interfaces, and orientation relationship between austenite and martensite can be calculated. In addition, the following presents the calculation methods used in the present work.

### 2.3.1 Fundaments and definitions

#### 2.3.1.1 Reference systems

Considering the characteristics of the crystal structures of the phases concerned in the present study, austenite, modulated martensite and non modulated martensite, as given in Table 2.2 and shown in Fig. 2.4, in connect with SEM/EBSD orientation definition (Convention Oxford-Channel 5), two crystal coordinate systems are selected by convenience. One is referred to the Bravais lattice cell of each phase and the other is a Cartesian coordinate system set to the lattice cell in the present work. The macroscopic sample coordinate system is referenced to the three edges of MgO substrate ($[100]_{MgO}$, $[010]_{MgO}$, $[001]_{MgO}$).

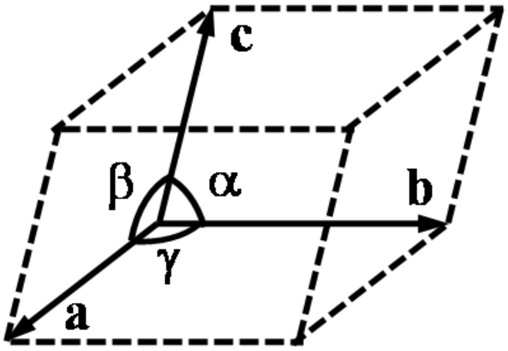

**Fig. 2.4** Schematic representation of a general (triclinic or anorthic) unit cell.

For the coordinate system referenced to the Bravais lattice cell, the basis is defined by three base vectors $\mathbf{a}$, $\mathbf{b}$ and $\mathbf{c}$ with respective lengths $a$, $b$ and $c$. The angles between each pair of base vectors are $\alpha$, $\beta$ and $\gamma$, as shown in Fig. 2.4. Its reciprocal space is defined by the three lattice vectors $\mathbf{a}^*$, $\mathbf{b}^*$ and $\mathbf{c}^*$ with respective lengths $a^*$, $b^*$ and $c^*$. The lattice vector in reciprocal space can be expressed by the lattice vector in the direct space, as shown in Eq.(2-1)

$$\mathbf{a}^* = \frac{\mathbf{b}\times\mathbf{c}}{\mathbf{a}\cdot(\mathbf{b}\times\mathbf{c})},\quad \mathbf{b}^* = \frac{\mathbf{c}\times\mathbf{a}}{\mathbf{b}\cdot(\mathbf{c}\times\mathbf{a})},\quad \mathbf{c}^* = \frac{\mathbf{a}\times\mathbf{b}}{\mathbf{c}\cdot(\mathbf{a}\times\mathbf{b})} \tag{2-1}$$

For the orthonormal crystal coordinate systems, the basis vectors are three orthogonal vectors **i**, **j** and **k** with **j** parallel to **b** (**j**//**b**) and **i** perpendicular to **b-O-c** plane ($\mathbf{i}\perp\mathbf{bOc}$) following Channel 5 convention, as shown in Fig.2.5 for the three phases in the present work.

**Table 2.2** The selection of coordinate systems

| | Phases | Crystal structure | Lattice parameters | |
|---|---|---|---|---|
| Crystal coordinate system | Austenite | Cubic (L2$_1$) | $\mathbf{a}_A=\mathbf{b}_A=\mathbf{c}_A$ | $\alpha=\beta=\gamma=90^{\mathrm{o}}$ |
| | 7M martensite | Monoclinic | $\mathbf{a}_{mono}\neq\mathbf{b}_{mono}\neq\mathbf{c}_{mono}$ | $\alpha=\gamma=90^{\mathrm{o}},\beta\neq 90^{\mathrm{o}}$ |
| | NM martensite | Tetragonal | $\mathbf{a}_{Tetr}=\mathbf{b}_{Tetr}\neq\mathbf{c}_{Tetr}$ | $\alpha=\gamma=\beta=90^{\mathrm{o}}$ |
| Sample coordinate system | MgO | Cubic | $\mathbf{a}=\mathbf{b}=\mathbf{c}$ | $\alpha=\beta=\gamma=90^{\mathrm{o}}$ |

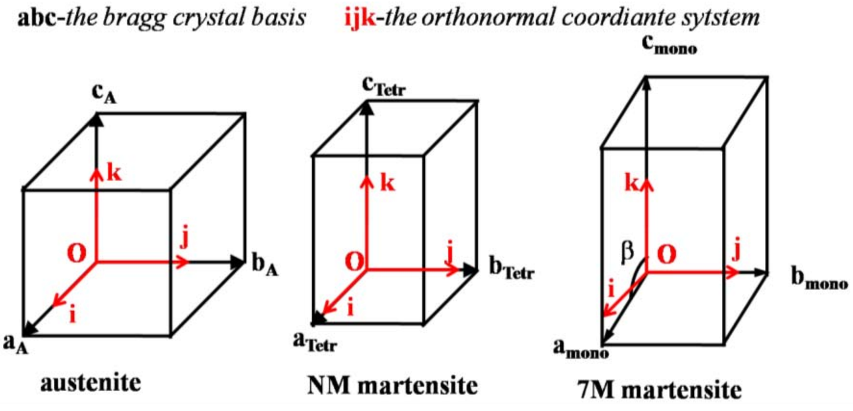

**Fig.2.5** The schematics of selection of orthonormal coordinate systems

For the macroscopic sample coordinate system, a Cartesian coordinate frame is set to the edges of MgO substrate with $x//[100]_{\mathrm{MgO}}$, $y//[010]_{\mathrm{MgO}}$ and $z//[001]_{\mathrm{MgO}}$, as shown in Fig. 2.6.

### 2.3.1.2 Metric tensors

The metric tensor contains the same information as the set of crystal lattice parameters, but in a form that allows direct computation of the dot product between two vectors. The computational and algebraic aspects of these mutually reciprocal bases can be conveniently expressed in terms of the metric tensors of these bases. The matrix of the metric tensor of the direct basis $\mathbf{G}$, or briefly the direct metric tensor, is

$$\mathbf{G}=\begin{bmatrix}\mathbf{a}\cdot\mathbf{a} & \mathbf{a}\cdot\mathbf{b} & \mathbf{a}\cdot\mathbf{c}\\ \mathbf{b}\cdot\mathbf{a} & \mathbf{b}\cdot\mathbf{b} & \mathbf{b}\cdot\mathbf{c}\\ \mathbf{c}\cdot\mathbf{a} & \mathbf{c}\cdot\mathbf{b} & \mathbf{c}\cdot\mathbf{c}\end{bmatrix}=\begin{bmatrix}a^2 & ab\cos\gamma & ac\cos\beta\\ ba\cos\gamma & b^2 & bc\cos\alpha\\ ca\cos\beta & cb\cos\alpha & c^2\end{bmatrix} \tag{2-2}$$

The corresponding reciprocal metric tensor is

$$\begin{aligned}\mathbf{G}^*&=\begin{bmatrix}\mathbf{a}^*\cdot\mathbf{a}^* & \mathbf{a}^*\cdot\mathbf{b}^* & \mathbf{a}^*\cdot\mathbf{c}^*\\ \mathbf{b}^*\cdot\mathbf{a}^* & \mathbf{b}^*\cdot\mathbf{b}^* & \mathbf{b}^*\cdot\mathbf{c}^*\\ \mathbf{c}^*\cdot\mathbf{a}^* & \mathbf{c}^*\cdot\mathbf{b}^* & \mathbf{c}^*\cdot\mathbf{c}^*\end{bmatrix}\\ &=\begin{bmatrix}\frac{b^2c^2\sin^2\alpha}{V^2} & \frac{abc^2(\cos\alpha\cos\beta-\cos\gamma)}{V^2} & \frac{ab^2c(\cos\alpha\cos\gamma-\cos\beta)}{V^2}\\ \frac{abc^2(\cos\alpha\cos\beta-\cos\gamma)}{V^2} & \frac{a^2c^2\sin^2\beta}{V^2} & \frac{a^2bc(\cos\beta\cos\gamma-\cos\alpha)}{V^2}\\ \frac{ab^2c(\cos\alpha\cos\gamma-\cos\beta)}{V^2} & \frac{a^2bc(\cos\beta\cos\gamma-\cos\alpha)}{V^2} & \frac{a^2b^2\sin^2\gamma}{V^2}\end{bmatrix}\end{aligned} \tag{2-4}$$

Where $V^2=a^2b^2c^2(1+2\cos\alpha\cos\beta\cos\gamma-\cos^2\alpha-\cos^2\beta-\cos^2\gamma)$.

With the matrix tensor, the vectors of direct space and reciprocal space can be easily transformed between each other according to Eq.(2-5). $[u \quad v \quad w]^T$ is a direction vector in direct space. $[h \quad k \quad l]^T$ is a miller index of a plane in direct space and also a direction vector in reciprocal space.

$$\begin{bmatrix}u\\ v\\ w\end{bmatrix}=\mathbf{G}^*\times\begin{bmatrix}h\\ k\\ l\end{bmatrix} \quad \text{and} \quad \begin{bmatrix}h\\ k\\ l\end{bmatrix}=\mathbf{G}\times\begin{bmatrix}u\\ v\\ w\end{bmatrix} \tag{2-5}$$

In the present study, for austenite, the matrix tensors in direct and reciprocal space are given in Eq.(2-6)

$$\mathbf{G_A} = \begin{bmatrix} a_A^2 & 0 & 0 \\ 0 & a_A^2 & 0 \\ 0 & 0 & a_A^2 \end{bmatrix} \quad \text{and} \quad \mathbf{G_A^*} = \begin{bmatrix} \frac{1}{a_A^2} & 0 & 0 \\ 0 & \frac{1}{a_A^2} & 0 \\ 0 & 0 & \frac{1}{a_A^2} \end{bmatrix} \tag{2-6}$$

For NM martensite, the matrix tensors in direct and reciprocal space are given in Eq.(2-7)

$$\mathbf{G}_{Tetr} = \begin{bmatrix} a_{Tetr}^2 & 0 & 0 \\ 0 & a_{Tetr}^2 & 0 \\ 0 & 0 & c_{Tetr}^2 \end{bmatrix} \quad \text{and} \quad \mathbf{G}_{Tetr}^* = \begin{bmatrix} \frac{1}{a_{Tetr}^2} & 0 & 0 \\ 0 & \frac{1}{a_{Tetr}^2} & 0 \\ 0 & 0 & \frac{1}{c_{Tetr}^2} \end{bmatrix} \tag{2-7}$$

For 7M martensite, the matrix tensors in direct and reciprocal space are given in Eq.(2-8) and Eq.(2-9)

$$\mathbf{G}_{mono} = \begin{bmatrix} a_{mono}^2 & 0 & a_{mono}c_{mono}\cos\beta \\ 0 & b_{mono}^2 & 0 \\ a_{mono}c_{mono}\cos\beta & 0 & c_{mono}^2 \end{bmatrix} \tag{2-8}$$

$$\mathbf{G}_{mono}^* = \begin{bmatrix} \frac{1}{a_{mono}^2\sin^2\beta} & 0 & -\frac{\cos\beta}{a_{mono}c_{mono}\sin^2\beta} \\ 0 & \frac{1}{b_{mono}^2} & 0 \\ -\frac{\cos\beta}{a_{mono}c_{mono}\sin^2\beta} & 0 & \frac{1}{c_{mono}^2\sin^2\beta} \end{bmatrix} \tag{2-9}$$

### 2.3.1.3 Coordinate transformation

As presented in Fig.2.6, the sample coordinate system and the Bravais lattice cell are related by two coordinate transformations. The first transformation is from the sample coordinate system to the orthonormal crystal coordinate system. Normally, this transformation can be expressed by the Euler angles $(\varphi_1, \Phi, \varphi_2)$ in Bunge notation [92, 93], which can be directly determined by EBSD system. According to Eq.(2-10), the transformation matrix can be constructed with the acquired Euler angles.

$$\mathbf{M_E} = \left\{ \begin{matrix} \cos\varphi_1\cos\varphi_2 - \sin\varphi_1\sin\varphi_2\cos\Phi & -\cos\varphi_1\sin\varphi_2 - \sin\varphi_1\cos\varphi_2\cos\Phi & \sin\varphi_1\sin\Phi \\ \sin\varphi_1\cos\varphi_2 + \cos\varphi_1\sin\varphi_2\cos\Phi & -\sin\varphi_1\sin\varphi_2 + \cos\varphi_1\cos\varphi_2\cos\Phi & -\cos\varphi_1\sin\Phi \\ \sin\varphi_2\sin\Phi & \cos\varphi_2\sin\Phi & \cos\Phi \end{matrix} \right\} \quad (2\text{-}10)$$

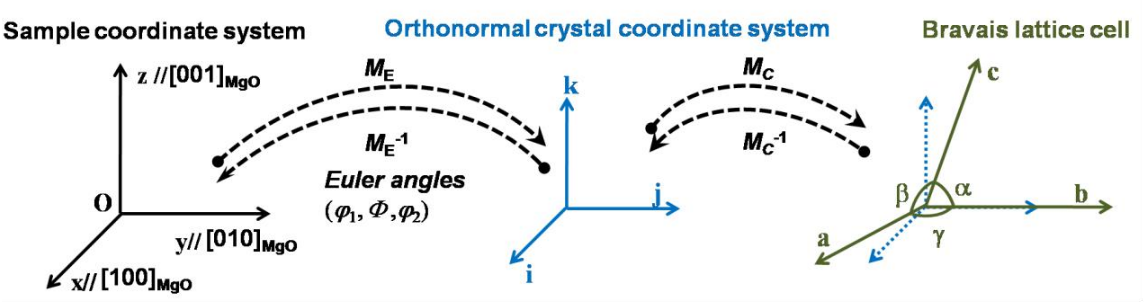

**Fig.2.6** Illustration of coordinate transformation from sample coordinate system to Bravais lattice cell.

The second transformation is from the orthonormal crystal coordinate system to the bravais lattice cell. In general, let the vector $[uvw]$ be in the old coordinate system $(\mathbf{abc})$ and $[UVW]$ be the same vector expressed in the new coordinate system $(\mathbf{ijk})$. Since, the coordinate transformation does not change the value of the vector, it follows that

$$u\mathbf{a} + v\mathbf{b} + w\mathbf{c} = U\mathbf{i} + V\mathbf{j} + W\mathbf{k} \quad (2\text{-}11)$$

The coordinate transformation can be made by:

$$\begin{bmatrix} U \\ V \\ W \end{bmatrix} = \mathbf{M_C} \begin{bmatrix} u \\ v \\ w \end{bmatrix} \quad (2\text{-}12)$$

If the transformation is from the orthonormal crystal coordinate system to a triclinic Bravais lattice unit cell,

$$\mathbf{M}_C = \begin{bmatrix} a\sqrt{\sin^2\gamma - [(\cos\beta - \cos\gamma\cos\alpha)/\sin\alpha]^2} & 0 & 0 \\ a\cos\gamma & b & c\cos\alpha \\ a(\cos\beta - \cos\gamma\cos\alpha)/\sin\alpha & 0 & c\sin\alpha \end{bmatrix} \quad (2\text{-}13)$$

In the present study, there are three phases: austenite, NM martensite and 7M martensite. The transformation matrixes from the orthonormal coordinate system to their Bravais crystal basis are given in Eq.(2-14) to Eq.(2-16) . For austenite $a = b = c = a_A$, $\alpha = \beta = \gamma = 90^o$, the coordinate transformation matrix crystal direction vector is

$$\mathbf{M}_{\mathbf{C}}^{\mathbf{A}} = \begin{bmatrix} a_A & 0 & 0 \\ 0 & a_A & 0 \\ 0 & 0 & a_A \end{bmatrix} \tag{2-14}$$

For non modulated martensite, $a = b = a_{Tetr}$ , $c = c_{Tetr}$ , $\alpha = \beta = \gamma = 90^{\circ}$ , the coordinate transformation matrix for crystal direction vector is

$$\mathbf{M}_{\mathbf{C}}^{\mathbf{Tetr}} = \begin{bmatrix} a_{Tetr} & 0 & 0 \\ 0 & a_{Tetr} & 0 \\ 0 & 0 & c_{Tetr} \end{bmatrix} \tag{2-15}$$

For 7M modulated martensite $a = a_{mono}$ , $b = b_{mono}$ , $c = c_{mono}$ , $\alpha = \gamma = 90^{\circ}$ , $\beta \neq 90^{\circ}$ , the coordinate transformation matrix crystal direction vector is

$$\mathbf{M}_{\mathbf{C}}^{\mathbf{mono}} = \begin{bmatrix} a_{mono}\sin\beta & 0 & 0 \\ 0 & b_{mono} & 0 \\ a_{mono}\cos\beta & 0 & c_{mono} \end{bmatrix} \tag{2-16}$$

### 2.3.2 Determination of orientation relationships

#### 2.3.2.1 Misorientation

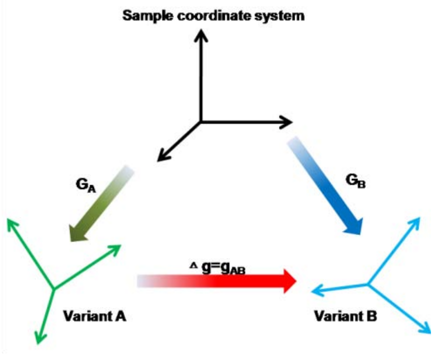

**Fig.2.7** The schematics of misorientation between two martensite variants

The misorientation between two crystals is defined by sets of rotations from one of the symmetrically equivalent coordinate systems of one crystal to another equivalent coordinate system of the other crystal. It can be calculated, using the experimentally determined orientations of the concerning crystals with respect to the macroscopic sample reference frame, as illustrated in Fig. 2.7. In the case of EBSD orientation under the convention of Oxford-Channel 5, the orientations of the crystals are characterized by a set of Euler angles

$(\varphi_1,\ \Phi,\ \phi_2)$ in Bunge's convention [92]. The rotations are between the orthonormal sample coordinate system the the orthonormal crystal coordinate system, as described in the coordinate transformation part (2.3.1.3). In the present study, this method was employed to calculate the misorientation between two martensite variants.

If the orientations of variant A and variant B are specified in rotation matrices $\mathbf{G_A}$ and $\mathbf{G_B}$ (Here, $\mathbf{G_A} = \mathbf{M_E^A}$, $\mathbf{M_E^A}$ is the Euler angle matrix). Then the misorientation matrix $\mathbf{\Delta g_{AB}}$ going from variant A to variant B can be defined as follows:

$$\mathbf{\Delta g_{AB}} = \mathbf{S_i^{-1} G_A{}^{-1} G_B S_j} \tag{2-17}$$

where the term $\mathbf{G_A}^{-1}$ is the reverse matrix of $\mathbf{G_A}$, transforming from crystal frame A back to the sample frame. $\mathbf{S_i}$ and $\mathbf{S_j}$ are the generic elements of the rotation symmetry group. This provides an alternate description of misorientation as the successive operation of transforming from the first variant frame (A) back to the sample frame and subsequently to the new variant frames (B). Various methods can be used to represent this transformation operation, such as: Euler angles, axis/angle (where the axis is specified as a crystallographic direction), or unit quaternion.

Misorientation expressed in angle and rotation axis is of particular interest for the present work, as it brings first information about twin orientation relationship between martensite variants. The determination of the angle and axis is explained as follow [94]. If we denote the misorientation matrix $\mathbf{\Delta g_{AB}}$ as Eq.(2-18)

$$\mathbf{\Delta g_{AB}} = \begin{bmatrix} g_{11} & g_{12} & g_{13} \\ g_{21} & g_{22} & g_{23} \\ g_{31} & g_{32} & g_{33} \end{bmatrix} \tag{2-18}$$

The misorientation angle $\omega$ and rotation $\mathbf{d}\,(\mathrm{d_1, d_2, d_3})$ can be calculated:

$$\omega = \arccos\left( \frac{g_{11} + g_{22} + g_{33} - 1}{2} \right) \tag{2-19}$$

(1) $\omega = 180^\circ$

$$\mathbf{d} = (d_1, d_2, d_3) = \left( \frac{g_{11}+1}{2}, \frac{g_{22}+1}{2}, \frac{g_{33}+1}{2} \right)$$

$$\text{with} \quad \left( \begin{array}{l} |d_m| = \max\left(|d_i|, i = 1,2,3\right) \\ d_m > 0, \text{by convention} \\ \forall i \neq m, \operatorname{sgn}(d_i) = \operatorname{sgn}(g_{im}) \end{array} \right) \tag{2-20}$$

(2) $\omega = 0^\circ$

$$\mathbf{d} = (d_1, d_2, d_3) = (1, 0, 0) \tag{2-21}$$

(3) $\omega \neq 180^\circ$ and $\omega \neq 0^\circ$

$$\mathbf{d} = (d_1, d_2, d_3) = \left( \frac{g_{23} - g_{32}}{2\sin\omega}, \frac{g_{31} - g_{13}}{2\sin\omega}, \frac{g_{12} - g_{21}}{2\sin\omega} \right) \tag{2-22}$$

**Table 2.3** the characteristic features of different twinning types

| | Type I twin | Type II twin | Compound twin |
|---|---|---|---|
| Number of 180° Rotation axis | 1 | 1 | 2 |
| Twinning plane **K**$_1$ | Rational | | Rational |
| Conjugate twinning plane K$_2$ | | Rational | Rational |
| Twinning shear direction $\eta_1$ | | Rational | Rational |
| Conjugate Twinning direction $\eta_2$ | Rational | | Rational |

The misorientation relationship, expressed in rotation axis/angle pairs, can be used to determine twinning type and certain twin elements. According to the definition of twin orientation relationship, there is at least one 180 °rotation for a twin. As shown in table 2.3, if there is one 180 °rotation and the Miller indices of the plane normal to the rotation axis are rational, the crystal twin belongs to type-I and ***K***$_1$ is identified. If there is one 180 °rotation and the Miller indices of the rotation axis are rational, the crystal twin belongs to type-II and $\eta_1$ is identified. If there are two independent 180 °rotations and the planes normal to the rotation axes are also rational, the twin is a compound twin, with one rotation axis being the twinning direction and the other being the normal to the twining plane [95]. With the determined twin type and rotation axis, the other twinning elements can be calculated using the general method developed by our group[95].

In addition, if the twin type and twinning elements are known, the rotation angle and rotation axis are also known. Thus, the misorientation matrix can be constructed by Eq. (2-25). Suppose the rotation angle is $\omega$, the rotation axis is $\mathbf{d} = (\mathrm{d}_1,\ \mathrm{d}_2,\ \mathrm{d}_3)^T$ expressed in the orthonormal crystal coordinate system and must be a unit vector.

$$\mathbf{M_R} = \begin{bmatrix} \cos\omega + d_1^2(1-\cos\omega) & d_1d_2(1-\cos\omega) - d_3\sin\omega & d_1d_3(1-\cos\omega) + d_2\sin\omega \\ d_1d_2(1-\cos\omega) + d_3\sin\omega & \cos\omega + d_2^2(1-\cos\omega) & d_2d_3(1-\cos\omega) - d_1\sin\omega \\ d_1d_3(1-\cos\omega) - d_2\sin\omega & d_2d_3(1-\cos\omega) + d_1\sin\omega & \cos\omega + d_3^2(1-\cos\omega) \end{bmatrix} \tag{2-23}$$

### 2.3.2.2 Stereographic projection and traces determination

The stereographic projection is a particular mapping that projects a sphere onto a plane, which is one of the projection methods to calculate pole figures. To calculate the pole figure of crystal directions or plane normal vectors, the vectors have to be expressed in the macroscopic coordinate system set with respect to the equatorial plane (for example the sample coordinate system) t before the stereographic projection. For instance, when a plane normal vector is $\mathbf{V_P} = (\mathbf{hkl})^*$. The corresponding vector in the sample coordinate system $\mathbf{V}_S$ can be calculated using Eq. (2-24).

$$\mathbf{V_S} = \mathbf{M_E M_C S_i G^* V_P} \tag{2-24}$$

Here, $\mathbf{M_E}$ is the Euler angle matrix, $\mathbf{M_C}$ is the coordinate transformation matrix from the orthonormal crystal coordinate system to the Bravais lattice basis. $\mathbf{S_i}$ is the symmetric element of a crystal, $\mathbf{G}^*$ is the metric tensor in reciprocal space. Then, the vector $\mathbf{V}_S = [t_1, t_2, t_3]^T$ should be normalized to unit vector.

As presented in Fig.2.8a, vector **OP** represents the vector $\mathbf{V}_S$ in the sphere $\mathbf{OP} = \mathbf{V}_S$. **P** is the intersection of vector **OP** with the sphere and is defined as the pole of plane ($hkl$). Let the line connect point **P** and the South Pole **S**. Line **PS** intersect the equatorial plane at point **P’**. **P’** is the stereographic projection of pole **P**. On the equatorial plane, **P** is expressed with the polar angle $\theta$ and the azimuth angle $\phi$ $(\theta, \phi)$, where

$$\theta = \arccos\left(\frac{\mathbf{ON} \cdot \mathbf{OP}}{|\mathbf{ON}| \cdot |\mathbf{OP}|}\right) \tag{2-25}$$

and

$$\phi = \frac{\pi}{2} - \arccos\left(\frac{\mathbf{OE} \cdot \mathbf{OP'}}{|\mathbf{OE}| \cdot |\mathbf{OP'}|}\right) \tag{2-26}$$

Line **HK** vertical to vector **OP’** in the equatorial plane represents the trace of plane $(hkl)$.

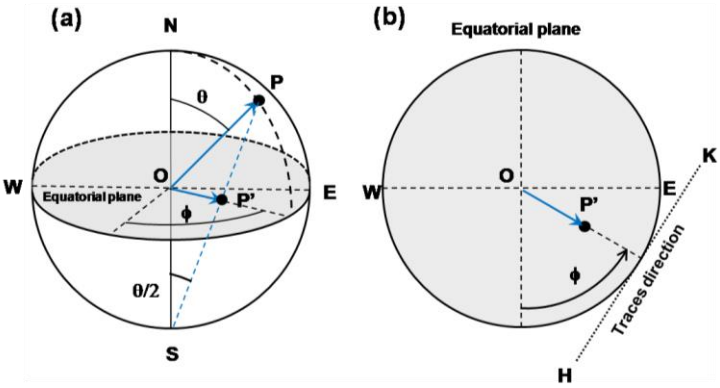

**Fig. 2.8** The stereographic projection of the normal on crystal

### 2.3.2.3 Orientation relationship between austenite and martensite

During martensitic transformation, one initial austenite grain transforms into several differently orientated martensitic variants under a specific orientation relationship. Normally, the orientation relationship possesses a pair of parallel plane and direction in austenite and in martensite. As presented in Fig.2.9, plane **P** $(hkl)_\mathrm{A}$ of austenite is parallel to plane **P’** $(hkl)_\mathrm{M}$ in martensite. The direction $[uvw]_\mathrm{A}$ in the plane **P** of austenite is parallel to the direction $[uvw]_\mathrm{M}$ in the plane **P** of martensite. To derive the transformation matrix from the austenite crystal reference frame to the that of the martensite under the defined orientation relationship, a orthonormal reference system set based on the parallel planes and directions would helpful for the determination.

As shown in Fig.2.9, the orthonormal reference frame is set such that the basis vector $\mathbf{e_2}$ is parallel to the crystal direction $[uvw]_\mathrm{A}$ and $[uvw]_\mathrm{M}$. The basis vector $\mathbf{e}_3$ is parallel to the normal direction of plane **P** and **P’** ($\mathbf{n}_{hkl}{}^{\mathrm{A}}$ and $\mathbf{n}_{hkl}{}^{\mathrm{M}}$). The axis $\mathbf{e}_1$ is parallel to the cross production of $[uvw]_{\mathrm{A}}$ and $\mathbf{n}_{hkl}{}^{\mathrm{A}}$. Under the given orientation relationship, the following relation holds:

$$\mathbf{M_E^A M_C^A S_i T_A} = \mathbf{M_E^m M_C^m S_j T_M} \tag{2-27}$$

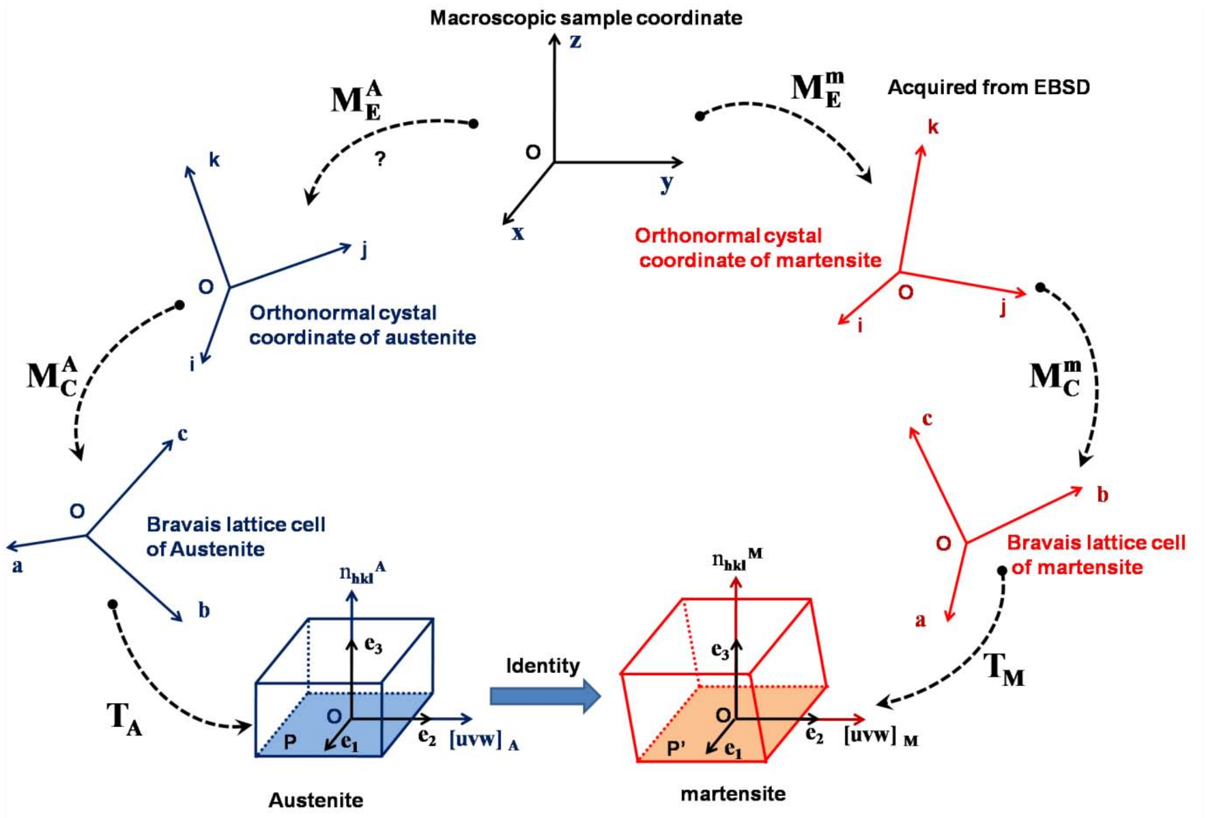

**Fig.2.9** Schematic illustration of the determination of OR between austenite and martensite.

Known the orientation of the martensite variants, the orientation of the austenite with respect to the sample coordinate system expressed in matrix can be calculated with Eq. (2-28)

$$\mathbf{M_E^A} = \mathbf{M_E^m M_C^m S_j T_M}(\mathbf{T_A})^{-1}(\mathbf{S_i})^{-1}(\mathbf{M_C^A})^{-1} = \mathbf{M_E^m M_C^m S_j T_{M\rightarrow A}}(\mathbf{S_i})^{-1}(\mathbf{M_C^A})^{-1} \tag{2-28}$$

Where, $\mathbf{M_E^m}$ is the Euler angle matrix of martensite, which can be determined by SEM-EBSD. $\mathbf{S_i}$ and $\mathbf{S_j}$ are the symmetry elements of austenite and martensite, respectively. $\mathbf{T_{M\rightarrow A}}$ is the transformation matrix from martensite to austenite. $\mathbf{T_A}$ and $\mathbf{T_M}$ are the transformation matrix from the Bravais lattice cell of austenite and martensite to the orthonormal reference frame set with respect to the parallel plane and direction.. $\mathbf{M}_{\mathbf{C}}^{\mathbf{A}}$ and $\mathbf{M}_{\mathbf{C}}^{m}$ are the transformation matrix for the orthonormal crystal coordinate system to the respective Bravais lattice cell of austenite and martensite.

**Table 2.4** the relationships of martensitic transformation

| Relationship | Plane | Direction | Ref. |
|---|---|---|---|
| Bain | $(001)_A \parallel (001)_M$ | $[001]_A \parallel [1\bar{1}0]_M$ | [96] |
| Kurdjumov-Sachs (**K-S**) | $(111)_A \parallel (101)_M$ | $[1\bar{1}0]_A \parallel [11\bar{1}]_M$ | [97] |
| Nishiyama-Wassermann(N-W) | $(111)_A \parallel (101)_M$ | $[\bar{2}11]_A \parallel [10\bar{1}]_M$ | [98, 99] |
| Pitsch | $(110)_A \parallel (1\bar{1}\bar{2})_M$ | $[1\bar{1}0]_A \parallel [\bar{1}1\bar{1}]_M$ | [100] |

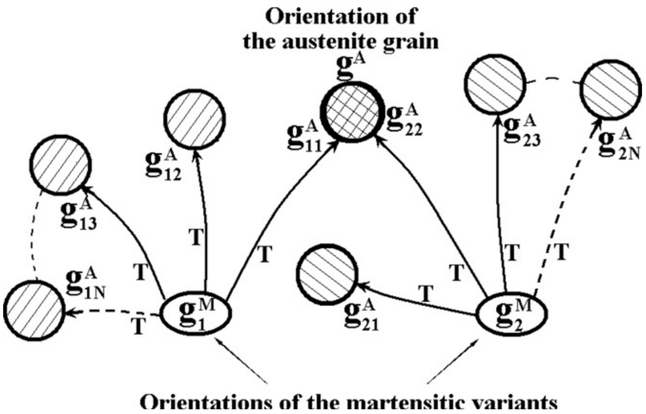

**Fig. 2.10** Schematic illustration of the determination of orientation relationship between austenite and martensite. $\mathbf{g}_{\mathbf{1n}}^{\mathbf{A}}$ and $\mathbf{g}_{2\mathbf{n}}^{\mathbf{A}}$ $(n = 1, 2, \cdots\cdots, N)$ represent possible distinct orientations of the austenite grain calculated from $\mathbf{g}_{\mathbf{1}}^{\mathbf{M}}$ and $\mathbf{g}_{2}^{\mathbf{M}}$ , respectively. The common orientation denoted as $\mathbf{g}^{\mathbf{M}}$ is the true orientation of the austenite grain and **T** is the orientation relationship existing between austenite and martensite.

For NiMnGa alloy, the possible orientation relationship between the austenite and martensite are shown in Table 2.4. If the orientation relationship between austenite and martensite is assumed to be the one between austenite and martensite, with Eq. (2-28), the orientation of the austenite from the measured orientations of the martensitic variants can be derived. The schematic illustration of the determination of the OR between austenite and martensite is shown in Fig.2.10. As presented in Fig. 2.10, if the distinct austenite orientations calculated from the observed variants have at least one orientation in common, it can be deduced that the assumed orientation relationship indeed exists. The common orientation is the orientation of the austenite.

### 2.3.3 Displacement gradient tensor

It is well known that martensitic transformation is a displacive transformation realized by coordinated atomic movements. As shown in Fig.2.11, the transformation can be regarded as the deformation of an artificially set reference cell based on the orientation relationship plane and direction of austenite to the corresponding reference cell of martensite by certain lattice distortion. The reference cells of austenite and martensite can be built according to the orientation relationship $((hkl)_{\mathrm{A}} \parallel (hkl)_{\mathrm{M}}, [uvw]_{\mathrm{A}} \parallel [uvw]_{\mathrm{M}})$. Normally, the reference cell of austenite is an orthogonal unit cell. To analysis the atomic displacement during martensitic transformation, the orthonormal coordinate systems are also helpful. As presented in Fig.2.11, orthonormal coordinate systems ($\mathbf{i}$ - $\mathbf{j}$ - $\mathbf{k}$) were fixed in both the austenite and martensite.

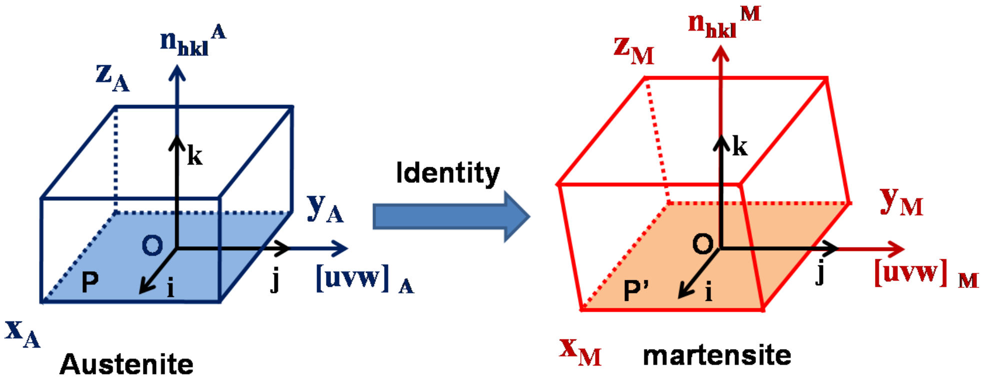

**Fig. 2.11** the schematics of martensitic transformation

The lattice vectors for both austenite and martensite can be expressed in the orthonormal coordinate system, as presented in Eq.(2-29) and Eq.(2-30)

$$\begin{cases} \mathbf{x}_{\mathrm{A}} = x_{\mathrm{A}} \cdot \mathbf{i} + 0 \cdot \mathbf{j} + 0 \cdot \mathbf{k} \\ \mathbf{y}_{\mathrm{A}} = 0 \cdot \mathbf{i} + y_{\mathrm{A}} \cdot \mathbf{j} + 0 \cdot \mathbf{k} \\ \mathbf{z}_{\mathrm{A}} = 0 \cdot \mathbf{i} + 0 \cdot \mathbf{j} + z_{\mathrm{A}} \cdot \mathbf{k} \end{cases} \tag{2-29}$$

$$\begin{cases} \mathbf{x}_{\mathrm{M}} = x_{\mathrm{M}x} \cdot \mathbf{i} + x_{\mathrm{M}y} \cdot \mathbf{j} + x_{\mathrm{M}z} \cdot \mathbf{k} \\ \mathbf{y}_{\mathrm{M}} = y_{\mathrm{M}x} \cdot \mathbf{i} + y_{\mathrm{M}y} \cdot \mathbf{j} + y_{\mathrm{M}z} \cdot \mathbf{k} \\ \mathbf{z}_{\mathrm{M}} = z_{\mathrm{M}x} \cdot \mathbf{i} + z_{\mathrm{M}y} \cdot \mathbf{j} + z_{\mathrm{M}z} \cdot \mathbf{k} \end{cases} \tag{2-30}$$

Then the displacement describing the lattice change from austenite to martensite can be obtained as $\mathbf{D}=\Delta\mathbf{x}+\Delta\mathbf{y}+\Delta\mathbf{z}$ , where

$$\begin{aligned}\Delta\mathbf{x}&=(x_{\mathrm{M}x}-x)\cdot\mathbf{i}+(x_{\mathrm{M}y}-0)\cdot\mathbf{j}+(x_{\mathrm{M}z}-0)\cdot\mathbf{k}\\ \Delta\mathbf{y}&=(y_{\mathrm{M}x}-0)\cdot\mathbf{i}+(y_{\mathrm{M}y}-y)\cdot\mathbf{j}+(y_{\mathrm{M}z}-0)\cdot\mathbf{k}\\ \Delta\mathbf{z}&=(z_{\mathrm{M}x}-0)\cdot\mathbf{i}+(z_{\mathrm{M}y}-0)\cdot\mathbf{j}+(z_{\mathrm{M}z}-z)\cdot\mathbf{k}\end{aligned}\tag{2-31}$$

Therefore, the displacement **D** can be rewritten as Eq. (2-32)

$$\begin{aligned}\mathbf{D}&=\Delta\mathbf{x}+\Delta\mathbf{y}+\Delta\mathbf{z}\\ &=((x_{\mathrm{M}x}-x_{\mathrm{A}})+(y_{\mathrm{M}x}-0)+(z_{\mathrm{M}x}-0))\cdot\mathbf{i}+((x_{\mathrm{M}y}-0)+(y_{\mathrm{M}y}-y_{\mathrm{A}})+(z_{\mathrm{M}y}-0))\cdot\mathbf{j}\\ &\quad+((x_{\mathrm{M}z}-0)+(y_{\mathrm{M}z}-0)+(z_{\mathrm{M}z}-z_{\mathrm{A}}))\cdot\mathbf{k}\\ &=\left(\frac{(x_{\mathrm{M}x}-x_{\mathrm{A}})}{x_{\mathrm{A}}}x_{\mathrm{A}}+\frac{(y_{\mathrm{M}x}-0)}{y_{\mathrm{A}}}y_{\mathrm{A}}+\frac{(z_{\mathrm{M}x}-0)}{z_{\mathrm{A}}}z_{\mathrm{A}})\right)\cdot\mathbf{i}\\ &\quad+\left((\frac{x_{\mathrm{M}y}-0)}{x_{\mathrm{A}}}x_{\mathrm{A}}+\frac{(y_{\mathrm{M}y}-y_{\mathrm{A}})}{y_{\mathrm{A}}}y_{\mathrm{A}}+\frac{(z_{\mathrm{M}y}-0)}{z_{\mathrm{A}}}z_{\mathrm{A}}\right)\cdot\mathbf{j}\\ &\quad+\left(\frac{(x_{\mathrm{M}z}-0)}{x_{\mathrm{A}}}x_{\mathrm{A}}+\frac{(y_{\mathrm{M}z}-0)}{y_{\mathrm{A}}}y_{\mathrm{A}}+\frac{(z_{\mathrm{M}z}-z_{\mathrm{A}})}{z_{\mathrm{A}}}z_{\mathrm{A}}\right)\cdot\mathbf{k}\\ &=D_i\cdot\mathbf{i}+D_j\cdot\mathbf{j}+D_k\cdot\mathbf{k}\end{aligned}\tag{2-32}$$

According to the definition, the displacement gradient tensor with respect to the orthonormal coordinate system is

$$\mathbf{M_D}=\begin{bmatrix}e_{11}&e_{12}&e_{13}\\e_{21}&e_{22}&e_{23}\\e_{31}&e_{32}&e_{33}\end{bmatrix}=\begin{bmatrix}\frac{\partial D_i}{\partial x}&\frac{\partial D_i}{\partial y}&\frac{\partial D_i}{\partial z}\\ \frac{\partial D_j}{\partial x}&\frac{\partial D_j}{\partial y}&\frac{\partial D_j}{\partial z}\\ \frac{\partial D_k}{\partial x}&\frac{\partial D_k}{\partial y}&\frac{\partial D_k}{\partial z}\end{bmatrix}=\begin{bmatrix}\frac{x_{\mathrm{M}x}-x_{\mathrm{A}}}{x_{\mathrm{A}}}&\frac{y_{\mathrm{M}x}}{y_{\mathrm{A}}}&\frac{z_{\mathrm{M}x}}{z_{\mathrm{A}}}\\ \frac{x_{\mathrm{M}y}}{x_{\mathrm{A}}}&\frac{y_{\mathrm{M}y}-y_{\mathrm{A}}}{y_{\mathrm{A}}}&\frac{z_{\mathrm{M}y}}{z_{\mathrm{A}}}\\ \frac{x_{\mathrm{M}z}}{x_{\mathrm{A}}}&\frac{y_{\mathrm{M}z}}{y_{\mathrm{A}}}&\frac{z_{\mathrm{M}z}-z_{\mathrm{A}}}{z_{\mathrm{A}}}\end{bmatrix}\tag{2-33}$$

By examining the change of the length of the basis vectors of the reference cell before and after the transformation, the displacement gradient tensor can be readily built.

To clearly analysis the constraint from MgO substrate during martensitic transformation process, the deformation gradient tensors of variants transformed from the $(1\bar{1}0)_{\mathrm{A}}$ and $(101)_{\mathrm{A}}$ planes were transformed to the basis coordinate system of MgO substrate, with the following equation.

$$\mathbf{M}_k = \left(\mathbf{M}_{\mathbf{MgO}\rightarrow\mathbf{A}}\mathbf{S}_{\mathrm{i}}\mathbf{M}_{\mathbf{A}\rightarrow\mathbf{pitsch}}\right)\mathbf{M}_{\mathrm{D}}\left(\mathbf{M}_{\mathbf{MgO}\rightarrow\mathbf{A}}\mathbf{S}_{\mathrm{i}}\mathbf{M}_{\mathbf{A}\rightarrow\mathbf{pitsch}}\right)^{-1} \tag{2-34}$$

$$\mathbf{M}_k = \begin{Bmatrix} e_{11} & e_{12} & e_{13} \\ e_{21} & e_{22} & e_{23} \\ e_{31} & e_{32} & e_{33} \end{Bmatrix}_{\mathrm{MgO}} \qquad \begin{pmatrix} e_{ij}:\ i=1,2,3;\ j=1,2,3; \\ k=1,2,3,4 \end{pmatrix} \tag{2-35}$$

The components of the displacement gradient tensor in the MgO substrate coordinate system represent the dilatation and shear. The components $e_{ij}\,(i=j)$ stand for the normal strain, which represent the dilatation along in the $[100]_{\mathrm{MgO}}$, $[010]_{\mathrm{MgO}}$ and $[001]_{\mathrm{MgO}}$ directions. The components $e_{ij}\,(i\neq j)$ are shear strains, which indicates the shear magnitude in *j* plane (the plane normal direction is the *j* axis) along *i* direction.

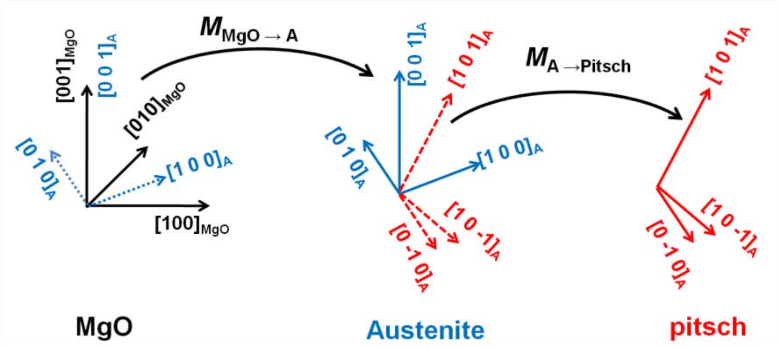

**Fig.2.12** Illustration of coordinate transformation from the coordinates of MgO substrate to austenite and from the coordinates of austenite to Pitsch.

As presented in Fig.2.12, the $\mathbf{M}_{\mathbf{MgO}\rightarrow\mathbf{A}}$ is the coordinate transformation matrix from MgO substrate to Austenite of NiMnGa. $\mathbf{S}_{\mathbf{i}}$ is the symmetric matrix of austenite. $\mathbf{M}_{\mathbf{A}\rightarrow\mathbf{pitsch}}$ is coordinate transformation matrix from the basic coordinate system to austenite coordinate system in the Pitsch relationship. The following presents the coordinate transformation matrix $\mathbf{M}_{\mathbf{MgO}\rightarrow\mathbf{A}}$ and $\mathbf{M}_{\mathbf{A}\rightarrow\mathbf{pitsch}}$:

$$\mathbf{M}_{\mathbf{MgO}\rightarrow\mathbf{A}} = \begin{Bmatrix} \cos(45°) & -\sin(45°) & 0 \\ \sin(45°) & \cos(45°) & 0 \\ 0 & 0 & 1 \end{Bmatrix},\ \mathbf{M}_{\mathbf{A}\rightarrow\mathbf{pitsch}} = \begin{Bmatrix} 0 & \sqrt{2}/2 & \sqrt{2}/2 \\ -1 & 0 & 0 \\ 0 & -\sqrt{2}/2 & \sqrt{2}/2 \end{Bmatrix}. \tag{2-36}$$

# Chapter 3 Fabrication of NiMnGa thin films

## 3.1 Introduction

In spite of the effort made recently to use sputtering technology for the preparation of thick Ni–Mn–Ga films (from sub-micron to micron range (<2 μm)), there are still some open questions in scientific and technical aspects in producing NiMnGa thin films, such as the control of the film composition during sputtering, the attainability of ultra thick epitaxial films (in several microns thick). The present work is dedicated to tackle these issues by optimizing the substrate parameters and the deposition parameters. Two substrate materials were used in the present work: one is thermal oxidization silicon and the other one is monocrystalline MgO (100). It is known that compared with MgO, Si substrate is not optimum for producing qualified epitaxial NiMnGa films in terms of mono-crystallinity of austenite at high temperature but it is of low cost. It allows to determinate the optimum depositing parameters that require large numbers of trial and errors with a relatively low cost. Thus in the present work, the Si substrate is used to optimize the primary deposition parameters and the MgO substrate is used to finally produced the qualified films with limited numbers of tests.

## 3.2 Experimental procedure

In the present study, the films are produced with the base pressure higher than $9.0 \times 10^{-5}$ Pa and the working pressure fixed at a low argon pressure (0.15 Pa) in the DC magnetron sputtering machine (JZCK 400DJ), in order to obtain continuous film.

For Si substrates, the substrate temperature, the target composition, the sputtering power and deposition time to produce NiMnGa films are given in Fig. 3.1. The selection of the deposition time is under the consideration to ensure the same film thickness at all the sputtering powers used. The targeted film thickness is about 1 micrometer. The film deposited under 75W is further undergone annealing at 750 ℃, 800 ℃ and 900 ℃.

Using the optimized sputtering power from the above tests, the other deposition parameters to produce the films are further refined on the MgO substrates without and with a seed layer (100 nm Cr or Ag). The corresponding parameters are displayed in Table 3.2.

**Table. 3.1** Parameters for producing NiMnGa thin films on Si substrates

| | Substrate temperature | Target composition | Power (W) | Time (h) |
|---|---|---|---|---|
| Si-1 | 500 | Ni50.0at. %-Mn28at.%-Ga22at.%. | 30 | 6 |
| Si-2 | | | 50 | 3.5 |
| Si-3 | | | 75 | 1.5 |
| Si-4 | | | 100 | 2 |

**Table. 3.2** Parameters for producing NiMnGa thin films on MgO substrate with and without seed layers

| | Seed layer | Substrate temperature | Target composition | Power (W) | Time (h) |
|---|---|---|---|---|---|
| MgO-1 | No | 400 | Ni46.0at. %-Mn32at.%-Ga22at.%. | 75 | 2 |
| MgO-2 | No | 500 | | | |
| MgO-3 | Ag | 500 | Ni46.0at. %-Mn32at.%-Ga22at.%. | | 2 |
| MgO-4 | Cr | | | | |
| MgO-5 | Cr | 500 | Ni46.0at. %-Mn32at.%-Ga22at.%. | | 4 |
| MgO-6 | Cr | | Ni48.0at. %-Mn30at.%-Ga22at.%. | | 2 |

The film thickness was verified by stylus profiler (DEKTAK 150). SEM (JEOL 6500F) equipped with EDS were used to analyze the microstructure and composition of these films. Home-made X-ray diffraction machine (FSM) with Cobalt cathode source ($\lambda$=0.178897 nm) was used to determine the phase constituents of the produced films.

## 3.3 Results

### 3.3.1 Influence of sputtering parameters and post annealing

#### 3.3.1.1 Influence of sputtering power

Table 3.1 presents the thickness and composition of NiMnGa thin films deposited at 500 ℃ on Si substrate. The nominal composition of the target is Ni50.0at. %-Mn28at.%-Ga22at.%. Compared to the composition of the target, it can be clearly seen that the concentration of Ga and Mn in NiMnGa thin films are decreased, while the concentration of Ni is increased at all shuttering powers. Fig. 3.1 shows the composition of

NiMnGa thin films deposited on Si substrate with various sputtering power. As presented in Fig.3.1, the concentration of Ni and Mn in NiMnGa thin films is slightly increased with the sputtering power, whereas the concentration of Ga is slightly decreased with the sputtering power. However, the changes are not linear with the sputtering power.

**Table 3.1** the corresponding parameters of NiMnGa thin films deposited on Si with various sputtering power

| | Power (W) | Time (h) | Thickness (μm) | Sputtering rates(nm/s) | Film composition (at.%) Ni | Mn | Ga |
|---|---|---|---|---|---|---|---|
| Si 1 | 30 | 6 | 1.142 | 0.059 | 54.85 | 23.92 | 21.23 |
| Si 2 | 50 | 3.5 | 1.142 | 0.091 | 55.36 | 24.22 | 20.42 |
| Si 3 | 75 | 1.5 | 0.714 | 0.132 | 55.76 | 23.92 | 20.02 |
| Si 4 | 100 | 2 | 1.285 | 0.159 | 55.17 | 24.97 | 19.87 |

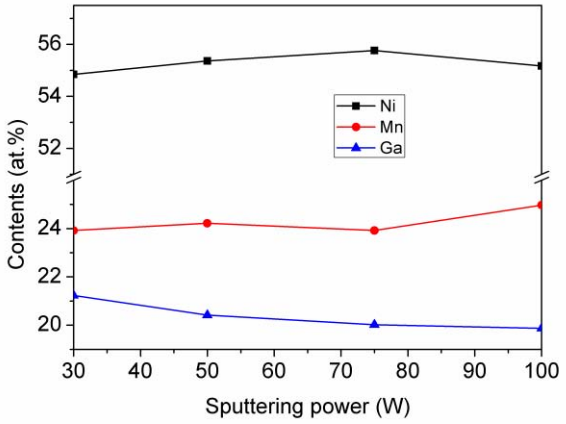

**Fig. 3.1** Composition of NiMnGa thin films deposited on Si substrate with various sputtering power

Fig.3.2 shows the microstructure of NiMnGa thin films deposited on Si substrate with various sputtering power. The inset of each figure is the cross-section view. All of these films show a column structure, suggesting the at austenite state the films are not monocrystalline. For the films deposited on 30 W and 50 W, the column size is about 1 μm, while for films deposited on 75 W and 100 W, the column size decrease to 500 nm. The surface roughness of NiMnGa thin films increases with the sputtering power. Normally, high sputtering power corresponds to high sputtering rate. It is easier to generate column structure with higher sputtering rate, as there is not enough time for the diffusion of these elements. Therefore, a lower sputtering rate is helpful to generate continuous films. However, low sputtering rate requires long depositing time for a given film thickness, as shown in Table 3.1. Considering that the film thickness should be up to 1 micron, a compromise should be made between the sputtering rate or power and the depositing time. Taking into account of the influence of the sputtering power on the film composition, the sputtering power of 75 W is selected. Hereafter, all the films deposited on MgO substrates are under this sputtering power.

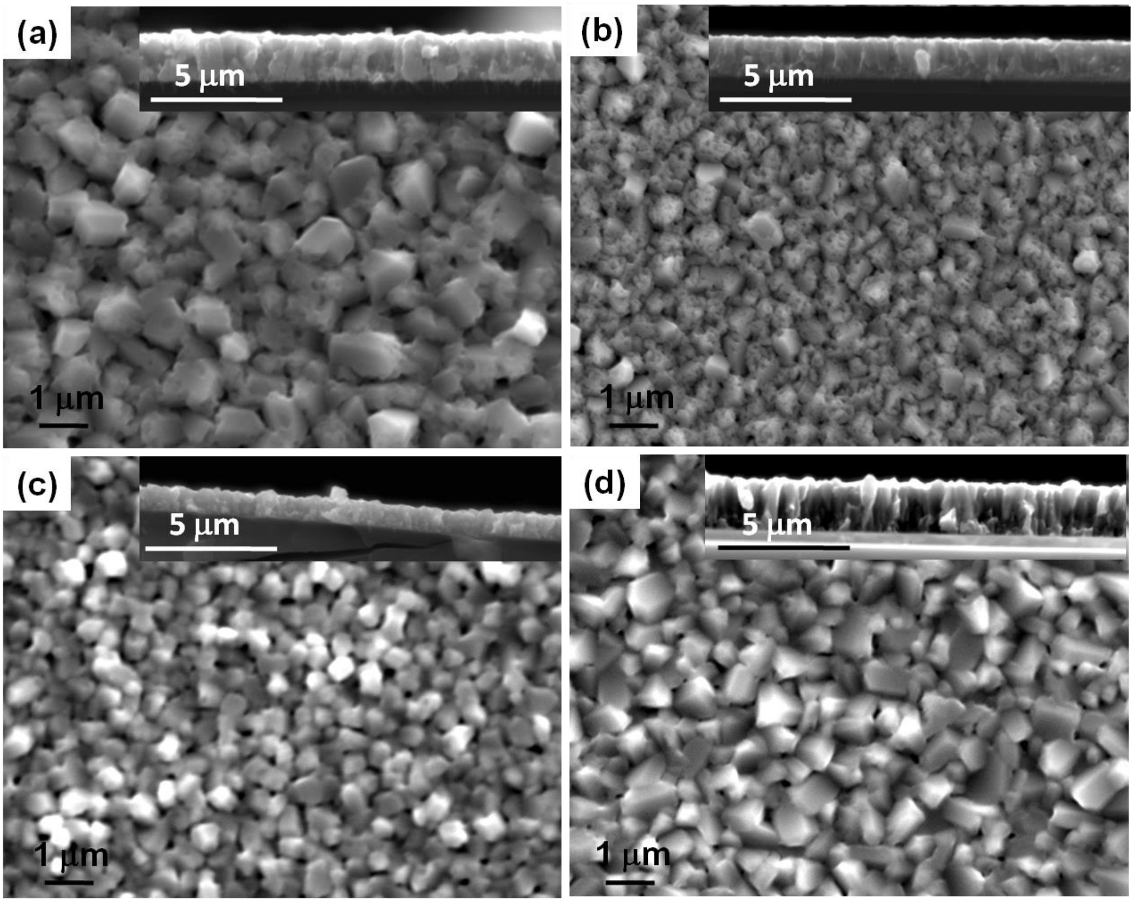

**Fig. 3.2** Microstructure of thin films deposited on Silicon substrate at various sputtering power (a) 30w, (b) 50w, (c) 75w, (d) 100w.

### 3.3.1.2 Influence of annealing

The film deposited under 75 W were further annealed at different temperature for 2 h. Fig. 3.3 shows the microstructures of the thin film annealed at different temperatures. It can be seen that the column thicknesses increase with the annealing temperatures. The film annealed at 900 ℃ for 2 h show a plate structure in each column with the plate width of about 200 nm. .

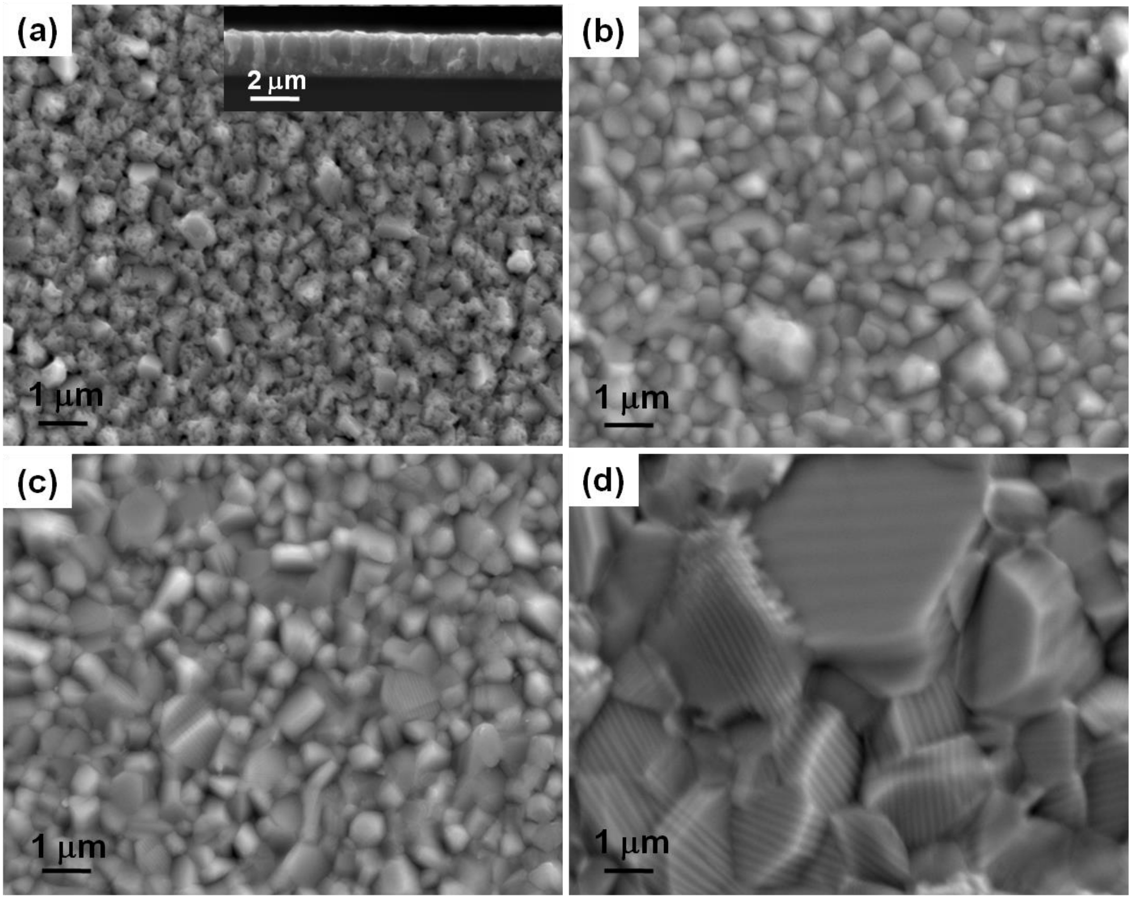

**Fig. 3.3** SEM microstructure of NiMnGa thin films deposited on Si annealed at different temperature for 2 h (a) As-deposited; (b) 750 ℃; (c) 800 ℃; (d) 900 ℃

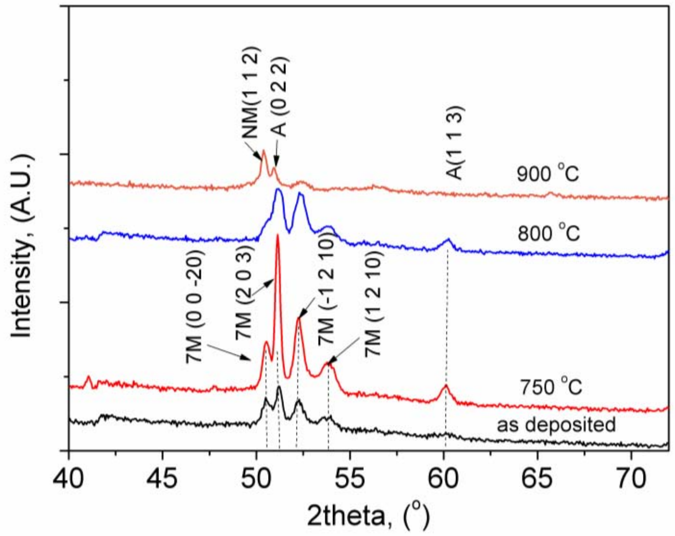

**Fig. 3.4** X-ray diffraction pattern of Si\NiMnGa thin films annealed at various temperatures for 2 h

Fig.3.4 shows the X-ray diffraction pattern of the thin film annealed at different temperatures. The as-deposited film contains seven layer modulation (7M) martensite and austenite. The intensity of the 7M martensite diffraction peaks increase with the annealing temperatures, when the annealing temperature is lower than 850 ℃, indicating that annealing promotes the transformation from austenite to martensite. However for the film annealed at 950 ℃, after the annealing, austenite transforms directly into NM martensite with no 7M modulated martensite retained.

### 3.3.2 Influence of substrate temperature and seed layer on the epitaxial thin films

#### 3.3.2.1 Influence of MgO substrate temperature

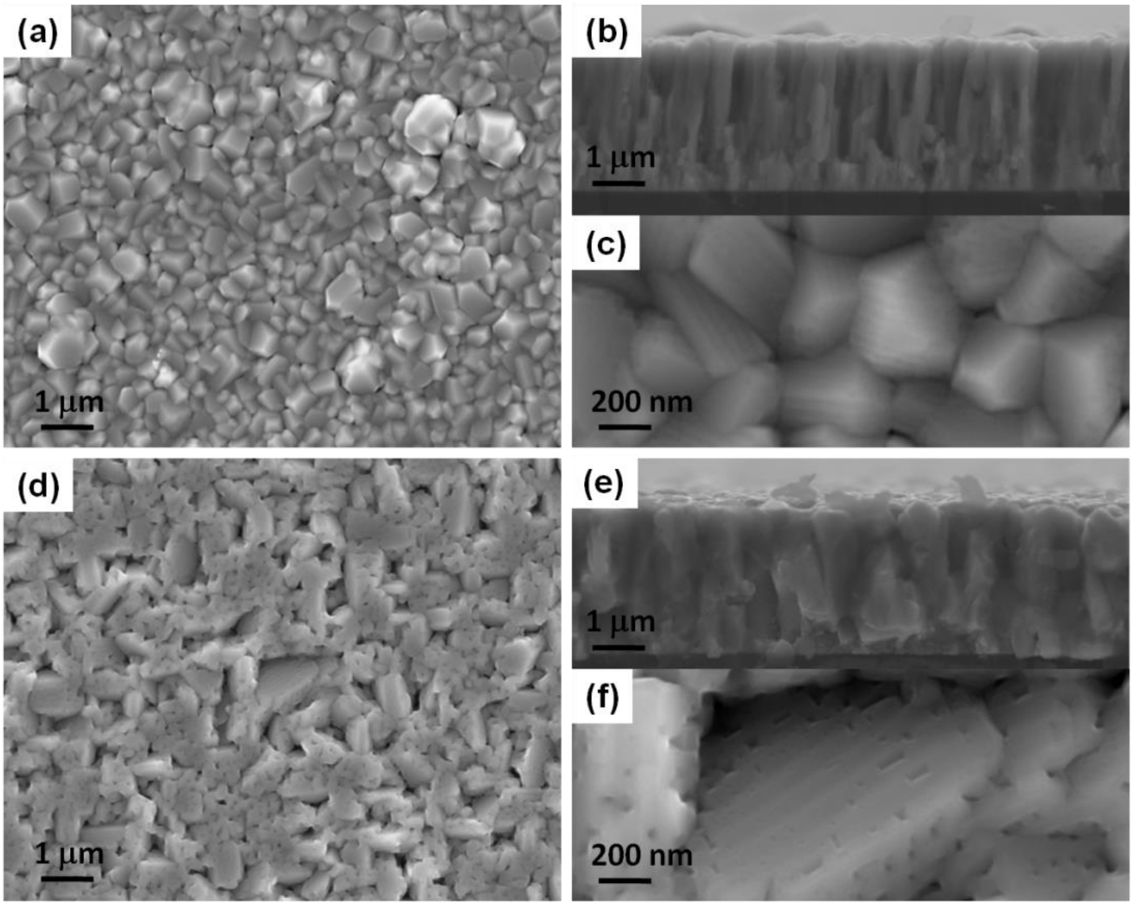

**Fig. 3.5** SEM-image of NiMnGa thin films deposited on MgO(100) at two substrate temperatures (a-c)400℃, (d-f) 500 ℃.

The above results show that the NiMnGa thin films deposited on silicon substrate is of column structure due to the polycrystallization of the high temperature austenite. Although the post annealing is helpful to increase the column thickness size and promotes martensitic transformation it cannot change the mono-crystallinity of austenite. Therefore, monocrystalline MgO(100) substrates were used to fabricate the epitaxial NiMnGa thin films. During the deposition, certain Mn and Ga are lost resulting in high Ni concentration, the target composition with reduced Ni concentrations were used, as shown in Table 3.3.

Fig.3.5 presents the SEM-image of NiMnGa thin films deposited on MgO(100) single crystalline substrate at 400 ℃ and 500 ℃, respectively without a seed layer. The microstructures of the two NiMnGa thin films are still of column structure. Fine lamellae could be observed in the high magnification SEM image in each column.

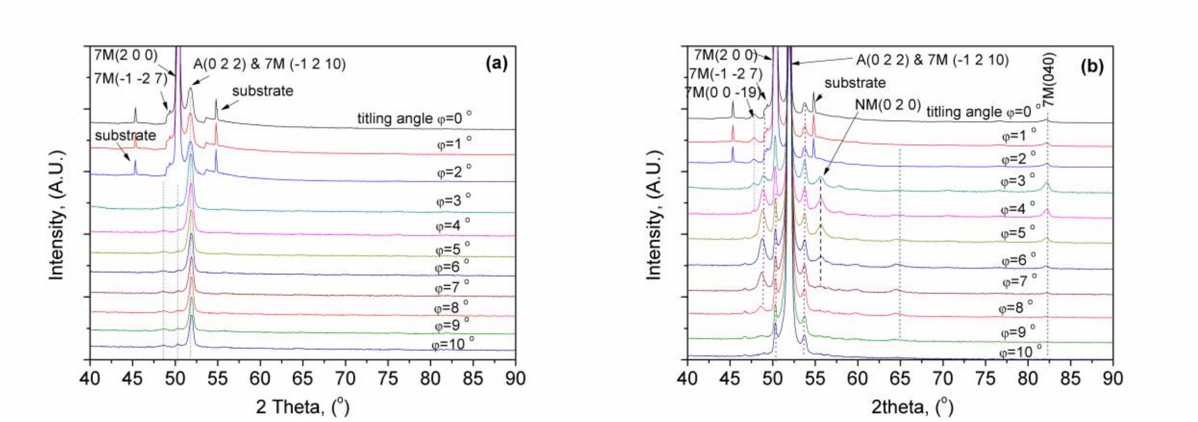

**Fig. 3.6** NiMnGa thin films deposited on MgO(100) at different substrate temperature(a)400℃, (b) 500 ℃.

Fig.3.6 shows the X-ray diffraction patterns of the NiMnGa thin film deposited on the MgO substrate. X-ray diffraction spectra show that the crystal structure of these thin films is of those of 7M martensite and austenite.

### 3.3.2.2 Influence of seed layer

To obtain continuous film, a 100 nm seed layer of either Ag or Cr is deposited on the substrate. Figure 3.7 shows the microstructures of the NiMnGa thin films deposited on MgO (100) and on MgO (100) with Ag or Cr seed layer. As can be seen in Fig. 3.7, only the NiMnGa thin films deposited on MgO\Cr show a continuous character. On one hand the Cr seed layer improves element diffusion on the substrate and on the other hand, the Cr seed layer decreases lattice misfit between the substrate and the NiMnGa thin films. Since the lattice parameter of Cr and NiMnGa austenite is 2.888 Å and 5.803 Å, respectively. The orientation relationship between MgO, Cr and NiMnGa is $\mathrm{MgO(001)[110]} \| \mathrm{Cr(100)[100]} \| \mathrm{NiMnGa(100)_A[001]_A}$. The misfit between the MgO and the austenite of NiMnGa is 2.42 %, whereas that between Cr and NiMnGa is 0.75%. It is easier to generate epitaxial thin films with small misfit.

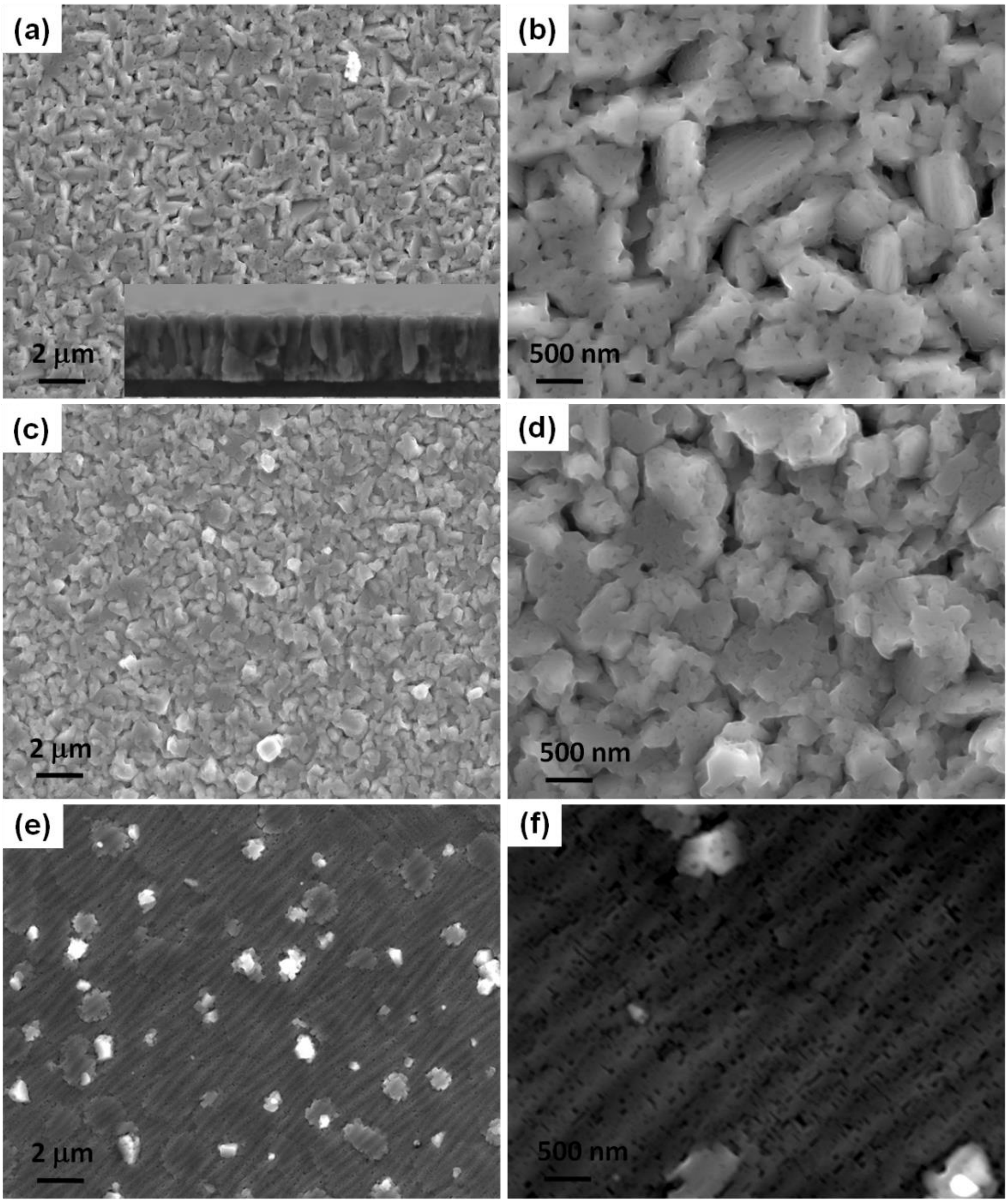

**Fig. 3.7** NiMnGa thin films deposited on MgO (100) with and without seed layer (a) MgO(100),(b) MgO\Ag(100 nm), (c) MgO\Cr(100 nm)

### 3.3.3 Influence of film composition and thickness

#### 3.3.3.1 Influence of film composition

The composition of NiMnGa alloys plays a key role on the crystal structure of the phase constituents and thus the magnetic induced strain. Fig.3.8 presents the microstructure of MgO\Cr\NiMnGa thin films with different composition (a-b) Ni51.42at.%-Mn29.25at.%-Ga19.33at.%, (c-d) Ni55.45at.%-Mn26.62at.%-Ga17.93at.%. It is seen that for the two compositions, the films contain lamellar structure, some pores (dark) and inclusion-like terraces (light). The difference is that with the increase of Ni concentration (Fig. 3.8 (c) and (d), the pores and terraces become dominant. Analyses show that the pores and terraces are of Ni-rich precipitates. Moreover, with the increase of Ni concentration, the sizes of the lamellae become smaller.

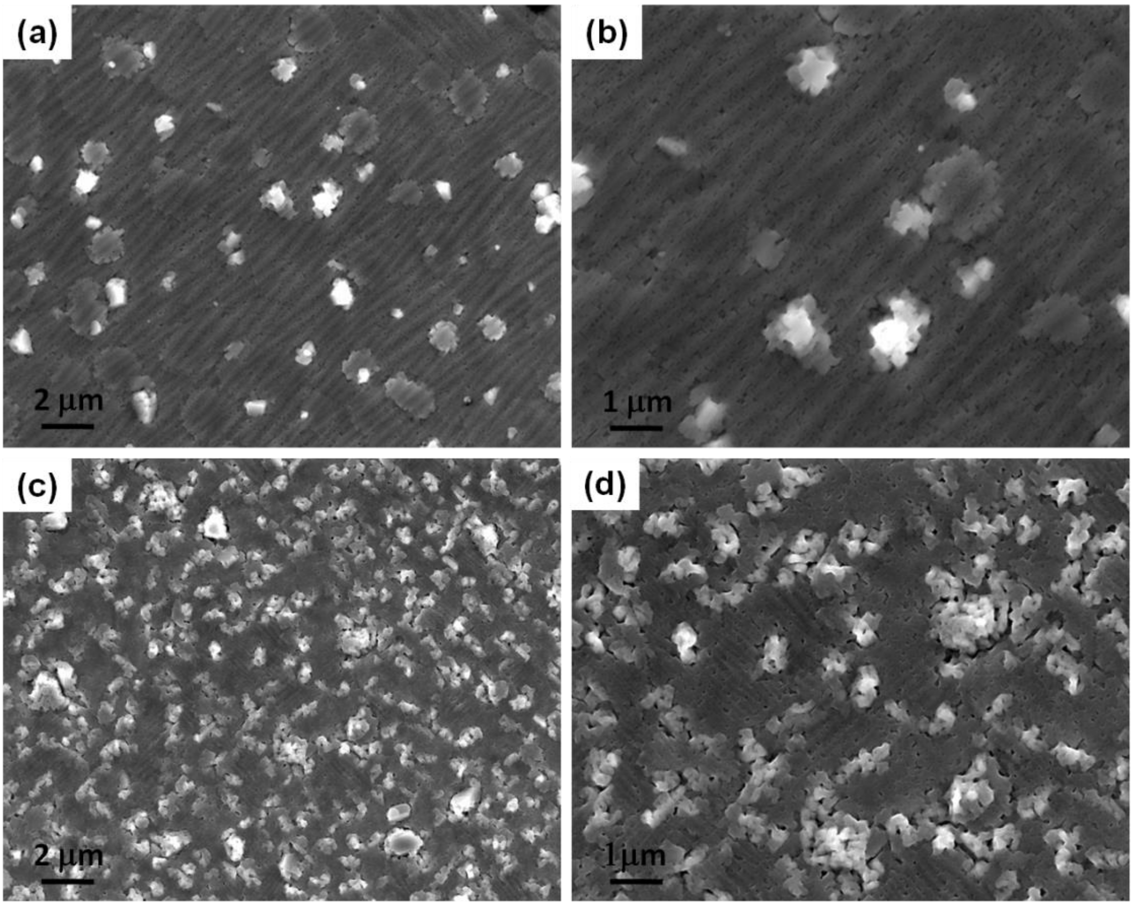

**Fig. 3.8** SEM image of MgO\Cr\NiMnGa thin films with different compositions
(a-b) Ni51.42at.%-Mn29.25 at.%-Ga19.33 at.%, (c-d) Ni55.45 at.%-Mn26.62 at.%-Ga17.93 at.%

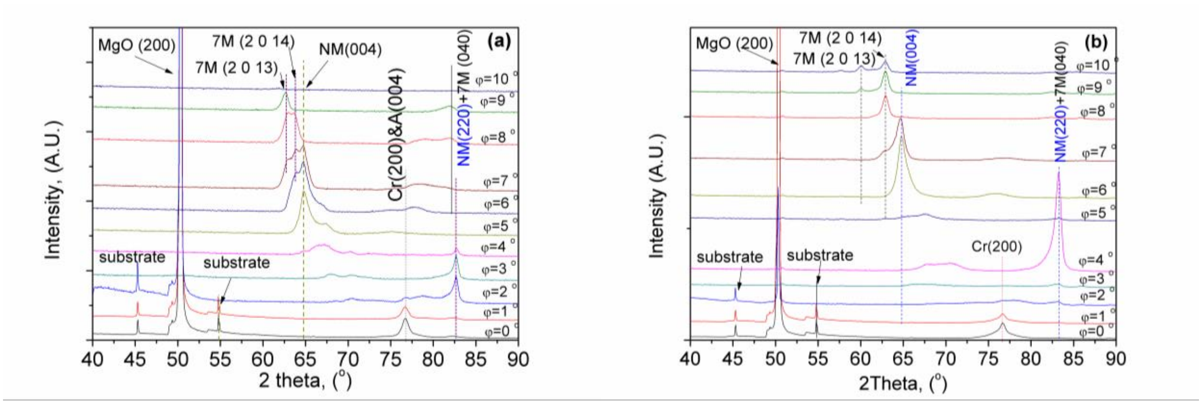

**Fig. 3.9** XRD patterns of MgO\Cr\NiMnGa thin films with different compositions
(a) Ni51.42 at.%-Mn29.25 at.%-Ga19.33 at.%, (b) Ni55.45 at.%-Mn26.62 at.%-Ga17.93 at.%

Fig.3.9 presents the X-ray diffraction patterns of the NiMnGa thin films. It can be clearly seen that the two films are composed of austenite, 7M and NM martensite. However, the intensity of NM $(220)_{Tetr}$ and $(004)_{Tetr}$ peaks of Ni55.45 at.%-Mn26.62 at.%-Ga17.93at.% thin film are much higher than that of the Ni51.42at.%-Mn29.25 at.%-Ga19.33 at.%, indicating that with the increase of the Ni content, the amount of NM martensite is increased.

#### 3.3.3.2 Influence of film thickness

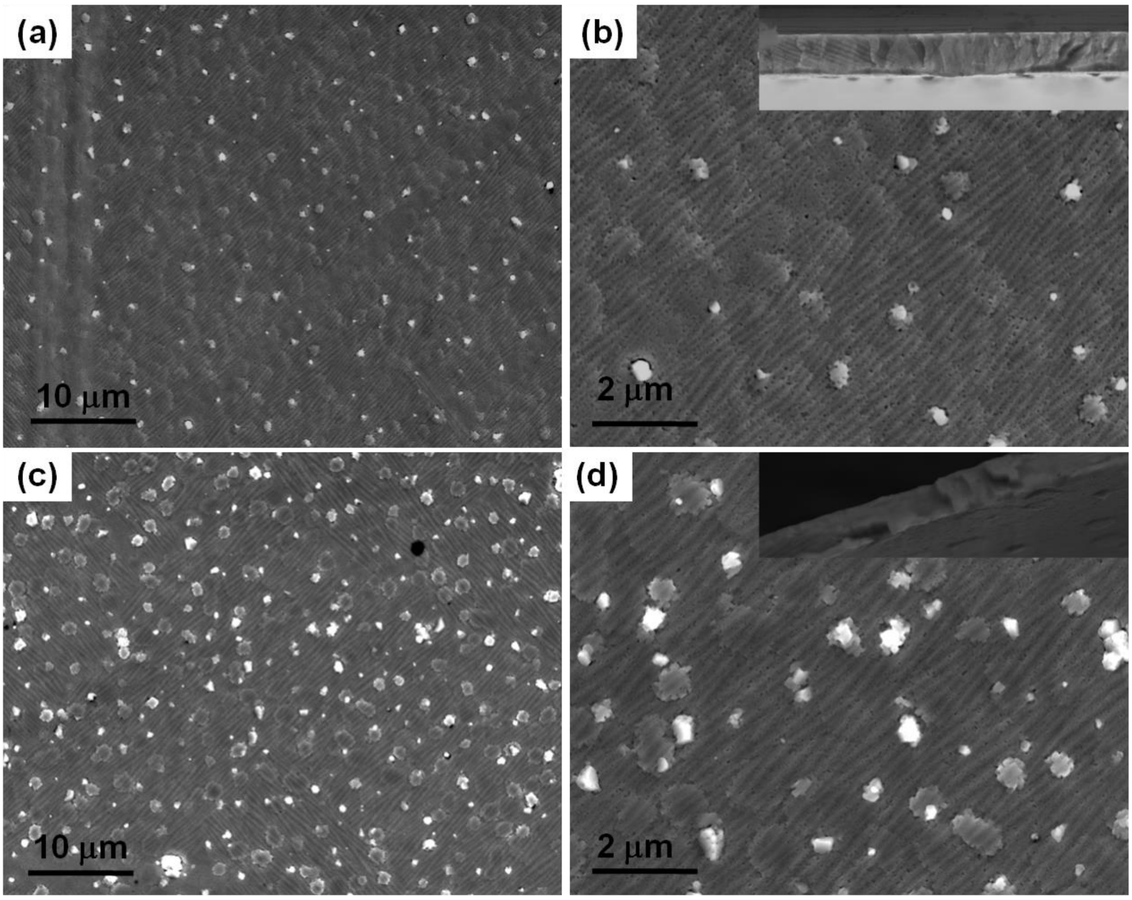

**Fig. 3.10** SEM image of MgO\Cr\NiMnGa thin films with different thicknesses (a-b)1.5 μm, (c-d) 3 μm.

Film thickness is an important parameter to be controlled. Usually, it is difficult to obtain thick epitaxial films. So far the studies on NiMnGa films are mainly on thin films with sub micrometer thickness.

Figure 3.10 presents the microstructure of MgO\Cr\NiMnGa thin film(composition?) with different thickness prepared in the present work. It is seen from the figures that with the increase of the film thickness, the amount of terrace shape constituents is increased. SEM-EDX analyses show that the composition of the terraces it is the same as that of the matrix. This indicates that with the increase of the depositing, the continuity of the film becomes deteriorated.

Fig.3.11 shows the X-ray diffraction patterns of the MgO\Cr\NiMnGa thin films with two different thicknesses. It is seen that both of them containing 7M and NM martensite. However, with the increase of the film thickness, the amount of NM martensite increases.

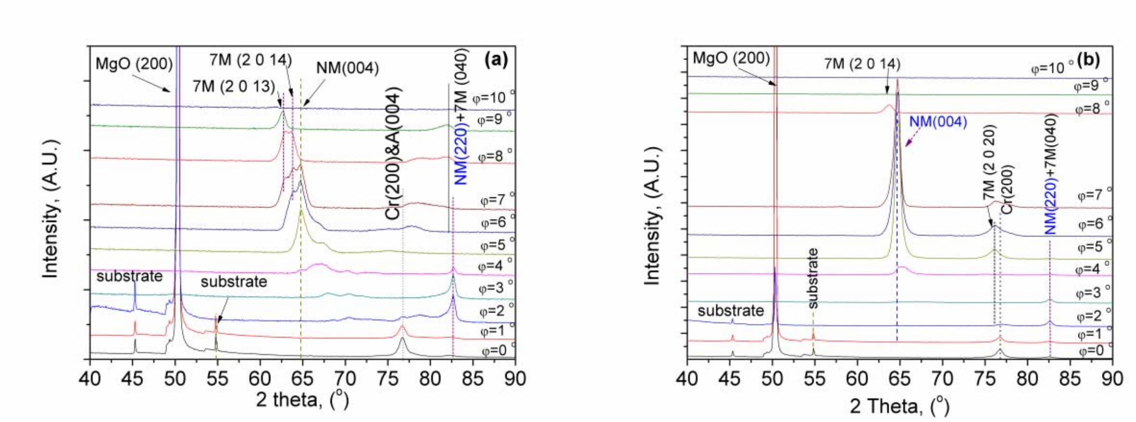

**Fig. 3.11** XRD patterns of MgO\Cr\NiMnGa thin films with two different thicknesses (a)1.5 μm, (b) 3 μm.

## 3.4 Discussion

When the sputtered atoms arrive at the substrate, a thin film is formed. The morphology, the microstructure and the crystallographic orientation of the thin films depend on the sputtering conditions, which has been depicted in a so-called structure zone model [101]. This model correlates the argon pressure and the substrate temperature to the morphological properties of the produced films. As shown in Fig.3.12, low argon pressure produces films with microstructures that are smooth and featureless while high argon pressure produces films with microvoids surrounding the amorphous islands. In addition, the grain growth and microstructure of deposited films is classified in different zones depending on the reduced temperature $T_S / T_M$ ($T_M$ is melting temperature, $T_S$ is the substrate temperature). High substrate temperature also produces films with continuous microstructure. However, in the present study, in order to fabricate NiMnGa thin films with continuous microstructure other than column microstructure, both the low argon pressure (0.15 Pa) and high substrate temperature (500 ℃) were employed. Maybe due to the limitations of the present depositing equipment, films with continuous microstructure were not attainable direct on the substrates without utilizing any seed layer. Introducing a seed layer proves to be an alternative. For the NiMnGa deposited on the MgO single crystal substrate, the Cr seed layer improves the element diffusion on the substrate, which results in the continuous microstructure.

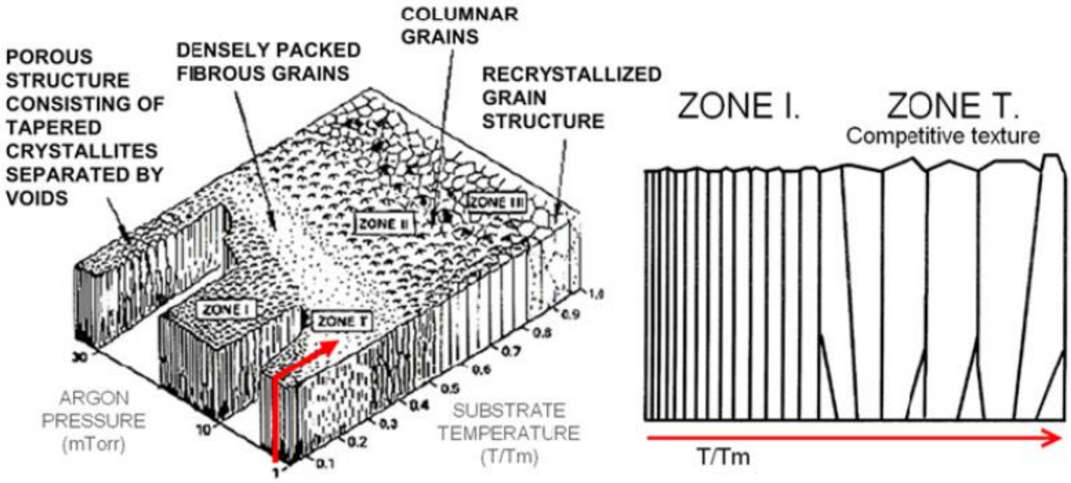

**Fig.3.12** Thornton structure zone model correlating the argon pressure and the substrate temperature to the morphological properties of the films [101].

## 3.5 Summary

In summary, NiMnGa thin films with continuous microstructures were successfully produced by DC magnetron sputtering, after the optimization of sputtering parameters such as substrate temperature, sputtering power, substrate materials, seed-layer materials, film composition and thickness. Low argon pressure, high substrate temperature and seed layer are necessary to fabricate the epitaxial NiMnGa thin films with continuous microstructure.

The optimum fabrication parameters to produce NiMnGa films with continuous microstructure and with martensite phase at room temperature are:

- Target material: Ni46at.%-Mn32at.%-Ga22at.%;
- Substrate: MgO(100) substrate with 100 nm Cr seed layer.
- working pressure: 0.15Pa;
- sputtering power: 75 w;
- substrate temperature 500 ℃;

# Chapter 4 Determination of crystal structure and crystallographic features by XRD

## 4.1 Introduction

A key requirement for considerable magnetic field-induced strains in ferromagnetic shape memory alloys, as reported for bulk NiMnGa samples, is the presence of modulated martensite. The precise knowledge of martensites in terms of crystal structure and crystallographic texture is of utmost importance. To conduct such characterizations, XRD techniques have been one of the privileged characterization techniques to analyze the phase constituents and texture components in many previous studies on NiMnGa epitaxial thin films [42, 45, 55, 87].

For crystal structure analyses of the constituent phases, the crystal structure of the cubic austenite and the tetragonal non-modulated (NM) martensite have been unambiguously determined from attainable XRD reflection peaks [45, 55, 84, 88]. However, for the monoclinic modulated martensite (7M or 14M), the lattice constant determination have suffered from insufficient number of measured reflection peaks [42, 44, 45, 55, 89], which result in the monoclinic angle of the crystal unattainable. Without knowing precisely the monoclinic angle, the monoclinic modulated martensite has to be simplified to a pseudo-orthorhombic structure [42, 44, 45, 55, 89]. The simplification to pseudo-orthorhombic structure makes the precise description of the orientation relationships between martensitic variants using well-defined twinning elements (such as twinning plane, twinning direction, and *etc.*) particularly difficult, especially when there are irrationally indexed twinning elements.

For crystallographic texture analyses, several studies have been performed on the preferred orientations of the two kinds of martensite. Special attention has been paid to link the orientation relationship between the two martensites, and to provide experimental evidences for the “adaptive phase model”.

In the chapter, the phase constituents and texture components of NiMnGa thin films were investigated by X-ray diffraction techniques. The crystal structure of modulated martensite and lattice constants expressed in monoclinic Bravais cell was fully determined and the texture characteristics were precisely detected.

## 4.2 Experimental

Ni-Mn-Ga thin films with nominal composition of $Ni_{50}Mn_{30}Ga_{20}$ and nominal thickness of 1.5 μm were deposited from a cathode target of $Ni_{46}Mn_{32}Ga_{22}$ by DC magnetron sputtering. A Cr buffer layer of 100 nm thick was pre-coated on the MgO(100) monocrystal substrate.

The crystal structures of the as-deposited NiMnGa thin films were determined by X-ray diffraction using Co-$K_\alpha$ radiation ($\lambda$ = 0.178897 nm). Considering that the thin films may possess in-plane texture, two four-circle X-ray diffractometers, one with a conventional θ–2θ coupled scan and the other with a rotating anode generator (RIGAKU RU300) and a large-angle position sensitive detector (INEL CPS120), were used to collect a sufficient number of diffraction peaks. The geometrical configurations of the two X-ray diffractometers are schematically illustrated in Fig. 2.3. In the former case (Fig. 2.3a), the θ–2θ coupled scans were performed between 45 ° and 90 ° at tilt angle ψ ranging from 0 ° to 10 ° with a step size of 1 °. In the latter case (Fig. 2.3b), the 2θ scans were conducted at tilt angle ψ from 0.75 ° to 78.75 ° with a step size of 1.25 °. At each tilt angle, the sample was rotated from 0 ° to 360 ° with a step size of 5 °. Two incident angles ω (27.9 ° and 40 °) were selected in order to obtain possible diffraction peaks at the low 2θ (48 °-58 °) and the high 2θ (around 82.5 °) regions. The final diffraction patterns were obtained by integrating all diffraction patterns acquired at different sample positions.

## 4.3 Results and discussion

### 4.3.1 Determination of crystal structure

Fig. 4.1a shows the *ψ*-dependent XRD patterns of the as-deposited Ni-Mn-Ga thin films obtained by conventional θ-2θ coupled scanning at ambient temperature. At each tilt angle *ψ*, there are only a limited number of diffraction peaks. Besides, no diffraction peaks become visible over the 2θ range of 48 °-55 °. This could be attributed to the texture effect of the as-deposited thin films, as several peaks at these positions were well observed in previous powder XRD measurements [63, 73].

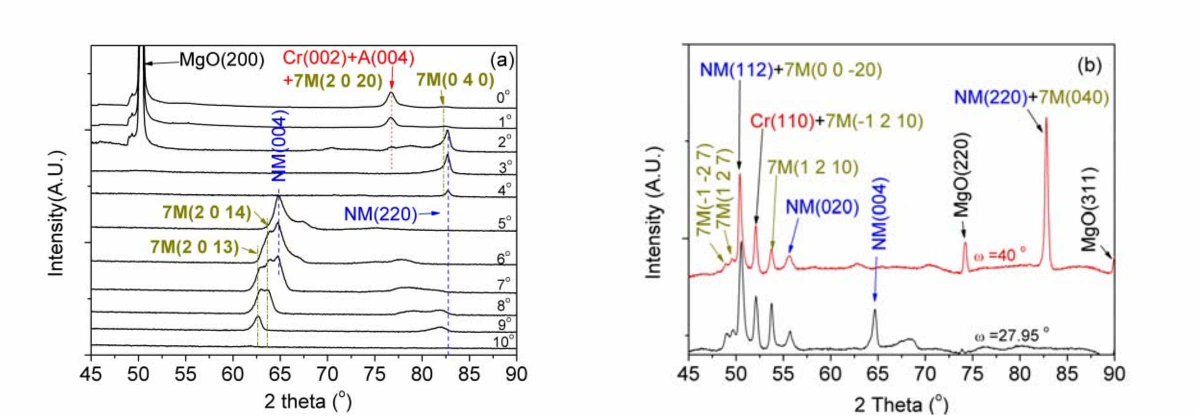

**Fig.4.1** XRD patterns of as-deposited Ni-Mn-Ga thin films with MgO/Cr substrate: (a) measured by conventional θ-2θ coupled scanning at different tilt angles ψ; (b) measured by 2θ scanning at two incidence angles ω and integrated over the rotation angle φ.

Fig. 4.1b presents the XRD patterns measured using a large-angle position sensitive detector under two different incident beam conditions. Compared with Fig. 4.1a, extra diffraction peaks are clearly seen in the 2θ range of 48°-55° and at the higher 2θ positions (around 82°). These additional peaks in the 2θ range of 48°-55° were not detected in the previous studies on the Ni-Mn-Ga thin films [42, 45, 55, 86, 88, 89]. By combining all the characteristic diffraction peaks in Figs. 4.1a and 4.1b, we are able to conduct more reliable phase identification and lattice constant determination on the constituent phases of the as-deposited thin films, especially for the modulated martensite.

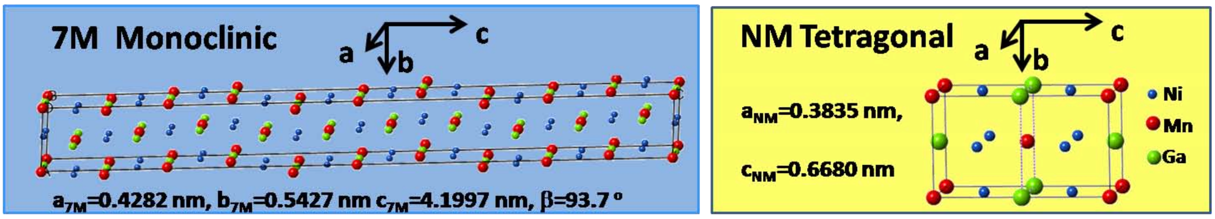

**Fig.4.2** the illustration of crystal structure of NM martensite and 7M martensite in NiMnGa thin films

As shown in Fig. 4.1, all the peaks are identified and indexed by comparing their positions with the calculated peak positions of all the three phases (austenite, NM martensite and 7M martensite) using the published crystal structure data [63, 72-74]. It is seen that peaks from the three phases co-exist in the measured spectra, indicating that the three phases co-exist in the deposited film.

A close look at the measured and calculated peak positions, we found that fairly good matches can be found between the measured and recalculated ones for the two kinds of martensite, although a deviation of 0.2~2 ° exists. The good fits confirm that the modulated martensite and the NM martensite possess the same crystal structure as their counterparts in bulk materials, whereas the angular deviations indicates that the lattice constants of the 7M and NM martensite in the as-deposited thin films are not exactly the same as the ones derived from their powder counterparts, as the substrate imposes a constraint on the as-deposited thin films during the phase transitions. Using the measured peak positions of each phase, the lattice constants of the 7M and NM martensite were resolved. Table 4.1 summarizes the complete crystal structure information on the three different phases (austenite, 7M martensite, and NM martensite) involved in the as-deposited thin films. The unit cell of the 7M and NM martensite is shown in Fig. 4.2. This information is prerequisite for the subsequent EBSD orientation analyses.

**Table 4.1.** Calculated lattice constants of austenite, 7M martensite and NM martensite for as-deposited Ni-Mn-Ga thin films.

| Phase | Space group | Crystal system | Lattice constants | | | |
|---|---|---|---|---|---|---|
| | | | *a* (nm) | *b* (nm) | *c* (nm) | $\alpha, \beta, \gamma$ |
| 7M | *P2/m* (No. 10) | Monoclinic | 0.4262 | 0.5442 | 4.199 | $\alpha=\gamma=90°$, $\beta= 93.7°$ |
| NM | *I4/mmm* (No. 139) | Tetragonal | 0.3835 | 0.3835 | 0.6680 | $\alpha=\beta=\gamma=90°$ |
| Austenite | $Fm\bar{3}m$ (No.225) | Cubic $L2_1$ | 0.5773 | 0.5773 | 0.5773 | $\alpha=\beta=\gamma=90°$ |

### 4.3.2 Determination of crystallographic texture

Fig.4.3 presents the pole figures of NM martensite and 7M martensite. Let the edges of MgO substrate as the macroscopic sample coordinate system as shown in Fig.4.3(a) and the crystal direction of $[100]_{\mathrm{MgO}}$ parallel to the starting position of the azimuth angle. It should be noted that the pole figures are incomplete pole figures. Only the central part of these pole figures was shown, since the martensites of NiMnGa possess strong in-plane texture and the information in the central part is enough to represent the texture characteristics of the film.

It is seen that from Fig.4.3 the NM martensite is with its $(004)_{\mathrm{Tetr}}$ or $(220)_{\mathrm{Tetr}}$ close to the substrate surface, demonstrating a typical plane texture, while 7M martensite is with its $(2\ 0\ 20)_{\mathrm{mono}}$, $(2\ 0\ \overline{20})_{\mathrm{mono}}$ or $(0\ 4\ 0)_{\mathrm{mono}}$ close to the substrate surface, also demonstrating a plane texture. It should be mentioned that for the $(2\ 0\ 20)_{mono}$ pole figure, the central pole is originated from the $(2\ 0\ 20)_{mono}$ plane of 7M martensite and $(004)_A$ plane of austenite. The four poles with 6° tilt angle are from the diffraction of $(2\ 0\ 23)_{mono}$ plane. Due to the structure modulation of 7M martensite, the two planes possess very close interplanar spacing.

As shown in Fig.4.3, the high intensity pole areas are clearly separated and distributed symmetrically with respect to the film surface normal. This indicates that the film possesses several strong preferred orientations that may be related to the specific orientation of different martensite variants. As XRD measurements capture only global orientation information from the film and the pole figures represent this global information with respect to the macroscopic sample coordinate system, it is difficult to correlate the poles with individual martensite variants in the microstructure. To further resolve such information, Local SEM-EBSD orientation determination is needed.

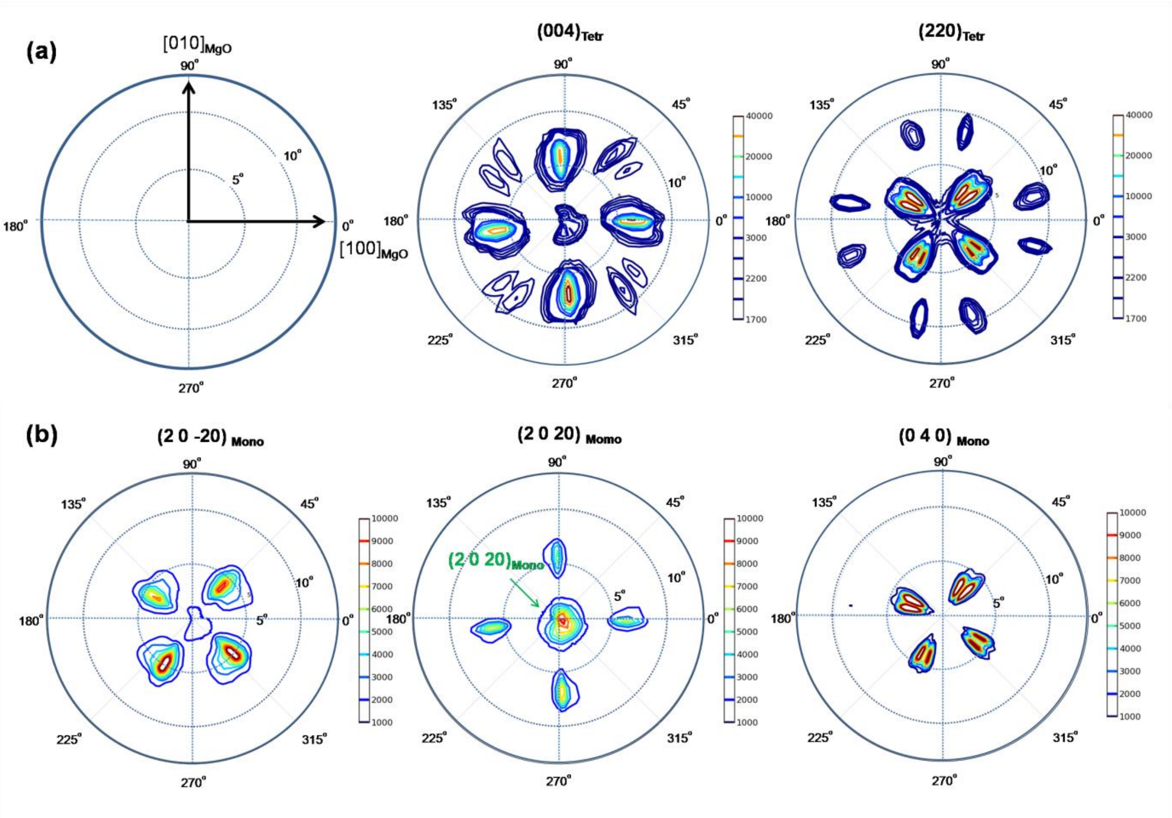

**Fig. 4.3** Pole figures of NM and 7M martensite in NiMnGa thin films (a) NM martensite, (b) 7M martensite

It should be noted that the macroscopic crystallographic features obtained in the present work are similar to those identified in the previous studies [42, 89]. The only difference is that choice of the lattice cell for the two martensite is not the same. The $(2\ 0\ 20)_{mono}$, $(2\ 0\ \overline{20})_{mono}$ and $(0\ 4\ 0)_{mono}$ planes in the present work refer to the respective $(0\ 4\ 0)_{orth}$, $(4\ 0\ 0)_{orth}$ and $(0\ 0\ 4)_{orth}$ planes in the pseudo-orthorhombic coordinate system [42, 89], whereas the $(004)_{Tetr}$ and $(220)_{Tetr}$ planes refer to the respective $(004)_{NM}$ and $(400)_{NM}$ in the previous studies [42, 89].

## 4.4 Summary

X-ray crystal structural analysis shows that three different phases, *i.e.* austenite, 7M modulated martensite, and NM martensite, co-exist in the as-deposited $Ni_{50}Mn_{30}Ga_{20}$ thin films. The austenite phase has a cubic $L2_1$ crystal structure ($Fm\bar{3}m$, No. 225) with lattice constant $a_A = 0.5773$ nm. The 7M martensite phase has an incommensurate monoclinic crystal structure ($P2/m$, No. 10) with lattice constants $a_{mono} = 0.4262$ nm, $b_{mono} = 0.5442$ nm, $c_{mono} = 4.1997$ nm, and $\beta = 93.7^{o}$. The NM martensite phase is of tetragonal crystal structure ($I4/mmm$, No. 139) with lattice constants $a_{Tetr} = 0.3835$ nm and $c_{Tetr} = 0.6680$ nm.

Pole figures revealed that the NM martensite possesses $(004)_{Tetr}$ and $(220)_{Tetr}$ plane texture close to the substrate surface, while 7M martensite have $(2\ 0\ 20)_{mono}$, $(2\ 0\ \overline{20})_{mono}$ and $(0\ 4\ 0)_{mono}$ plane texture close to the substrate surface. To correlate the poles in the pole figures with the orientation of individual martensite variants, SEM-EBSD characterization is a pertinent characterization technique.

# Chapter 5 Determination of crystallographic features of epitaxial NiMnGa thin films by EBSD

## 5.1 Introduction

The type and character of martensite variant boundaries (usually twin boundaries in NiMnGa alloys) are dominant factors for magnetic-field-induced strains in NiMnGa ferromagnetic shape memory alloys, as type II twin boundaries of modulated martensite possess higher mobility than that of others. For bulk materials, these factors have been well clarified through direct orientation determination on individual martensitic variants. As for thin films, only the so-called $a_{14M}$-$c_{14M}$ twin interfaces could be deduced by examining X-ray pole figures and local surface morphologies. To determine the twin relationship and precise twinning elements, local crystallographic orientation correlated with microstructure is the prerequisite information.

In this chapter, a spatially-resolved orientation analysis is conducted on martensites of NiMnGa thin films by means of electron backscatter diffraction (EBSD) – a SEM based microstructural-crystallographic characterization technique. The microstructural features of both NM martensite and 7M modulated martensitic variants are directly correlated with their crystallographic orientations. The roles of substrate constraint in the preferential selection of martensitic variants are addressed. Based on the crystallographic calculation the martensitic transformation sequence in the present NiMnGa thin films was verified.

## 5.2 Experimental procedure

The microstructures and crystallographic orientations of the thin films with nominal composition (at.%) of $Ni_{50}Mn_{30}Ga_{20}$ and nominal thickness of 1.5 μm were analyzed using the same SEM equipped with an EBSD system, where the EBSD patterns from martensitic variants were manually acquired using Channel 5 Flamenco’s interactive option. Prior to the microstructural observations and orientation measurements, the thin film samples were subject to thickness-controlled electrolytic polishing with a solution of 20%$HNO_3$ in $CH_3OH$ at 12 volts at room temperature.

NiMnGa thin films were also investigated by transmission electron microscope (TEM) with 200 kV accelerating voltage. Specimens for TEM investigation were cut off out the freestanding NiMnGa thin film and further thinned using twin-jet electrolytic polishing with an electrolyte of 20% $HNO_3$ in volume in $CH_3OH$ at ambient temperature.

## 5.3 Results

### 5.3.1 Microstructure of epitaxial NiMnGa thin films

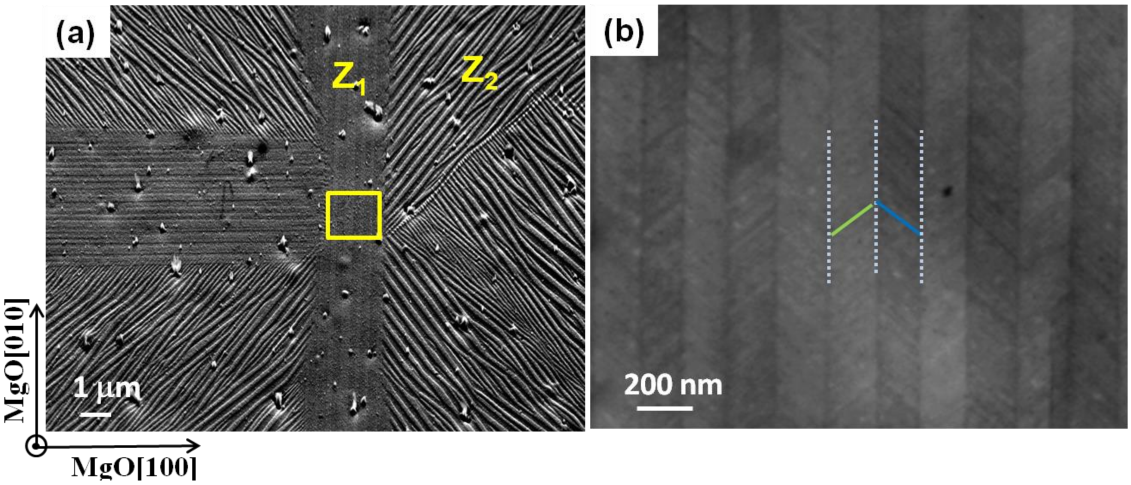

**Fig.5.1** SE image of electrolytically polished Ni-Mn-Ga thin films, showing martensite plates that are clustered in groups with low and high relative contrasts. The sample coordinate system is set in accordance with the basis vectors of the MgO substrate. (b) High-magnification BSE image of the squared area $Z_1$ in Fig. 5.1a, showing fine lamellae distributed alternately inside each plate. The inter-plate interfaces are marked with white dotted lines, and the intra-plate interfaces with blue and green solid lines.

Fig.5.1(a) shows a SE image of the as-deposited thin films after slight electrolytic polishing. It is clearly seen that the martensite appears in plate shape, and individual plates are clustered into groups that can be distinguished locally by the alignment of parallel or near-parallel inter-plate boundaries. According to the SE image contrast of neighboring martensite plates, the clustered groups are characteristic of two different relative contrasts - low relative contrast ($Z_1$) or high relative contrast ($Z_2$), as illustrated in Fig.5.1(a). Whereas the low relative contrast zones consist of long and straight plates running with their length direction parallel to one edge of the substrate (*i.e.* $[100]_{\mathrm{MgO}}$ or $[010]_{\mathrm{MgO}}$), the high relative contrast zones are of shorter and somewhat bent plates that orient roughly at 45° with respect to the substrate edges. In fact, the SE image contrast is related to the surface topography of an observed object. Thus, the low relative contrast zones and the high relative contrast zones are expected to have low and high surface reliefs, respectively.

Further examination at a higher magnification in backscattered electron imaging (BSE) mode reveals that the fine lamellae having two different brightness levels are distributed alternately inside each plate, as highlighted with green and blue lines in Fig. 5.1(b). Of the two contrasted neighboring lamellae, one is thicker and the other is thinner. As the BSE image contrast for a monophase microstructure with homogenous chemical composition originates from the orientation differences of the microstructural components, the thicker and thinner lamellae distributed alternately in each plate should be correlated with two distinct orientations.

Fig. 5.2(a) presents the secondary electron (SE) image acquired from the sample with gradient thickness film thickness. This sample was prepared by a controlled polishing to obtain an increased polishing depth from the left to the right, as schematically illustrated in Fig. 5.2(b). The right side and the left side of Fig. 5.2(a) represent the microstructure near the film surface and that deep inside the film, respectively. It can be seen from Fig. 5.2(a) that the thin film has an overall plate-like microstructure, with plate thickening from its interior to its surface. Although the polishing depth of the film changes smoothly, an abrupt change in the plate thickness occurs without any transition zone. This indicates a complete change of microstructural constituents or phases along the film thickness.

The crystal structures of the coarse plates in the near surface layer of the film and fine plates well under the film surface were further verified by EBSD, using the determined crystal structure information for the 7M and NM martensite. Fig. 5.2(c) and Fig. 5.2(f) present the respective Kikuchi patterns, acquired from one coarse plate (with high brightness in the dotted blue square of Fig. 5.2(a)) and one thin plate (with high brightness in the dotted yellow square of Fig. 5.2(a)). Obviously, the measured patterns bear intrinsic differences, as arrowed in Fig. 5.2(c) and Fig. 5.2(f). Fig. 5.2(d) and Fig. 5.2(e) demonstrate that each of the two overlapping patterns appeared in Fig. 5.2(c) can be indexed with the tetragonal crystal structure of the NM martensite. It means that one coarse plate in the top surface layer of the film contains two NM martensitic variants. This is coherent with the BSE observations, shown in Fig. 5.1(b).

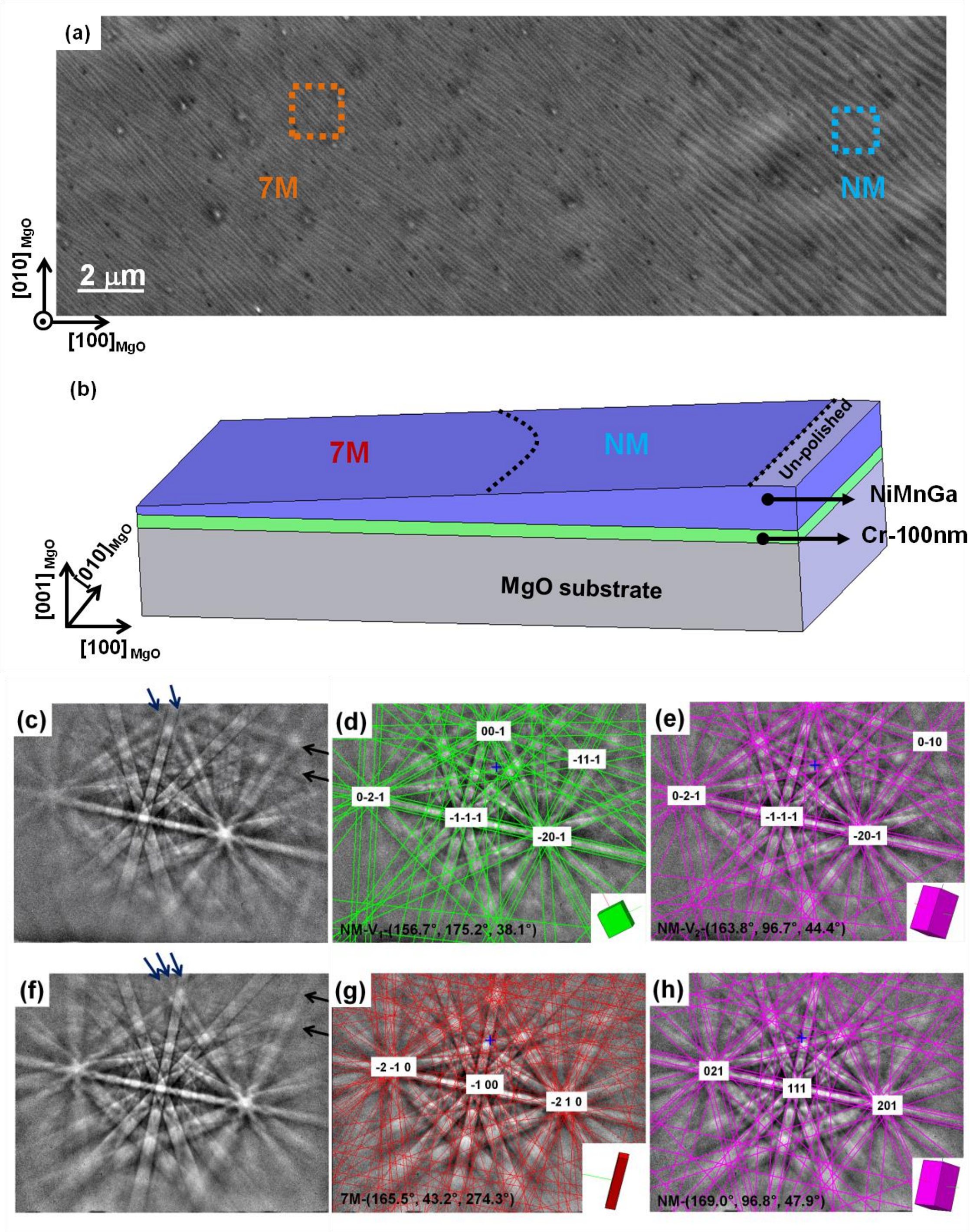

**Fig.5.2.** (a) SE image showing the plate-like microstructure of an electropolished sample with gradient film thickness. (b) Schematic illustration of the sample thickness change from the left side to the right side, produced by gradually electrolytic polishing. (c-e) Kikuchi patterns acquired from one coarse plate with high brightness in the dotted blue square of Fig. 5.2a. The mixed patterns in Fig. 1c are indexed as two NM variants (Fig. 5.2d and Fig. 5.2e) with Euler angles of (156.7°, 175.2°, 38.1°) and (163.8°, 96.7°, 44.7°), respectively. (f) Kikuchi pattern acquired from one fine plate with high brightness in the dotted yellow square of Fig. 5.2a. (g and h) Calculated Kikuchi patterns using the monoclinic superstructure of 7M martensite and the tetragonal structure of NM martensite, respectively. Note that in the latter case there appear large mismatches with the measured Kikuchi pattern.

In contrast, the pattern in Fig. 5.2(f) represents a single pattern and can be well indexed with the monoclinic superstructure of the 7M martensite (Fig. 5.2(g)). Large misfits between the acquired and calculated patterns are generated if using the tetragonal crystal structure of the NM martensite (Fig. 5.2(h)) to index this pattern. In this context, the coarse plates in the top layer of the film are composed of the NM martensite, whereas the fine plates in the film interior are of the 7M martensite. By taking into account of the X-ray measurement results, one may deduce that the NM martensite is located near the free surface of the film, the austenite above the substrate surface, and the 7M martensite in the intermediate layers between them.

### 5.3.2 Crystallographic features of NM martensite

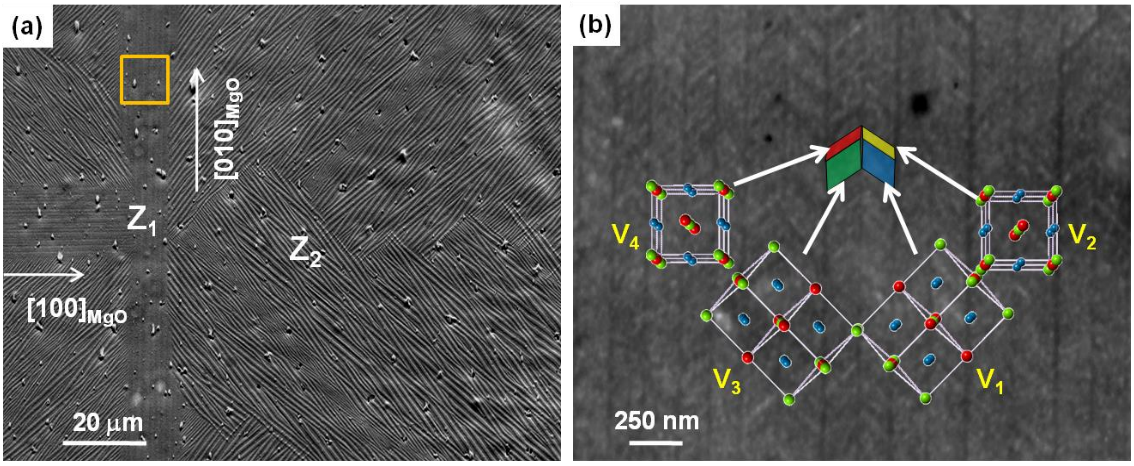

**Fig.5.3** (a) SE image of the as-deposited thin films after slight electrolytic polishing. (b) High-magnification BSE image of the squared area $Z_1$ in Fig. 5.3(a). The insets represent the crystallographic orientation of the major and minor lamella variants. $V_1$ and $V_2$ are the major and minor variants in one martensite plate. $V_3$ and $V_4$ are the major and minor variants in the left adjacent martensite plate.

Using the determined lattice constants of the NM and 7M martensites and the published atomic position data [63] as initial input, the constituent phases in the surface layers of the as-deposited thin films were verified by EBSD analysis. The Kikuchi line indexation has evidenced that both low and high relative contrast zones displayed in Fig. 5.3(a) can be identified as the tetragonal NM martensite other than the 7M martensite. Fig. 5.4 presents an example of the Kikuchi line pattern acquired from one martensite plate with high brightness in the high relative contrast zone and the calculated patterns using the tetragonal NM martensite structure. As the in-plate lamellar variants are too fine and beyond the resolution of the present

EBSD analysis system, we could not obtain a single set of Kikuchi lines from one variant. For each acquisition, there are always mixed patterns from two neighboring variants in one image, as displayed in Fig. 5.4(a). However, the high intensity reflection lines belonging to two different variants can be well separated in the image, as outlined by the green and red triangles in Fig. 5.4(b). By comparing Figs. 5.4(c) and 5.4(d) with Fig. 5.4(a), perfect matches between the acquired Kikuchi lines for the two variants and the calculated ones using the tetragonal NM martensite structure are evident.

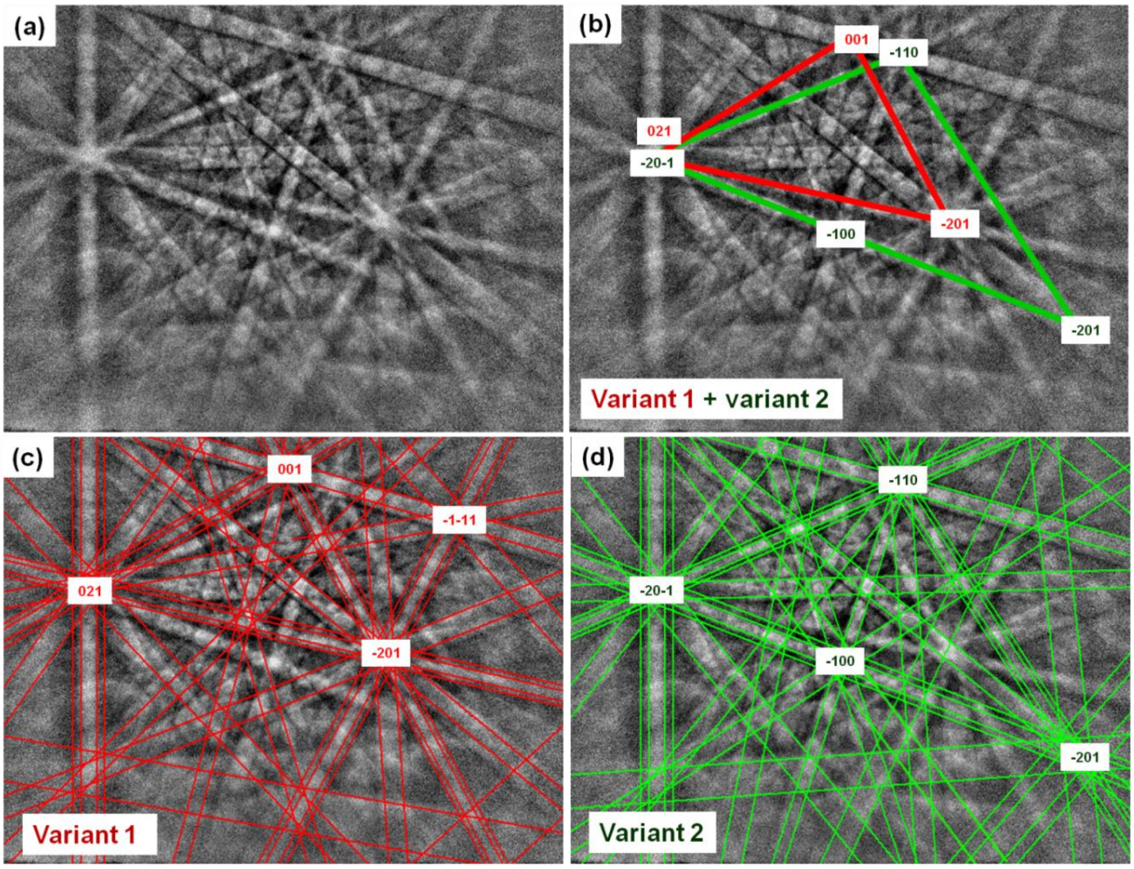

**Fig. 5.4.** (a) Kikuchi line pattern acquired from one martensite plate in the high relative contrast zone ($Z_2$) in Fig. 5.3a. (b) Indication of high intensity reflection lines from two adjacent variants 1 (the green triangle) and 2 (the red triangle). (c-d) Calculated Kikuchi line patterns using the tetragonal structure for variants 1 and 2, respectively.

Apparently, there is a difference in interpreting the microstructural features of Ni-Mn-Ga thin films between the present result and previous work by other groups [42-44, 55, 82, 85, 86, 88, 89]. This may be related to the different thickness of thin films used for microstructural characterizations. In the present study, the NM martensite was found at the surface of the produced thin films of about 1.5 μm thick, while the others reported the existence of the 7M martensite at the surface of the thin films with maximum thickness of about 0.5 μm. Indeed, the formation of different types of martensite is very sensitive to local constraints. It is obvious that at the film surface, the constraint from the substrate decreases with the increasing film thickness. Thus, the surface layers of thick films without much constraint from substrate would easily transform to the stable NM martensite, as demonstrated in the present case.

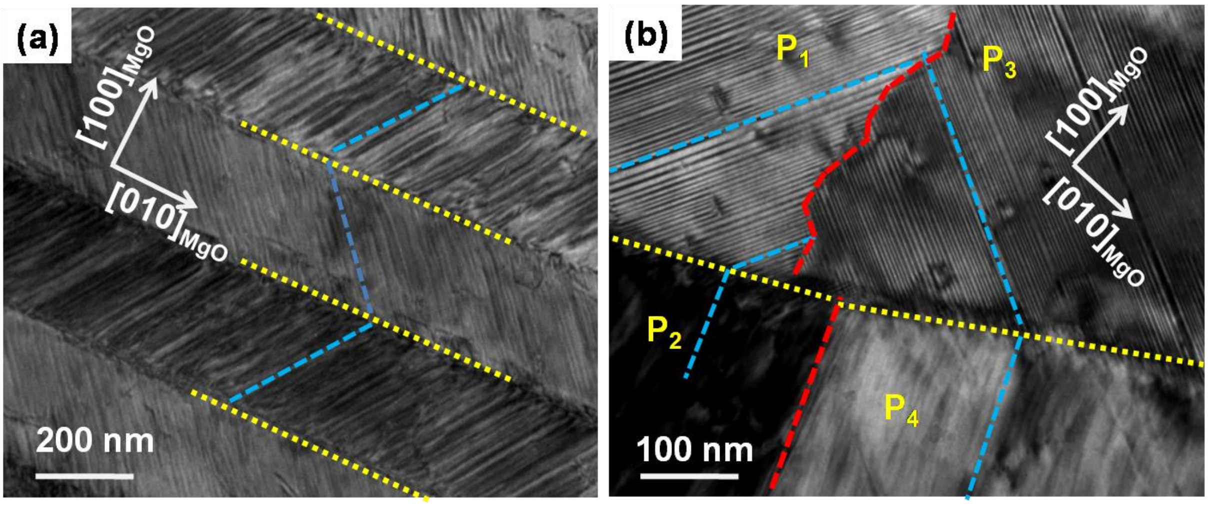

**Fig.5.5** The TEM bright field image of NiMnGa thin films (a) the low relative contrast zone, (b) the high relative contrast zone. The yellow dotted lines represent traces of the inter plate interfaces. The blue dashed lines represent traces of the intra plate interfaces.

The two characteristic organizations of variants in the relative low contrast and high contrast zones have been further confirmed by TEM examinations, as presented by TEM bright field images in Fig. 5.5. As shown in Fig.5.5, the low relative contrast zones are composed of long and straight plates (Fig. 5.5(a)), whereas the high relative contrast zones are composed of bent plates (Fig.5.5(b)). There is only one interface trace direction (yellow dotted lines in Fig. 5.5 (a)) in the low contrast zone, whereas there are two interplate interface trace directions (yellow dotted lines) in the high relative contrast zone. In both the low and high relative contrast zones, the fine lamella inside each plate could be clearly seen, as outlined by the blue dotted lines in the figures. From Fig. 5.5(b), it is seen that the bending of the plate in the high relative contrast zone is realized by orientation change of the fine lamellae, as indicated by the red dotted lines in the figure.

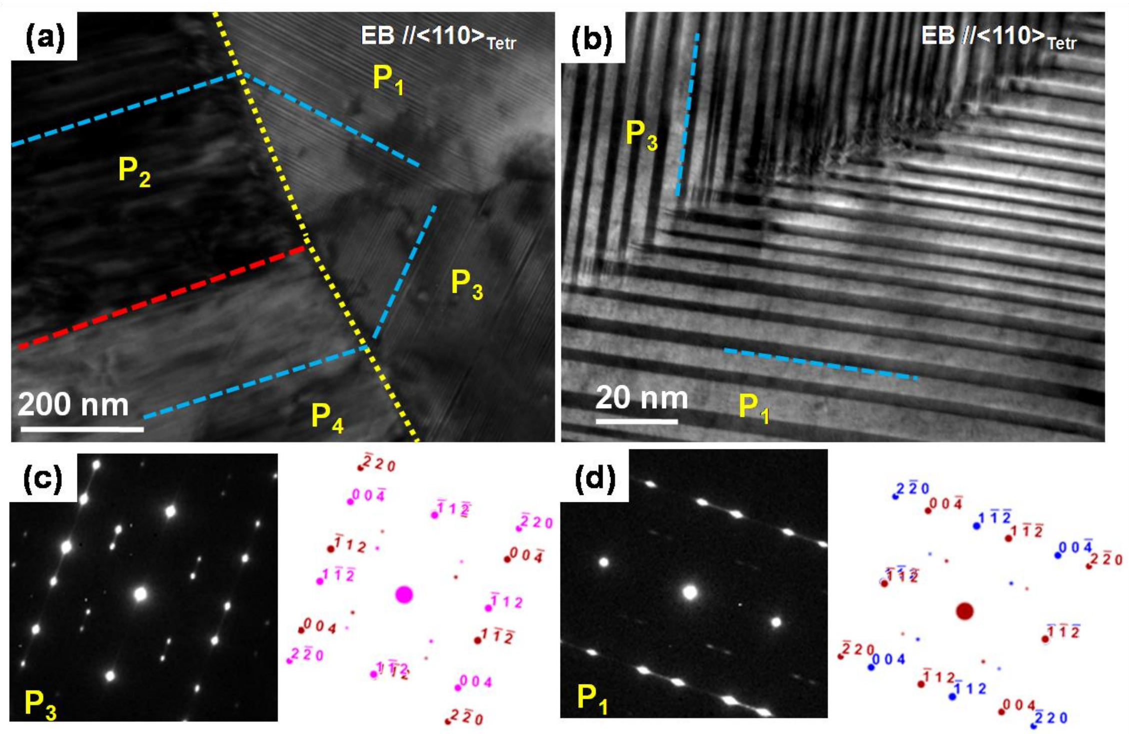

**Fig.5.6** The TEM bright field image in the high relative contrast zones of NiMnGa thin films (a-b) and the corresponding diffraction patterns of $P_1$ and $P_3$ (c-d). The yellow dotted lines represent traces of the inter plate interfaces. The blue dashed lines represent traces of the intra plate interfaces. Here the electron beam is parallel to the $<110>_{Tetr}$ zone axes of $P_1$ and $P_3$.

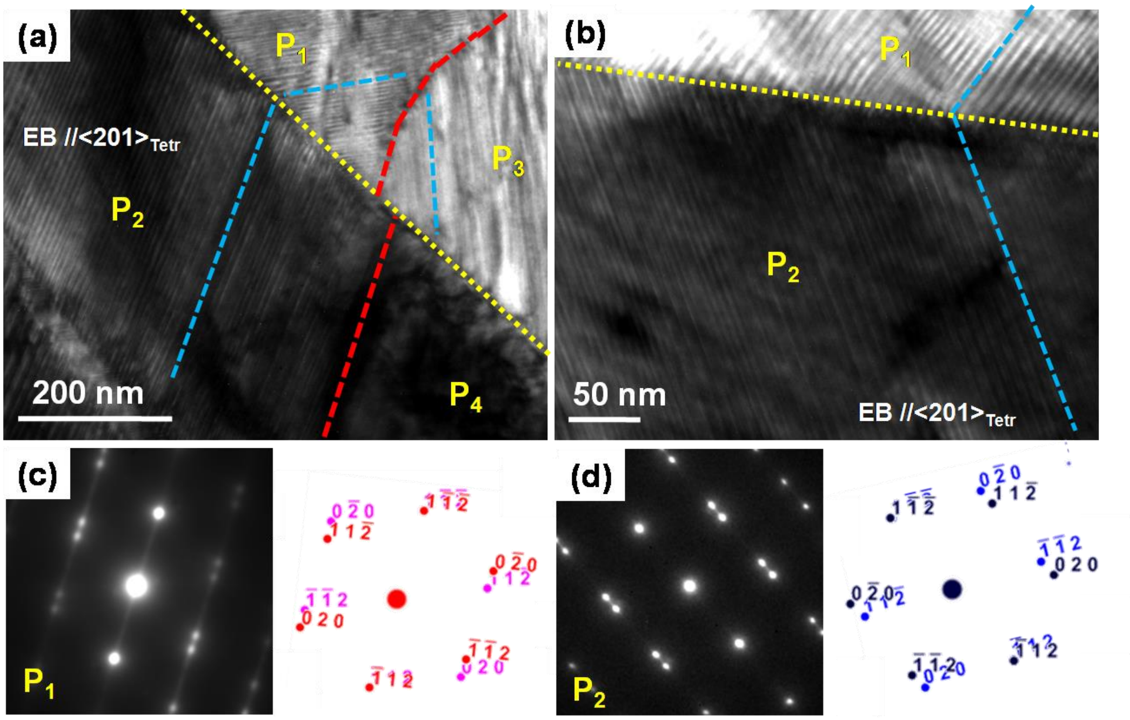

**Fig.5.7** The TEM bright field image in the high relative contrast zones of NiMnGa thin films (a-b) and the corresponding diffraction patterns of $P_1$ and $P_2$ (c-d). Here the electron beam is parallel to the $<201>_{Tetr}$ zone axes of $P_1$ and $P_2$.

Fig. 5.6 and 5.7 show the TEM bright field images from the same area displayed in Fig. 5.5(b) acquired in two specific incident beam conditions (beam//$<110>_{Tetr}$ in Fig. 5.6 and beam//$<201>_{Tetr}$ in Fig. 5.7). The beam//$<110>_{Tetr}$ condition allows the $\{\bar{1}12\}_{Tetr}$ lamellar interfaces in $P_1$ and $P_3$ to be on edge, as shown in Fig. 5.6, and the beam//$<201>_{Tetr}$ permits the $\{\bar{1}12\}_{Tetr}$ lamellar interfaces in $P_1$ and $P_2$ to be on edge, as shown in Fig. 5.7. The selected area diffraction patterns acquired from plate $P_1$ and $P_3$ in Fig. 5.6 and $P_1$ and $P_2$ in Fig. 5.7 well revealed that the adjacent fine lamellae in the same plate have their $\{\bar{1}12\}_{Tetr}$ in parallel. This further confirms the compound twin relationship between them.

### 5.3.2.1 Orientation correlation

Detailed EBSD orientation analyses were conducted on the NM martensite plates in the low and high relative contrast zones ($Z_1$ and $Z_2$ in Fig. 5.3(a)). Individual plates were identified to be composed of two alternately distributed orientation variants (lamellae) with different thicknesses, as schematically illustrated in Fig. 5.8(a) and 5.8(b). The clustered martensite plates running parallel to the substrate edges ($Z_1$) represent one kind of variant group, whereas those running roughly at 45 ° to the substrate edges ($Z_2$) represent another kind. According to the orientations of the thicker variants in plates, two sets of orientation plates can be distinguished, *i.e.* the set of plates A, B, C and D in the low relative contrast zones and the set of plates 1, 2, 3 and 4 in the high relative contrast zones. Thus, there are in total eight orientation variants of the NM martensite in one variant group. For easy visualization, they are denoted as $V_1$, $V_2$, …, $V_8$ in Fig. 5.8(a) and $SV_1$, $SV_2$, …, $SV_8$ in Fig. 5.8(b), where the symbols with odd subscripts correspond to the thicker (major) variants and those with even subscripts the thinner (minor) variants. Taking the basis vectors of the MgO(100) monocrystal substrate as the sample reference frame, as defined in the "Experimental" part, the measured orientations of the NM variants in the two relative contrast zones are presented in the form of $\{001\}_{Tetr}$, $\{110\}_{Tetr}$, $\{010\}_{Tetr}$ and $\{112\}_{Tetr}$ pole figures, as displayed in Figs. 5.8(c) and Fig. 5.8(d).

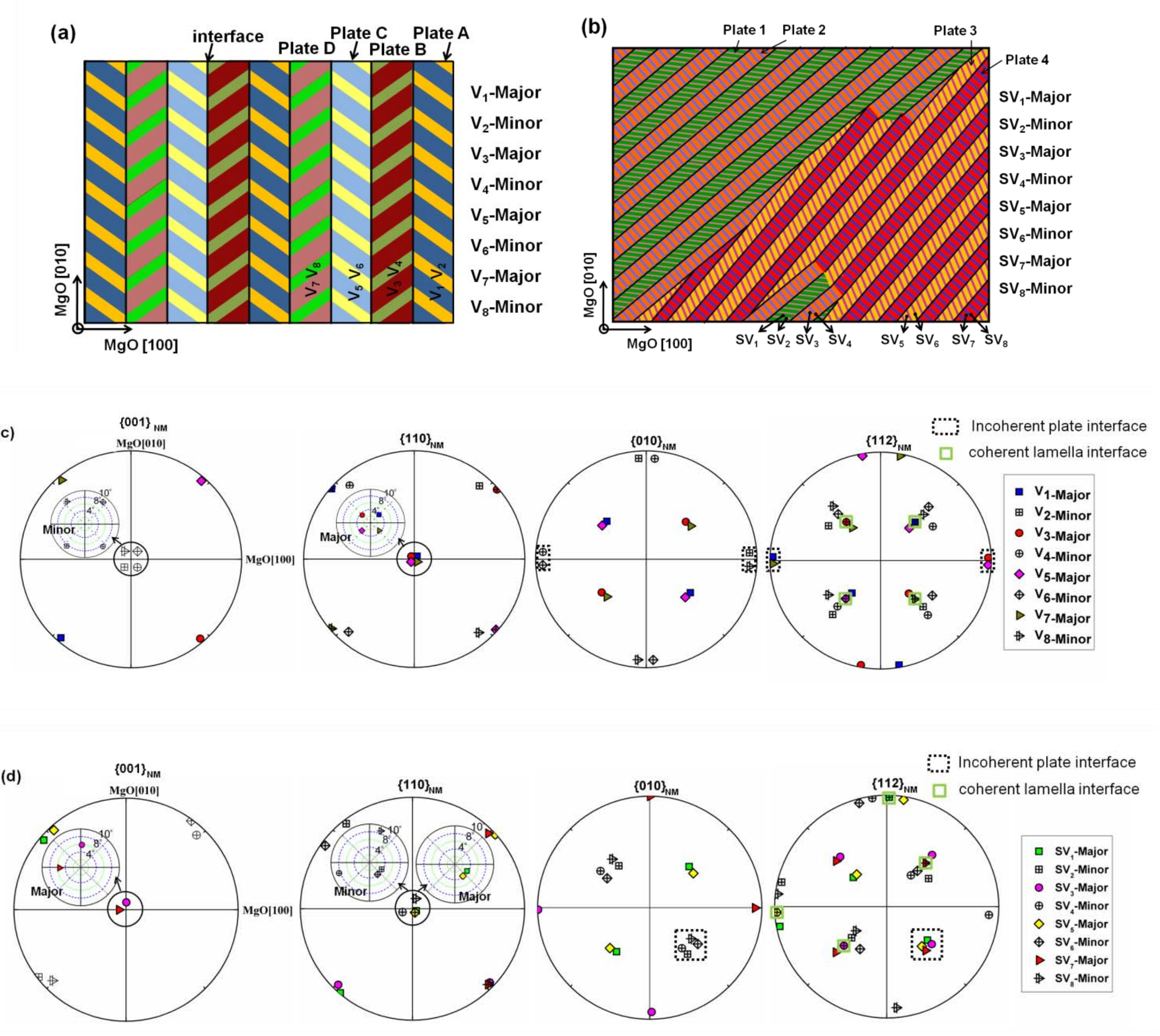

**Fig. 5.5.** (a-b) Schematic illustration of the geometrical configuration of NM plates. $V_1$, $V_2$, …, $V_8$ and $SV_1$, $SV_2$, …, $SV_8$ denote eight orientation variants in the low relative contrast zones ($Z_1$) and in the high relative contrast zones ($Z_2$), respectively. (c-d) Representation of measured orientations of in-plate lamellar variants in the form of $\{001\}_{Tetr}$, $\{110\}_{Tetr}$, $\{010\}_{Tetr}$ and $\{112\}_{Tetr}$ pole figures. The orientations of the intra- and inter-plate interface planes are respectively indicated by light green solid squares and black dotted rectangles in the $\{010\}_{Tetr}$ and $\{112\}_{Tetr}$ pole figures.

It is noted that the orientations of the major and minor variants in the low relative contrast zones are different from those in the high relative contrast zones. For the low relative contrast zones ($Z_1$), the major and minor variants are oriented respectively with their $(110)_{Tetr}$ planes and $(001)_{Tetr}$ planes nearly parallel to the substrate surface (Fig. 5.8(c)). In the high relative contrast zones ($Z_2$), such plane parallelisms hold for plates 2 and 4 but with an exchange of the planes between the major and minor variants, whereas both major and minor variants in plates 1 and 3 are oriented with their $(110)_{Tetr}$ planes nearly parallel to the substrate surface (Fig. 5.8(d)). In correlation with the microstructural observations, plates 2 and 4 are featured with higher brightness and plates 1 and 3 with lower brightness.

#### 5.3.2.2 Misorientation relationships

Based on the misorientation calculations in part 2.3.2 and Eq.(2-17), the orientation relationships between adjacent lamellar variants were further determined from their orientation data manually acquired by EBSD. For both low and high relative contrast zones, the in-plate lamellar variants are found to have a compound twin relationship with the twinning elements $\mathbf{K}_1 = (112)_{Tetr}$, $\mathbf{K}_2 = (11\bar{2})_{Tetr}$, $\boldsymbol{\eta}_1 = [11\bar{1}]_{etr}$, $\boldsymbol{\eta}_2 = [111]_{Tetr}$, $P = (1\bar{1}0)_{Tetr}$ and $s = 0.412$. Here, all the crystallographic elements are expressed in the crystal basis of tetragonal Bravais lattice for the convenience in interpreting the EBSD orientation data and introducing the symmetry elements of the tetragonal structure to find proper misorientation axes and angles. The present twin relationship is the same as that reported for the bulk alloys [69, 95], and it is also consistent with the so-called *a*-*c* twin relationship found in the thin films [34, 43, 44, 82, 88, 89].

By means of the indirect two-trace method [102], the in-plate interlamellar interface planes in the two relative contrast zones were further determined. They coincide well with the $(112)_{Tetr}$ twining plane (roughly corresponding to the (101) planes of the austenite [44, 55, 88, 89]) and are perfectly coherent, as indicated by the light green solid squares in Figs. 5.8(c) and 5.8(d). According to the $\{112\}_{Tetr}$ pole figure of the low relative contrast zones shown in Fig. 5.8(c), the interlamellar interfaces in each plate are inclined roughly 47.5 °toward the substrate surface, and two interlamellar interfaces from adjacent plates are positioned symmetrically either to the $(010)_{MgO}$ plane (*e.g.* plates A and B) or to the $(100)_{MgO}$ plane (*e.g.* plates B and C). As for the high relative contrast zones (Fig. 5.8(d)), the interlamellar interfaces in one plate (*e.g.* plate 1) are roughly perpendicular (88.6 °) to the substrate surface. Whereas, the interlamellar interfaces in its neighboring plates (*e.g.* plate 2) are inclined 44.4 °toward the substrate surface.

Moreover, the orientation relationships between two lamellae connected by an inter-plate interface in the low and high relative contrast zones were calculated. The respective minimum rotation angles and the corresponding rotation axes are displayed in Table 5.1 and Table 5.2. The counterpart major and minor variants in adjacent plates are related by a rotation of ~83 ° around the $<110>_{Tetr}$ axes and a rotation of ~11-14 ° around the $<301>_{Tetr}$ axes with certain degrees of deviation, respectively. For the low relative contrast zones, the closest atomic planes from the counterpart major variants are referred to the $(1\bar{1}2)_{Tetr}$ planes with an angular deviation of 1.9° and those from the counterpart minor variants to the $\{010\}_{Tetr}$ planes with an angluar deviation of 4.2°, as outlined with black dotted rectangles in the $\{010\}_{Tetr}$ and $\{112\}_{Tetr}$ pole figures in Fig. 5.8(c). These characteristic planes are all nearly perpendicular to the substrate surface and the corresponding planes of the counterpart major and minor variants are positioned symmetrically to the $(010)_{MgO}$ plane. As for the high relative contrast zones (Fig. 5.8(d)), the closest atomic planes from the counterpart major and minor variants are respective of the $(\bar{1}12)_{Tetr}$ and $(010)_{Tetr}$, similar to the case in the low relative contrast zones. However, they are no longer perpendicular to the substrate surface. Detailed calculations on plates 1 and 2 show that their $(\bar{1}12)_{Tetr}$ planes are inclined to the substrate surface at 42.57° and 47.24°, and the $(010)_{Tetr}$ planes are at 48.29° and 41.68°, respectively.

**Table5.1.** Minimum rotation angle and rotation axis between two lamellar variants connected by an inter-plate interface in the low relative contrast zones.

| **Neighboring plates** | **Variant pairs** | **Misorientation angle $\omega$ (°)** | **Rotation axis** |
|---|---|---|---|
| A/B | $V_1$-$V_3$ | 82.6518 | 3.4° from the $<110>_{Tetr}$ direction |
| | $V_2$-$V_4$ | 13.6865 | 5.4° from the $<031>_{Tetr}$ direction |
| C/D | $V_5$-$V_7$ | 83.0965 | 3.7° from the $<110>_{Tetr}$ direction |
| | $V_6$-$V_8$ | 13.1146 | 4.6° from the $<301>_{Tetr}$ direction |
| B/C | $V_3$-$V_5$ | 83.1537 | 3.6° from the $<110>_{Tetr}$ direction |
| | $V_4$-$V_6$ | 14.4210 | 4.0° from the $<301>_{Tetr}$ direction |
| D/A | $V_7$-$V_1$ | 83.0093 | 3.7° from the $<110>_{Tetr}$ direction |
| | $V_8$-$V_2$ | 14.4189 | 3.1° from the $<301>_{Tetr}$ direction |

**Table 5.2.** Minimum rotation angle and rotation axis between two lamellar variants connected by an inter-plate interface in the high relative contrast zones.

| **Neighboring plates** | **Variant pairs** | **Misorientation angle $\omega$ (°)** | **Rotation axis** |
|---|---|---|---|
| 1/2 | $SV_1$-$SV_3$ | 82.9699 | 3.9° from the $<110>_{Tetr}$ direction |
| | $SV_2$-$SV_4$ | 14.1760 | 2.1° from the $<301>_{Tetr}$ direction |
| 3/4 | $SV_5$-$SV_7$ | 82.7963 | 3.4° from the $<110>_{Tetr}$ direction |
| | $SV_6$-$SV_8$ | 14.8473 | 3.6° from the $<031>_{Tetr}$ direction |
| 2/3 | $SV_3$-$SV_5$ | 82.5782 | 4.7° from the $<110>_{Tetr}$ direction |
| | $SV_4$-$SV_6$ | 12.2859 | 3.5° from the $<031>_{Tetr}$ direction |
| 4/1 | $SV_7$-$SV_1$ | 82.8110 | 5.0° from the $<110>_{Tetr}$ direction |
| | $SV_8$-$SV_2$ | 11.8090 | 9.9° from the $<031>_{Tetr}$ direction |

It should be noted that the present results on the orientation relationships between lamellar variants in two neighboring NM plates (e.g. plates A and B in the low relative contrast zones and plates 1 and 2 in the high relative contrast zones), the orientations of in-plate interlamellar interfaces and those of inter-plate interfaces with respect to the substrate are similar to those reported in literature [42-44, 82, 89]. However, our direct EBSD orientation measurements have clarified that plates C and D in the low relative contrast zones (or plates 3 and 4 in the high relative contrast zones) are not a repetition of plates A and B (or plates 1 and 2), in terms of the orientations of the lamellar variants, intra-plate interfaces and inter-plate interfaces.

### 5.3.2.3 Discussion

As demonstrated above, the morphology and the surface topology of the NM martensite plates in the low and high relative contrast zones are clearly different, although they appear to be composed of the same $(112)_{\mathrm{Tetr}}$ compound twins that act as the primary microstructural elements. In essence, the crystallographic orientations of the in-plate martensitic variants with respect to the substrate surface are not the same. This may be the origin of the morphological and topological differences observed for the two relative contrast zones, as discussed below.

**(1)** ***Low relative contrast zone***

Fig. 5.9(a) illustrates the atomic correspondences of eight lamellar variants organized in four NM plates (representing one variant group) for the low relative contrast zones ($Z_1$), viewed from the top of the as-deposited thin films. The atomic correspondences were constructed with the individually measured orientations of lamellar variants and the detemined intra- and inter-plate interface planes. The width ratio (expressed in the number ratio of atomic layers) between the minor and major variants is 0.492, being determined according to the phenomenological theory of martensitic transformation (known as WLR theory [103, 104]) under the assumption that the invariant plane is parallel to the MgO subtrate surface. This width ratio is very close to 2:4 (0.5), *i.e.* that of the ideal $(5\bar{2})$ stacking sequence. It should be noted that for the sake of saving article space, only two atomic layers for the minor variants and five atomic layers for the major variants were taken in Fig. 5.9(a) to illustrate the thickness ratio between the minor variants and the major variants, the structures of intra- and inter-plate interfaces and the orientations of lamellar variants with respect to the substrate.

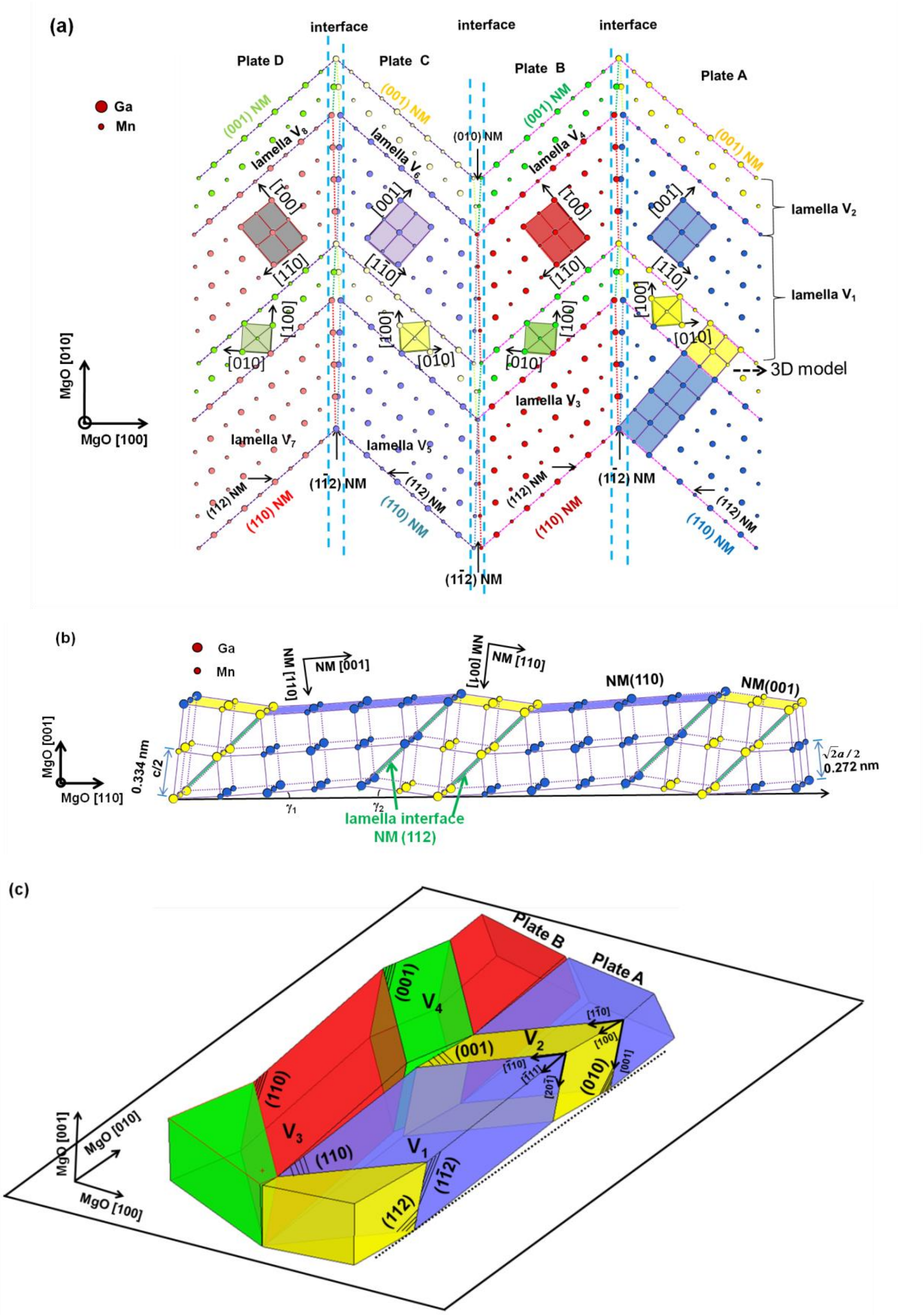

**Fig. 5.9**. (a) Atomic correspondences of eight lamellar variants in four NM plates for the low relative contrast zones (viewed from the top of as-deposited thin films). Only Mn and Ga atoms are displayed. (b) 3D-atomic correspondences of two alternately distributed lamellae with $(112)_{Tetr}$ compound twin relationship in one NM plate. The coherent twinning planes are outlined in green. $\gamma_1$ is the dihedral angle between the $(110)_{Tetr}$ plane of the major variants and the MgO substrate, and $\gamma_2$ is the dihedral angle between the $(001)_{Tetr}$ plane of the minor variants and the MgO substrate. (c) 3D configuration of two adjacent NM plates using in-plate lamellar variants as blocks to illustrate the plate interface misfits.

In reality, the lamellar variants are much thicker in nanometer range. One should not confuse this with the structure model from the "adaptive phase theory"[43, 44, 84, 89, 90], where the unit cell of the monoclinic 7M martensite is built based on a fixed number of atomic layers in each tetragonal variant. Fig. 5.9(b) presents a 3D display of the atomic correspondences between two alternately distributed lamellar variants with the $(112)_{\mathrm{Tetr}}$ compound twin relationship in one NM martensite plate. It is seen from Figs. 5.9(a) and 5.9(b) that the in-plate interlamellar interfaces are coherent with perfect atomic match.

To further reveal the inter-plate interface features, a 3D configuration of two adjacent NM plates was constructed using the twinned lamellar variants as blocks, as illustrated in Fig. 5.9(c). From Figs. 5.9(a) and 5.9(c), it is seen that the inter-plate interfaces are incoherent with certain amout of atomic mismatch. These inter-plate interfaces correspond to the so-called *a*-*c* twin interfaces, as mentioned in literature [44, 82]. Interestingly, the atoms from two adjacent NM plates are not totally disordered at the inter-plate interfaces but show some periodicity. For instance, each pair of major and minor lamellae constitutes one period, and two end atoms at one period possess perfect match at the inter-plate interface. If choosing those coherent atoms as reference, the atoms within one period experience an increased mismatch symmetrically to the plate interface when approching the interlamellar interface enclosed in the period. Both the periodic coherence and the symmetrical mismatch would define a straight inter-plate interface, which acts as another invariant plane for the NM martensite in the low relative contrast zones. Indeed, the width ratio required by this invariant plane is the same as that required by the invariant plane parallel to the MgO substrate surface. Due to such an atomic construction, inter-plate interface are always straight without need to bend to accommodate the unbalanced interfacial atomic misfits. This boundary character has been evidenced in the microstructural observation (Fig. 5.3(a)). As the combination of the lamellar variants ($(112)_{\mathrm{Tetr}}$ compound twins) are the same in neigboring plates, the atomic structures of all inter-plate interfaces are the same. Therefore, all plate interfaces in the low relative contrast zones are parallel to one another, as demonstrated in Fig. 5.3(b).

Moreover, as the major and the minor lamellar variants ($(112)_{\mathrm{Tetr}}$ compound twins) have the same orientation combination for all NM plates and they are distributed symmetrically to the inter-plate interfaces (Fig. 5.9(c)), there appear no microscopic height misfits across the inter-plate interfaces in the film normal direction. The NM plates in these zones are relatively flat without prononced surface relief or corrugation. Therefore, no significant relative contrast is visible between adjacent NM plates in the SE image.

### (2) *High relative contrast zone*

Similarly to the above analyzing scheme, the atomic correspondences of eight lamellar variants in four NM plates, the 3D-atomic correspondences of twinned lamellar variants in one NM plate, and the 3D configuration of two adjacent NM plates were also constructed for the high relative contrast zone ($Z_2$), as shown in Fig. 5.10. Note that each high relative contrast zone contains two distinct orientation plates (*e.g.* plates 1 and 2 or plates 3 and 4 in Fig. 5.10(a)) in terms of the orientations of paired lamellar variants (the $(112)_{\mathrm{Tetr}}$ compound twins). Due to the orientation differences, the width ratios between the minor and major variants in plate 1 and plate 2 are respectively 0.47 and 0.48, compared with that (0.492) for the low relative contrast zones. Here, the ideal width ratio 0.5 was used to construct Fig. 5.10. For a real material, the deviations from the ideal width ratio may be accommodated by stacking faults. From Fig. 5.10(a), it is seen that both major and minor lamellar variants in plate 1 are with their $(110)_{\mathrm{Tetr}}$ planes near-parallel to the substrate surface, whereas the major and minor lamellar variants in plate 2 are respectively with their $(001)_{\mathrm{Tetr}}$ and $(110)_{\mathrm{Tetr}}$ planes near-parallel to the substrate surface. If taking the coherent $(112)_{\mathrm{Tetr}}$ compound twin interfaces in plate 2 as reference, the $(112)_{\mathrm{Tetr}}$ compound twin interfaces in plate 1 can be generated by a rotation of about 90 °around the $[110]_{\mathrm{MgO}}$. In this manner, the $(112)_{\mathrm{Tetr}}$ compound twin interfaces become perpendicular to the substrate surface.

It is commonly considered that the $(112)_{\mathrm{Tetr}}$ compound twinning may bring about the atomic corrugations in NM plates, as illustrated in Fig. 5.10(b). As the direction of the atomic corrugations in plate 1 lie in the film plane, no significant surface relief is created on the free surface of thin films. Scanning tunneling microscopy (STM) imaging has evidenced that the free surface of the NM plates – being equivalent to plate 1 in the present work - stays smooth [43].

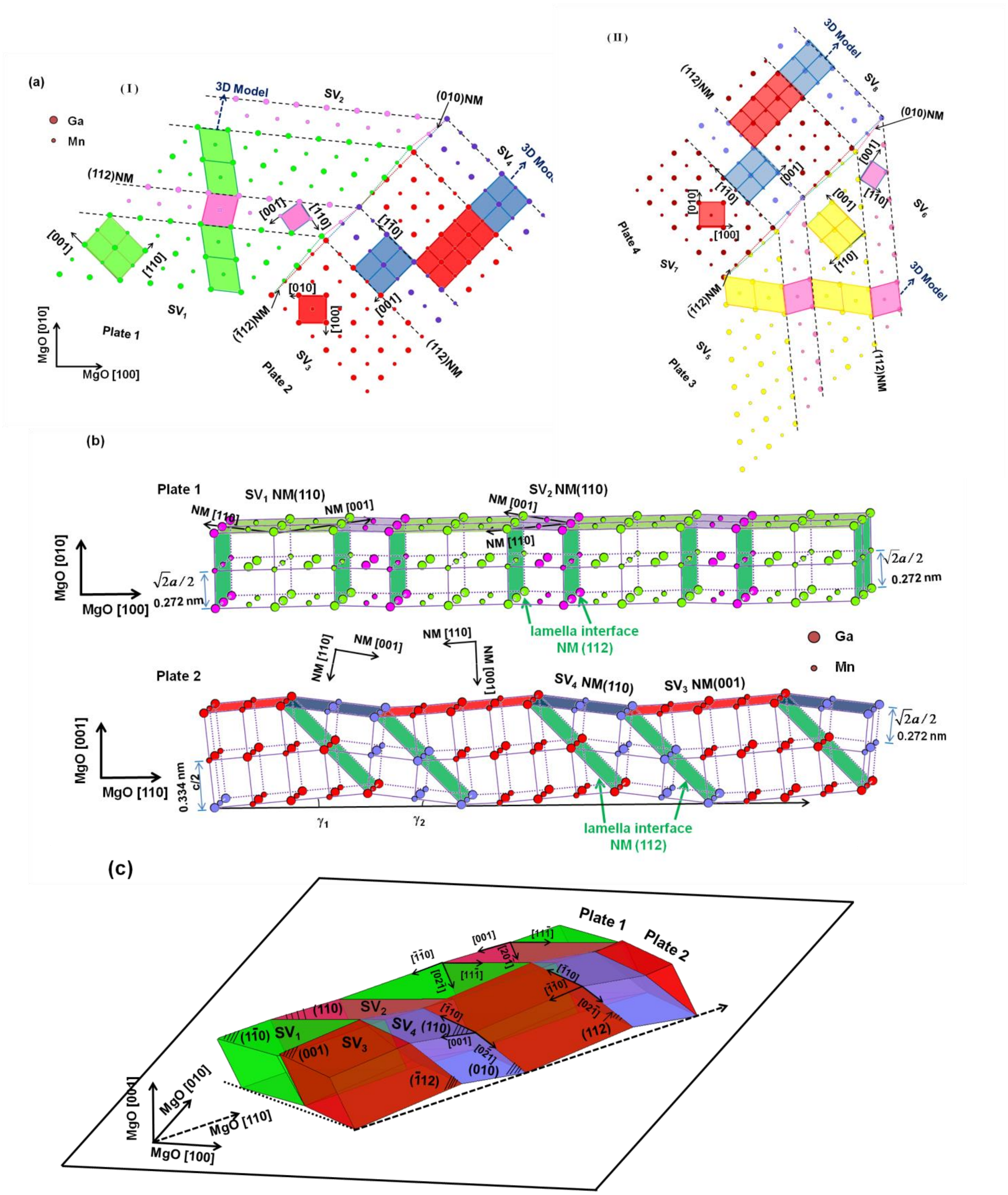

**Fig. 5.10.** (a) Atomic correspondences of eight lamellar variants in four NM plates for high relative contrast zones (viewed from the top of as-deposited thin films). Only Mn and Ga atoms are displayed. (b) 3D-atomic illustration of the combination of two lamellar variants ($(112)_{Tetr}$ compound twins) in plates 1 and 2. The twinning planes between lamellar variants are colored in green. $\gamma_1$ is the dihedral angle between $(001)_{Tetr}$ plane of the major variants and the MgO substrate, and $\gamma_2$ is the dihedral angle between the $(110)_{Tetr}$ plane of the minor variants and the MgO substrate. (c) 3D construction of two adjacent plates showing the plate interface misfits.

From Figs. 5.10(a) and 5.10(c), it is seen that the microscopic plate interface outlined by the paired $(\bar{1}12)_{\mathrm{Tetr}}$ and $(010)_{\mathrm{Tetr}}$ planes from the neighboring plates are not in mirror relation with respect to the inter-plate interface. As the lengths of one pair of major and minor variants (considered as one period) in two plates are not the same along the macroscopic plate interface (Fig. 5.10(c)), unbalanced atomic misfit can be expected. This misfit is accumulative and increases with the increased length (parallel to the film surface) and the height (normal to the film surface) of the plates. Therefore, the plate interface orientation could be dominated by the orientation of the $(\bar{1}12)_{\mathrm{Tetr}}$ of the major variant in either plate 1 or plate 2, depending on local constraints. This may be the reason why the inter-plate interfaces in the high relative contrast zones are bent after running in certain length.

As displayed in Figs. 5.10(b) and 5.10(c), the atomic misfit also arises in the film normal direction. For example, the planar spacing of the major and minor variants in the film normal direction is 0.272 nm in plate 1, but 0.334 (major) and 0.272 nm (minor) in plate 2. If assuming that the major variants in plate 2 make dominant contribution to the atomic misfit between the two plates at the plate interface, the region of plate 2 is elevated by 23% in height with respect to that of plate 1. In the present work, the as-deposited thin films were subject to electrolytic polishing before microstructural observation. The constraints induced by the atomic misfits in the height direction may be fully released at the free surface. Thus, significant height difference between plate 1 and plate 2 can be expected. In the high relative contrast zones of Fig. 5.3(a), the plates with higher brightness are those with larger planar spacing in the film normal direction (major variants in plate 2), whereas the plates with lower brightness are those with smaller planar spacing in the film normal direction. This could well account for the distinct levels of brightness between neighboring plates observed in the high relative contrast zones.

### 5.3.3 Crystallographic features of 7M martensite

Fig. 5.11 presents a selected SE image of 7M martensite plates with full-featured microstructural constituents. It is evident that in Fig. 5.11(a) the individual martensite plates are clustered into groups, exhibiting either low relative contrast (Group 1) or high relative SE contrast (Group 2 and Group 3), as the case of NM martensite. The low relative contrast zones contain long straight plates parallel to one of the substrate edges, whereas the high relative contrast zones contain shorter and bent plates oriented at specific angles (roughly 45°) with respect to the substrate edges. Detailed inspection on the high relative contrast zones has shown that the traces of inter-plate interfaces have three distinct spatial orientations, as indicated by the dotted yellow and green lines and the solid black lines in Fig. 5.11(b). The angle between the dotted yellow and green lines is about 15°, being bisected by one solid black line that is parallel to the $[\bar{1}\ 1\ 0]_{MgO}$ direction. The observed microstructural features are similar to those reported in recent studies [42-44, 82, 86]. A low relative contrast zone (Group 1) corresponds to the so-called Type Y pattern, and a high relative contrast zone (Group 2 or Group 3) to the Type X pattern [91]. In most cases, the neighboring plates in both the low and high relative contrast zones have almost the same width.

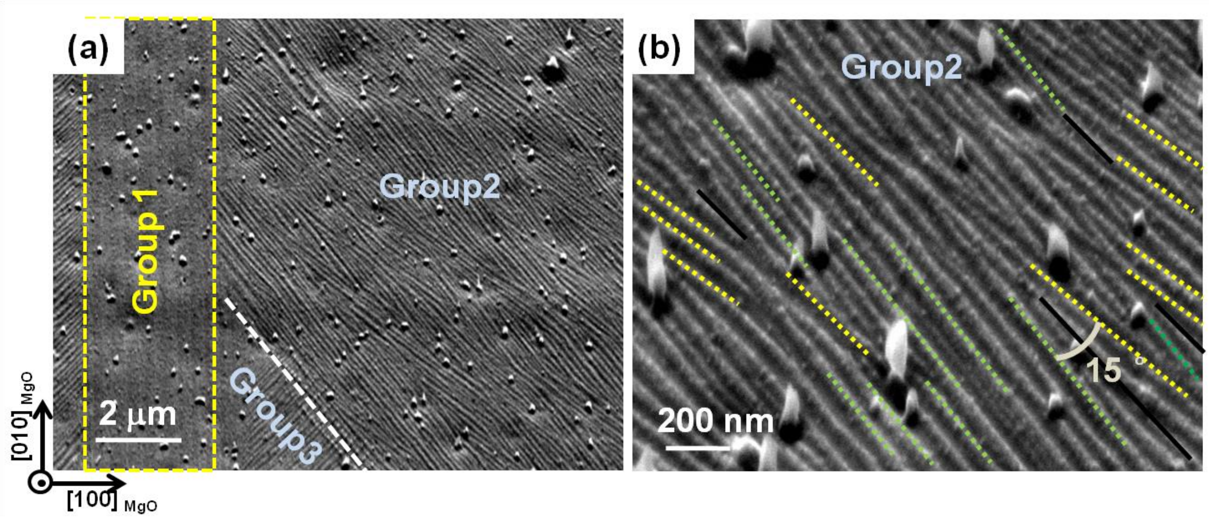

**Fig. 5.11.** (a) SE image of plate groups of 7M martensite with low relative contrast (Group 1) and high relative contrast (Group 2 and Group 3). (b) Magnified image of individual plates belonging to Group 2. Note that the traces of inter-plate interfaces have three distinct spatial orientations, as highlighted by the dotted yellow lines (Type-II twin interfaces), the dotted green lines (Type-II twin interfaces), and the solid black lines (Type-I twin interfaces).

The microstructural-correlated characterizations of crystallographic orientations of 7M martensite plates were conducted by EBSD, where the macroscopic reference frame was set to the crystal basis of the MgO monocrystal substrate. It is found that each 7M martensite plate is specified by a single crystallographic orientation, being designated as one orientation variant. There are a total of four different orientation variants distributed in one plate group, as illustrated in Fig. 5.12(a) and Fig. 5.12(b). Here, the four orientation variants - representing one plate group with low or high relative contrast - are denoted by the symbols 7M-$V_1$, $V_2$, $V_3$, $V_4$ (Fig. 5.12(a)) and 7M-$V_A$, $V_B$, $V_C$, $V_D$ (Fig. 5.12(b)), respectively.

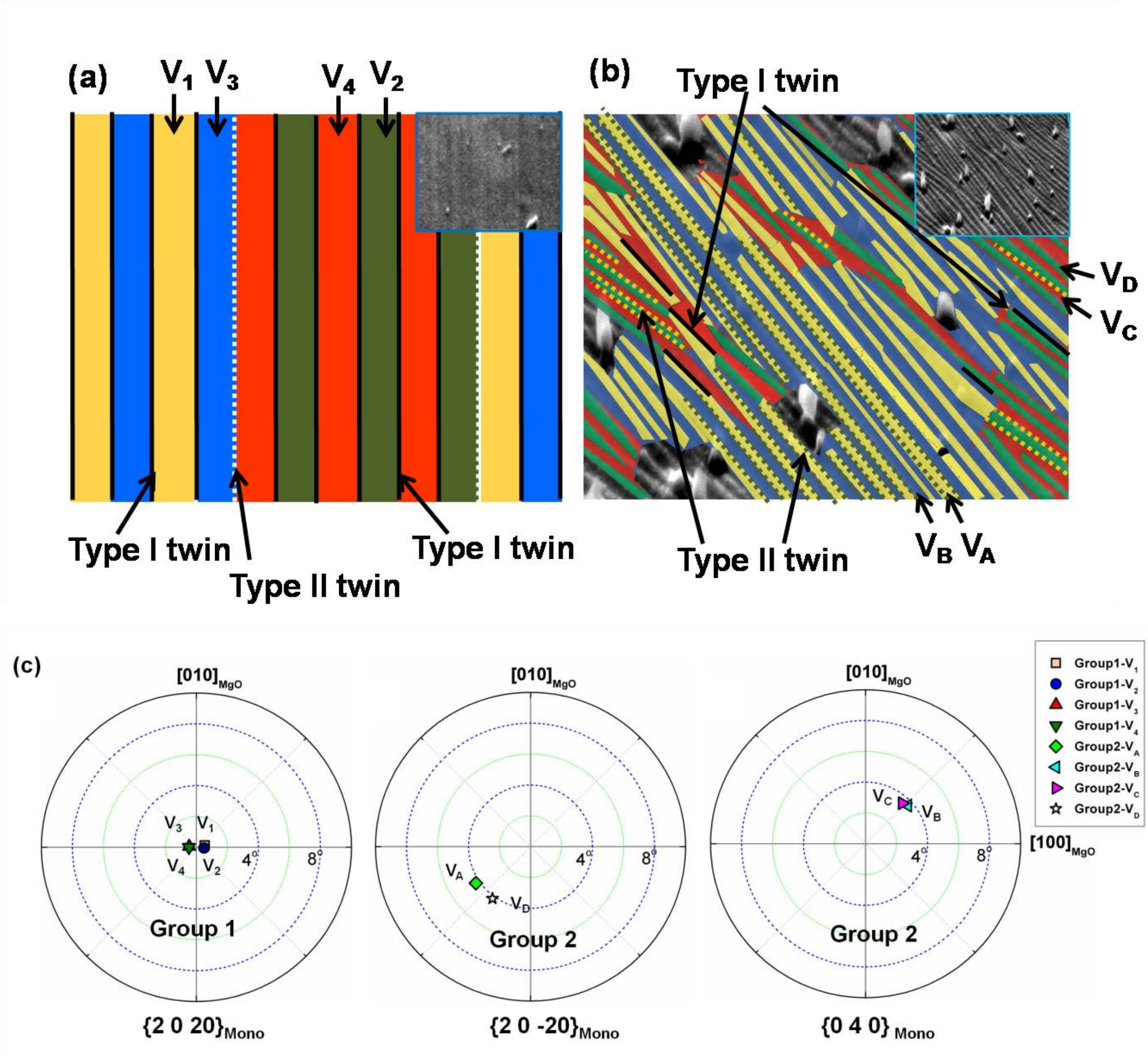

**Fig. 5.12.** (a and b) Illustration of 7M martensite plates with four orientation variants in Group 1 (denoted by $V_1$, $V_2$, $V_3$, $V_4$) and Group 2 (denoted by $V_A$, $V_B$, $V_C$, $V_D$). The insets show the corresponding microstructures in the same zones. (c) Representation of individually measured orientations of 7M variants in Group 1 and Group 2 in the form of $\{2\ 0\ 20\}_{mono}$, $\{2\ 0\ \overline{20}\}_{mono}$ and $\{0\ 4\ 0\}_{mono}$ pole figures.

Fig. 5.12(c) presents the individually measured orientations of the 7M variants in Group 1 and Group 2 in the form of $\{2\ 0\ 20\}_{mono}$, $\{2\ 0\ \overline{20}\}_{mono}$ and $\{0\ 4\ 0\}_{mono}$ pole figures. The subscript “mono” stands for monoclinic, as the three indices of the crystallographic planes are defined in the monoclinic Bravais lattice frame. Clearly, in the low relative contrast zone

(Group 1), the four variants 7M-$V_1$, $V_2$, $V_3$, $V_4$ are all with their $(2\ 0\ 20)_{mono}$ plane nearly parallel to the substrate surface (Fig. 5.12(c), left). These variants correspond to the ***a*-*c*** twins with their common ***b*** axis perpendicular to the substrate surface, the so-called ***b***-variants in the literature [42, 44, 82]. However, in the high relative contrast zone (Group 2), the variants $V_A$ and $V_D$ (colored in yellow and green in Fig. 5.12(b)) are with their $(2\ 0\ \overline{20})_{mono}$ plane nearly parallel to the substrate surface (Fig. 5.12(c), middle), and the variants $V_B$ and $V_C$ (colored in blue and red in Fig. 5.12(b)) with their $(0\ 4\ 0)_{mono}$ plane nearly parallel to the substrate surface (Fig. 5.12(c), left). Furthermore, the variants $V_B$ and $V_C$ and the variants $V_A$ and $V_D$ are of low brightness and high brightness, respectively. They correspond to the ***a*-*c*** twins with their common ***b*** axis parallel to the substrate surface, the so-called ***a***-variants for $V_A$ and $V_D$ and ***c***-variants for $V_B$ and $V_C$ [44].

It should be noted that in the high relative contrast zones, one plate group is composed of two $(2\ 0\ \overline{20})_{mono}$ variants ($V_A$ and $V_D$) and two $(0\ 4\ 0)_{mono}$ variants ($V_B$ and $V_C$). But in the literature [42, 44, 82], a pair of the $(2\ 0\ \overline{20})_{mono}$ variants ($V_A$ and $V_D$) was designated to be one single ***a***-variant and a pair of the $(0\ 4\ 0)_{mono}$ variants ($V_B$ and $V_C$) to one single ***c***-variant. The same situation has also happened to the identification of constituent variants in the low relative contrast zones, *e.g.* a pair of the $(2\ 0\ 20)_{mono}$ variants ($V_1$ and $V_4$, or $V_2$ and $V_3$) was previously taken as one single ***b***-variant. The appearance of such a discrepancy in specifying the number of variants in one plate group arises from the fact that in the other work, the crystallographic orientations of constituent variants in thin films were determined by conventional X-ray diffraction (XRD). The limited spatial resolution with this technique has prevented differentiating the corresponding $(2\ 0\ 20)_{mono}$, $(2\ 0\ \overline{20})_{mono}$, and $(0\ 4\ 0)_{mono}$ planes from variant pairs in pole figures. Here, the $(2\ 0\ 20)_{mono}$, $(2\ 0\ \overline{20})_{mono}$ and $(0\ 4\ 0)_{mono}$ planes refer to the $(0\ 4\ 0)_{orth}$, $(4\ 0\ 0)_{orth}$ and $(0\ 0\ 4)_{orth}$ planes in the pseudo-orthorhombic coordinate system, respectively [42, 89]). In consequence, only two variants were found in each plate group [44, 82], instead of four variants as evidenced in the present work.

**Table 5.3.** Calculated misorientations between adjacent 7M variants in Group 1, expressed as rotation axis (***d***) and angle ($\omega$) in the orthonormal crystal reference frame. The Euler angles of four variants $V_1$, $V_2$, $V_3$, and $V_4$ are respectively (137.94°, 46.93°, 90.45°), (221.82°, 133.15°, 270.46°), (41.68°,133.18°, 270.44°), and (318.32°, 46.80°, 90.50°).

| **Variant pairs** | **Misorientation angle ($\omega$)** | **Rotation axis *d*** | | | Twin type |
|---|---|---|---|---|---|
| | | $d_1$ | $d_2$ | $d_3$ | |
| $V_1$:$V_3$ | 83.1337 | -0.7342 | -0.0010 | -0.6789 | Type I |
| | 179.9229 | 0.4504 | 0.7482 | -0.4871 | |
| $V_2$:$V_4$ | 82.8455 | -0.7339 | -0.0007 | -0.6791 | Type I |
| | 179.9432 | 0.4493 | 0.7498 | -0.4856 | |
| $V_1$:$V_2$ | 96.7436 | 0.7265 | -0.0005 | 0.6871 | Type II |
| | 179.9519 | -0.5136 | 0.6643 | 0.5430 | |
| $V_3$:$V_4$ | 97.2851 | 0.7254 | 0.0002 | 0.6882 | Type II |
| | 179.9806 | 0.5166 | -0.6607 | -0.5445 | |
| $V_1$:$V_4$ | 179.3063 | 0.6837 | 0.0036 | -0.7297 | Compound |
| | 179.5858 | -0.7297 | -0.0060 | -0.6837 | |
| $V_2$:$V_3$ | 179.3435 | 0.6841 | -0.0011 | -0.7293 | Compound |
| | 179.8736 | 0.7293 | 0.0057 | 0.6841 | |

**Table 5.4.** Calculated misorientations between adjacent 7M variants in Group 2, expressed as rotation axis (***d***) and angle ($\omega$) in the orthonormal crystal reference frame. The Euler angles of four variants $V_A$, $V_B$, $V_C$, and $V_D$ are respectively (48.43°, 136.75°, 95.28°), (178.19°, 92.35°, 2.78°), (271.81°, 87.65°, 182.78°), and (41.57°, 43.25°, 275.28°).

| **Variant pairs** | **Misorientation angle ($\omega$)** | **Rotation axis *d*** | | | **Twin type** |
|---|---|---|---|---|---|
| | | $d_1$ | $d_2$ | $d_3$ | |
| $V_A$:$V_C$ | 82.3098 | -0.7414 | 0.0195 | -0.6707 | Type I |
| | 178.5255 | -0.4414 | -0.7529 | 0.4880 | |
| $V_B$:$V_D$ | 82.2390 | -0.7476 | -0.0277 | -0.6635 | Type I |
| | 177.9083 | 0.4364 | 0.7534 | -0.4917 | |
| $V_A$:$V_B$ | 97.8691 | 0.7295 | 0.0049 | 0.6839 | Type II |
| | 179.5722 | -0.5156 | -0.6569 | 0.5500 | |
| $V_C$:$V_D$ | 97.6586 | 0.7246 | -0.0032 | 0.6891 | Type II |
| | 179.7170 | 0.5187 | 0.6583 | -0.5454 | |
| $V_A$:$V_D$ | 177.3972 | 0.6871 | -0.0004 | -0.7265 | Compound |
| | 179.9432 | 0.7263 | 0.0227 | 0.6869 | |
| $V_B$:$V_C$ | 179.6341 | 0.6693 | -0.0013 | -0.7429 | Compound |
| | 179.8470 | 0.7429 | 0.0031 | 0.6693 | |

With the correctly determined crystallographic orientations (represented with three Euler angles in Bunge’s notation [92]) of the four 7M variants in each plate group, the orientation relationships between neighboring variants can be further calculated. Table 5.3 and Table 5.4

show the calculated misorientations of adjacent variants in the low and high relative contrast zones, expressed in terms of rotation axis and angle. Detailed analysis has revealed that each pair of adjacent variants can be identified as either Type-I or Type-II or Compound twins, depending on whether the rotation axis is close to the normal of a rational plane or/and a rational direction in the monoclinic crystal basis. It is seen from Table 1 that in the low relative contrast zone (Group 1), the variant pairs $V_1$:$V_3$ and $V_2$:$V_4$ belong to Type-I twins, $V_1$:$V_2$ and $V_3$:$V_4$ to Type II twins, and $V_1$:$V_4$ and $V_2$:$V_3$ to Compound twins. The adjacent variants in the high relative contrast zone (Group 2) possess exactly the same twin relationships as shown in Table 2, where $V_A$:$V_C$ and $V_B$:$V_D$ belong to Type I twins, $V_A$:$V_B$ and $V_C$:$V_D$ to Type II twins, and $V_A$:$V_D$ and $V_B$:$V_C$ to Compound twins.

**Table 5.5.** Twinning elements of 7M variants represented in the monoclinic crystal coordinate frame. $\boldsymbol{K}_1$ is the twinning plane, $\boldsymbol{K}_2$ the reciprocal or conjugate twinning plane, $\boldsymbol{\eta}_1$ the twinning direction, $\boldsymbol{\eta}_2$ the conjugate twinning direction, ***P*** the shear plane, and *s* the magnitude of shear.

| Twin elements | Type I twin ($V_A$:$V_C$, $V_B$:$V_D$; $V_1$:$V_3$, $V_2$:$V_4$) | Type II twin ($V_A$:$V_B$, $V_C$:$V_D$; $V_1$:$V_2$, $V_3$:$V_4$) | Compound twin ($V_A$:$V_D$, $V_B$:$V_C$; $V_1$:$V_4$, $V_2$:$V_3$) |
|---|---|---|---|
| $\boldsymbol{K}_1$ | $(1\ \bar{2}\ \overline{10})_{\mathrm{mono}}$ | $(1.1240\ \bar{2}\ \overline{8.7602})_{\mathrm{mono}}$ | $(1\ 0\ 10)_{\mathrm{mono}}$ |
| $\boldsymbol{K}_2$ | $(\overline{1.1240}\ \bar{2}\ 8.7602)_{\mathrm{mono}}$ | $(\bar{1}\ \bar{2}\ 10)_{\mathrm{mono}}$ | $(\bar{1}\ 0\ 10)_{\mathrm{mono}}$ |
| $\eta_1$ | $[11.0973\ 10\ \overline{0.8903}]_{\mathrm{mono}}$ | $[\overline{10}\ \overline{10}\ 1]_{\mathrm{mono}}$ | $[\overline{10}\ 0\ 1]_{\mathrm{mono}}$ |
| $\eta_2$ | $[10\ \overline{10}\ \bar{1}]_{\mathrm{mono}}$ | $[11.0973\ \overline{10}\ \overline{0.8903}]_{\mathrm{mono}}$ | $[10\ 0\ 1]_{\mathrm{mono}}$ |
| ***P*** | $(1\ \overline{0.1161}\ 11.1610)_{\mathrm{mono}}$ | $(1\ 0.1161\ 11.1610)_{\mathrm{mono}}$ | $(0\ 1\ 0)_{\mathrm{mono}}$ |
| *s* | 0.2537 | 0.2537 | 0.0295 |

From the calculated misorientation data, the complete twinning elements - $\boldsymbol{K}_1$, $\boldsymbol{K}_2$, $\boldsymbol{\eta}_1$, $\boldsymbol{\eta}_2$, ***P*** and *s* - of the above three types of twins were derived using a general method developed by our group [74, 95], as shown in Table 5.5. The twinning modes are exactly the same as those in bulk materials [73, 74]. Here, an attempt is made to correlate the present twin relationships (identified by EBSD) under the monoclinic crystal system with the published ones (deduced from XRD) under the pseudo-orthorhombic crystal system. It is seen from Table 5.6 that the so-called ***a-c*** twins with the $(1\ 0\ 1)_A$ as the twin interface are the Type-I twins in the present work. Interestingly, the Type-II twins in the present work also belong to the so-called ***a-c*** twins.

Clearly the specification of twin relationships under the pseudo-orthorhombic crystal system has difficulty to distinguish the subtle differences between the two types of twins. Apart from this, the compound twins could not be differentiated due to the simplification of the 7M martensite with a pseudo-orthorhombic crystal structure.

**Table 5.6.** Comparison of twin orientation relationships identified in the present work with those reported in the literature.

| 14M-adaptive [44, 82, 91] | 7M modulated super cell | 7M-average unit cell | Notes |
|---|---|---|---|
| $a_{14M}$-$c_{14M}$ twin<br>$K_1 = (1\ 0\ 1)_{14M}$ | Type I twin<br>$K_1 = (1\ \bar{2}\ \overline{10})_{mono}$ | Type I twin<br>$K_1 = (1\ \bar{2}\ \bar{1})_{mono}$ | $K_1^{14M}\ //\ K_1^{mono}\ //\ \{101\}_A$ |
| $a_{14M}$-$c_{14M}$ twin<br>$K_1$ close to $(1\ 0\ 1)_{14M}$<br>*Twinning elements undetermined* | Type II twin<br>$K_1 = (1.1240\ \bar{2}\ \overline{8.7602})_{mono}$<br>$\eta_1 = [\overline{10}\ \overline{10}\ 1]_{mono}$ | Type II twin<br>$K_1 = (1.1240\ \bar{2}\ \overline{0.8760})_{mono}$<br>$\eta_1 = [\bar{1}\ \bar{1}\ 1]_{mono}$ | - |
| *Twin type existing but undetermined* | Compound twin<br>$K_1 = (1\ 0\ 10)_{mono}$ | Compound twin<br>$K_1 = (1\ 0\ 1)_{mono}$ | - |

To have a general view on the configuration of the 7M variants, the occurrences of the three types of twins in the two relative contrast zones are further examined. In the low relative contrast zone (Fig. 5.12(a)), the Type-I twins ($V_1$:$V_3$ and $V_2$:$V_4$) and the Type-II twins ($V_1$:$V_2$ and $V_3$:$V_4$) are those with the interface traces marked by solid black lines and dotted white lines, respectively. In these zones, the traces of Type-I and Type-II interfaces are in parallel, and the majority of variants are Type-I twins. Moreover, no compound twin relationship ($V_1$:$V_4$ and $V_2$:$V_3$) can be observed between two adjacent variants. However, in the high relative contrast zone (Fig. 5.12(b)), the majority of variants are Type-II twins. The interface traces of Type-I twins have only one orientation (marked by the solid black lines), whereas those of Type-II twins have two orientations (marked by the dotted yellow and green lines). The interfaces with compound twin relationship ($V_A$:$V_D$ and $V_B$:$V_C$) are those intra-plate interfaces, occurred with the bending of martensite plates.

Using the indirect two-trace method [102, 105], the planes of twin interfaces in the low and high relative contrast zones were calculated with the measured crystallographic orientations of individual variants and orientations of their interface traces on the film surface.

Results show that the twin interface planes are coincident with the respective twinning planes, *i.e.* $\{1\ \bar{2}\ \overline{10}\}_{mono}$ for Type-I twins, $\{1.1240\ \bar{2}\ \overline{8.7602}\}_{mono}$ for Type-II twins and $\{1\ 0\ 10\}_{mono}$ for Compound twins, as in the case for bulk materials. For easy visualization of the through-film-thickness orientations of twin interfaces in two relative contrast zones, the $\{1\ \bar{2}\ \overline{10}\}_{mono}$, $\{1.1240\ \bar{2}\ \overline{8.7602}\}_{mono}$ and $\{1\ 0\ 10\}_{mono}$ planes of four variants in Group 1 and Group 2 are represented in the form of stereographic projections, as displayed in Fig. 5.13(a) and Fig. 5.13(b). In both figures, the interface traces on the film surface are indicated by arrowed lines.

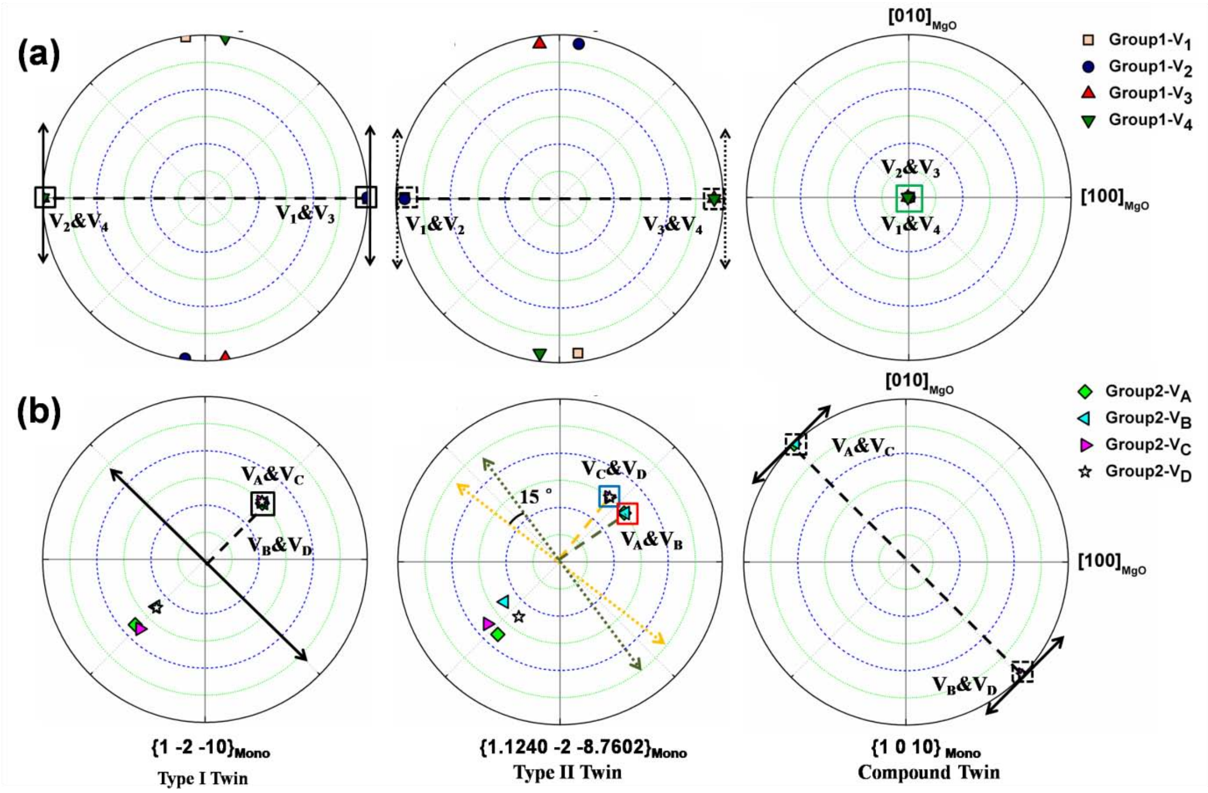

**Fig. 5.13.** Stereographic projections of twin interface planes between adjacent 7M variants in (a) low relative contrast zone (Group 1) and (b) high relative contrast zone (Group 2). The macroscopic sample coordinate frame is set to the crystal basis of the MgO substrate. The lines with arrows represent the trace of twin interfaces.

For the low relative contrast zone (Group 1), it is seen from the $\{1\ \bar{2}\ \overline{10}\}_{mono}$ pole figure (Fig. 5.13(a), left) that there are two different Type-I twin interfaces, being oriented at +89.9 ° ($V_1$ and $V_3$) and -89.9 ° ($V_2$ and $V_4$) with respect to the substrate surface, although their interface traces on the film surface are both in parallel to the $[0\ 1\ 0]_{\mathrm{MgO}}$ direction. Similar cases can be found for the Type-II twin interfaces. As shown in the $\{1.1240\ \bar{2}\ \overline{8.7602}\}_{\mathrm{mono}}$ pole figure (Fig. 5.13(a), middle), the two Type-II twin interfaces that have parallel traces on the film surface intersect the substrate surface at +85 ° ($V_3$ and $V_4$) and -85 ° ($V_1$ and $V_2$), respectively. Apparently, the four Type-I and Type-II twin interfaces are oriented differently through the film thickness, but they have the same interface trace orientation on the film surface. As for the Compound twin interfaces, the interfaces between adjacent variants are all parallel to the film surface, as shown in the $\{1\,0\ 1\ 0\}_{\mathrm{mono}}$ pole figure (Fig. 5.13(a), right). That is why no Compound twin interfaces could be observed by examining solely the film surface microstructure in the present work. Such Compound twin interfaces have been detected by cross section SEM observation [44].

For the high relative contrast zone (Group 2), it is seen from the $\{1\ \bar{2}\ \overline{10}\}_{\mathrm{mono}}$ pole figure (Fig. 5.13(b), left) that the Type-I twin interfaces between variants $V_A$ and $V_C$ and those between variants $V_B$ and $V_D$ possess roughly the same orientation in the film. They incline at about 45 ° to the substrate surface and their traces on the film surface are along the $[\bar{1}\,1\,0]_{\mathrm{MgO}}$ direction. However, for the Type-II twin interfaces as shown in the $\{1.1240\,\bar{2}\ \overline{8.7602}\}_{\mathrm{mono}}$ pole figure (Fig. 5.13(b), middle), although the interface between $V_A$ and $V_B$ and that between $V_C$ and $V_D$ are inclined at about 45 ° to the substrate surface, their interface traces on the film surface do not possess the same orientation. One is 37.3 ° ($V_A$ and $V_B$) away from the $[1\,0\,0]_{\mathrm{MgO}}$ direction and the other 52.5 ° away from the $[1\,0\,0]_{\mathrm{MgO}}$ direction. Therefore, the angle between two differently oriented Type-II twin interface traces on the film surface is 15 ° (as shown in Fig. 5.11(b)), being in accordance with the results reported in the literature [91]. As for the Compound twin interfaces, the interface between $V_A$ and $V_D$ and that between variant $V_B$ and $V_C$ possess roughly the same orientation (Fig. 5.13(b), right). They are nearly perpendicular to the substrate surface and their traces on the film surface are nearly parallel to the $[1\,1\,0]_{\mathrm{MgO}}$ direction. It is found that the bending of martensite plates in the high relative contrast zone is associated with the orientation change from $V_A$ to $V_D$ or from $V_B$ to $V_C$, which results in an change of the plate interface from type I twin interface to type II twin interface or from type II twin interface to type I twin interface.

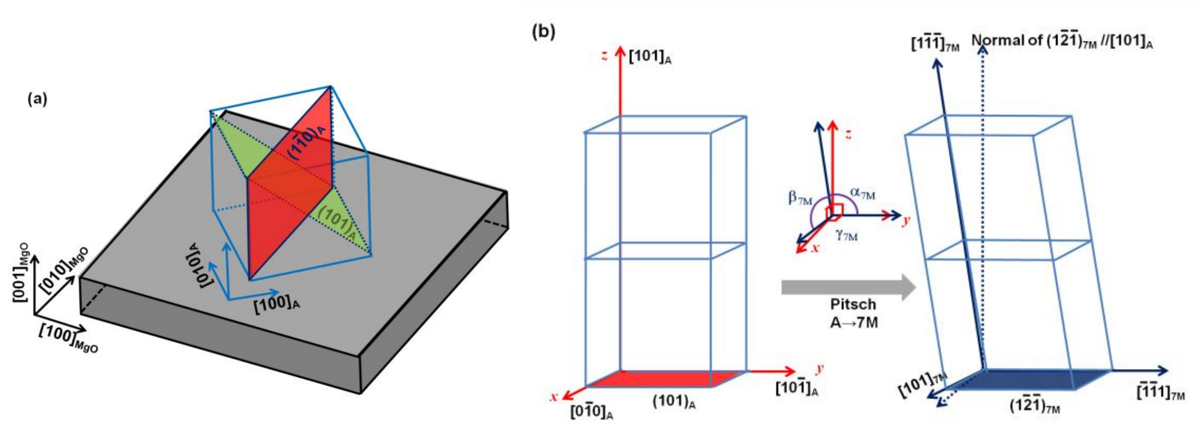

**Fig. 5.14.** (a) Illustration of the orientation relationship between NiMnGa austenite and MgO substrate. (b) Schematic of the Pitsch orientation relationship between the cubic austenite lattice and the monoclinic 7M martensite lattice. Note that only the average monoclinic unit cell [73] is used for describing the 7M structure.

Since the epitaxial NiMnGa thin films were prepared on the MgO monocrystal substrate at elevated temperature, the thin films were composed of monocrystalline austenite when the deposition process was finished. According to the scanning tunneling microscopy (STM) analysis [43], the orientation relationship between the MgO substrate and the NiMnGa austenite refers to $(0\,0\,1)_{\mathrm{MgO}}[1\,1\,0]_{\mathrm{MgO}}\,//\,(0\,0\,1)_{\mathrm{A}}[1\,0\,0]_{\mathrm{A}}$, as illustrated in Fig. 5.14(a). Upon cooling, the cubic austenite transforms to the monoclinic 7M modulated martensite below the martensitic transformation start temperature. Due to the displacive nature of martensitic transformation, the phase transformation from austenite to 7M martensite in the present thin films is realized by coordinated lattice deformation of the parent phase following certain orientation relationship between the two phases. The Pitsch orientation relationship ($(1\ 1\ 0)_{\mathrm{A}}[1\ \bar{1}\ 0]_{\mathrm{A}}\,//\,(1\ \bar{2}\ \bar{1})_{\mathrm{mono}}[\bar{1}\ \bar{1}\ 1]_{\mathrm{mono}}$), previously revealed for the austenite to 7M martensite transformation in bulk NiMnGa [73], is further confirmed in the present work, as illustrated in Fig. 5.14(b).

It has been demonstrated that the austenite to 7M martensite transformation should be self-accommodated to minimize the macroscopic strain by forming specific variant pairs or groups with specific variant volume fractions [106-108]. This self-accommodation character in accordance with the substrate constraint may be the origin of the characteristic organizations of 7M variants in different variant zones, notably the low and high relative contrast zones in the present work. With the aid of the Pitsch orientation relationship, the lattice deformation during the martensitic transformation can be described by the displacement gradient tensor (*M*) in the orthonormal basis referenced to the $[0\,\bar{1}\,0]_{\mathrm{A}}$ - $[1\,0\,\bar{1}]_{\mathrm{A}}$ - $[1\,0\,1]_{\mathrm{A}}$, *i.e.*

$$M = \left\{\begin{matrix} e_{xx} & e_{xy} & e_{xz} \\ e_{yx} & e_{yy} & e_{yz} \\ e_{zx} & e_{zy} & e_{zz} \end{matrix}\right\} = \left\{\begin{matrix} 0.0024 & 0 & 0.0098 \\ -0.0111 & 0.0080 & -0.1265 \\ 0 & 0 & 0 \end{matrix}\right\} \qquad (5\text{-}1)$$

where the diagonal term $e_{ii}$ represents the dilatation in the $i$ direction ($[0\,\bar{1}\,0]_{\mathrm{A}}$, or $[1\,0\,\bar{1}]_{\mathrm{A}}$ or $[1\,0\,1]_{\mathrm{A}}$), and the off diagonal term $e_{ij}$ represents the shear in the $i$ direction on the plane normal and in the $j$ direction. It is seen that the largest deformation during the transformation happens as a shear in the $\{1\,0\,1\}_{\mathrm{A}}$ plane along the $<1\,0\,\bar{1}>_{\mathrm{A}}$ direction, *i.e.* the twinning plane and the twinning direction of the 7M martensite. Here, for simplicity, we ignore the structural modulation of the 7M martensite and the 7M superstructure is reduced to an average monoclinic unit cell that corresponds to one cubic unit cell [73].

Due to the cubic crystal symmetry of the austenite phase, there are six distinct but equivalent $\{1\,1\,0\}_{\mathrm{A}}$ planes, *i.e.* $(1\,0\,1)_{\mathrm{A}}$, $(1\,0\,\bar{1})_{\mathrm{A}}$, $(0\,1\,1)_{\mathrm{A}}$, $(0\,1\,\bar{1})_{\mathrm{A}}$, $(1\,1\,0)_{\mathrm{A}}$ and $(1\,\bar{1}\,0)_{\mathrm{A}}$. Orientation calculation has confirmed that the four 7M variants in Group 1 in the low relative contrast zone are originated from the $(1\,\bar{1}\,0)_{\mathrm{A}}$ plane, whereas the four 7M variants in Group 2 in the high relative contrast zone are from the $(1\,0\,1)_{\mathrm{A}}$ plane. It is seen from Fig. 5.14(a) that the $(1\,\bar{1}\,0)_{\mathrm{A}}$ plane is perpendicular to the MgO substrate surface and parallel to the $[0\,1\,0]_{\mathrm{MgO}}$ direction, whereas the $(1\,0\,1)_{\mathrm{A}}$ plane is inclined at $45^{\circ}$ with respect to the MgO substrate surface and parallel to the $[1\,1\,0]_{\mathrm{MgO}}$ direction. Clearly, the 7M variants that originate from the two austenite planes ($(1\,\bar{1}\,0)_{\mathrm{A}}$ and $(1\,0\,1)_{\mathrm{A}}$) should be subject to different constraints from the MgO substrate. To quantify these differences and their influence on the occurrences of different variant pairs in different martensite groups, the displacement gradient tensor of each variant is calculated and presented in the macroscopic reference frame ($[1\,0\,0]_{\mathrm{MgO}}$-$[0\,1\,0]_{\mathrm{MgO}}$-$[0\,0\,1]_{\mathrm{MgO}}$).

For the low relative contrast zone (Group 1), the displacement gradient tensors of the four 7M variants ($V_1$, $V_2$, $V_3$, $V_4$) in the macroscopic reference frame are expressed as

$$\begin{array}{cccc}
\mathbf{V_1} & \mathbf{V_2} & \mathbf{V_3} & \mathbf{V_4} \\
M_1=\left\{\begin{matrix} 0 & 0 & 0 \\ \mathbf{0.1265} & 0.0080 & -0.0111 \\ -0.0098 & 0 & 0.0024 \end{matrix}\right]_{\mathrm{MgO}} &
M_2=\left\{\begin{matrix} 0 & 0 & 0 \\ \mathbf{-0.1265} & 0.0080 & 0.0111 \\ -0.0098 & 0 & 0.0024 \end{matrix}\right]_{\mathrm{MgO}} &
M_3=\left\{\begin{matrix} 0 & 0 & 0 \\ \mathbf{-0.1265} & 0.0080 & -0.0111 \\ 0.0098 & 0 & 0.0024 \end{matrix}\right]_{\mathrm{MgO}} &
M_4=\left\{\begin{matrix} 0 & 0 & 0 \\ \mathbf{0.1265} & 0.0080 & 0.0111 \\ 0.0098 & 0 & 0.0024 \end{matrix}\right]_{\mathrm{MgO}}
\end{array}$$

$$\underbrace{M_1\times d_1+M_2\times(1-d_1)}_{\textbf{type II twin}} \qquad \underbrace{M_1\times d_1+M_3\times(1-d_1)}_{\textbf{type I twin}} \tag{5-2}$$

It is seen that the diagonal components of the four displacement gradient tensors are exactly the same, whereas the off diagonal components are of the same absolute value but sometimes with opposite signs. The maximum deformation appears as a shear $e_{21}$ in the (1 0 0)$_{\mathrm{MgO}}$ plane along the $[0\,1\,0]_{\mathrm{MgO}}$ direction, as highlighted in bold in the matrices in Eq. (5-2).

According to our experimental observations on the low relative contrast zones, the variant pair $V_1$:$V_3$ (or $V_2$:$V_4$) belongs to Type-I twins, and the variant pair $V_1$:$V_2$ (or $V_3$:$V_4$) to Type-II twins. To estimate the overall transformation deformations of the two types of twins, a mean tensor matrix is defined as $M = M_1 \times d_1 + M_{2\,\mathrm{or}\,3} \times (1-d_1)$, where $d_1$ represents the relative volume fraction of one variant. Fig. 5.15 plots the non-zero $e_{ij}$ components of the matrix $M$ against $d_1$ for the Type-I and Type-II twin variant pairs. In the case of the Type-I twins, the $e_{ii}$ components representing dilatation in the three principal directions (Fig. 5.15(a), as well as the $e_{23}$ component representing the shear in the (0 0 1)$_{\mathrm{MgO}}$ plane along the $[0\,1\,0]_{\mathrm{MgO}}$ direction (Fig. 5.15(b)), remain unchanged with the variation of $d_1$. This means that these transformation deformations cannot be accommodated by forming twin variants. However, when the variant volume ratio $d_1$ reaches 0.5, the largest shear $e_{21}$ and the shear

$e_{31}$ are cancelled out. This volume ratio is very close to the thickness ration observed in the present work. For the case of the Type-II twins, the $e_{ii}$ and $e_{31}$ terms stay unchanged under the variant volume change. When the volume ratio reaches 0.5, the largest shear $e_{21}$ and the shear $e_{23}$ are both cancelled out.

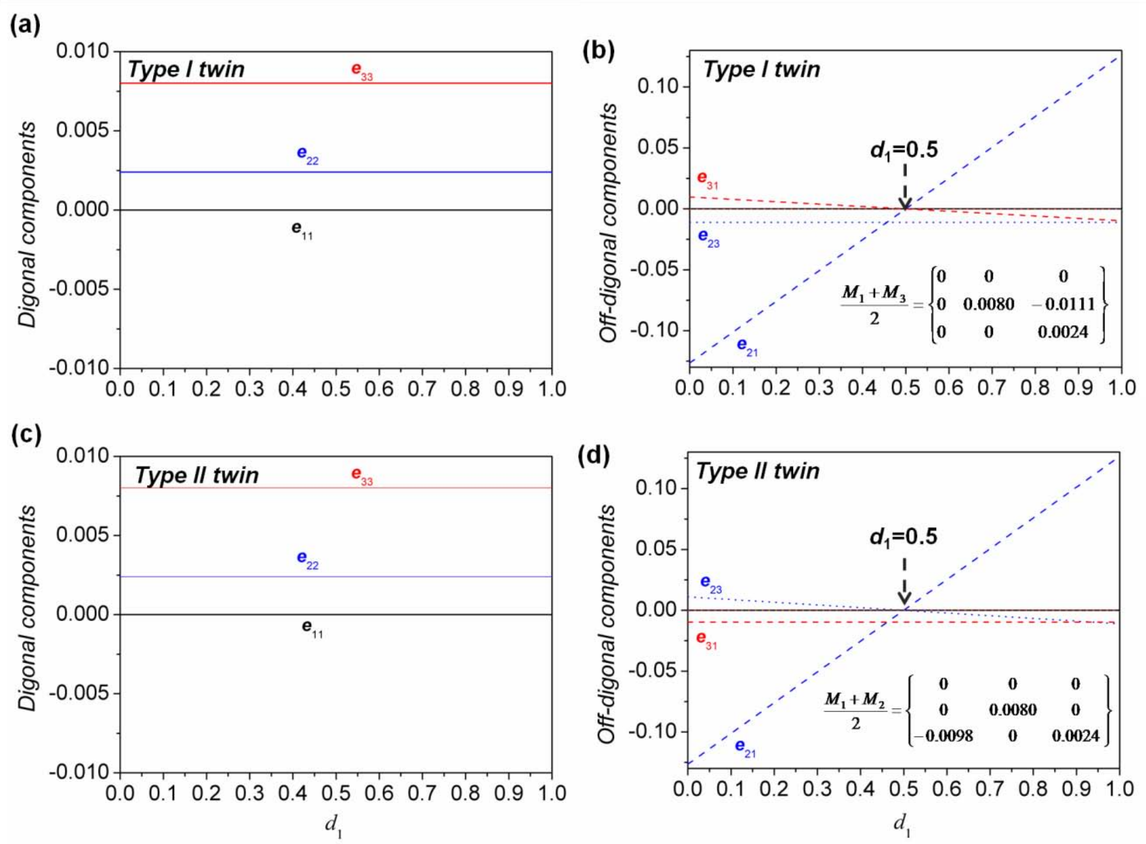

**Fig. 5.15.** Displacement gradient tensor components of (a-b) Type-I twins and (c-d) Type-II twins in the low relative contrast zone, averaged with the volume fractions of two constituent variants.

Based on the above calculation, it could be derived that the dilatation deformations for Type-I and Type-II twins are the same. Moreover, the largest shear deformations ($e_{21}$) of adjacent variants are cancelled out at $d_1$ = 0.5, as illustrated in Fig. 5.16(a) (where the Mn atoms are projected to the substrate surface). The only difference is that the formation of Type-I twins cancels the $e_{31}$ shear components, whereas the formation of Type-II twins cancels the $e_{23}$ shear components. Considering that the thin film is epitaxially grown on a rigid substrate, one can figure out that the external constraints come mainly from the substrate.

The shear deformations in the film normal direction represented by $e_{3j}$ in the matrices are particularly constrained by the substrate, since they tend to "peel" the film off the substrate surface. As illustrated in Fig. 5.16(b) (where the Mn atoms are projected to the $[100]_{\mathrm{MgO}} - [001]_{\mathrm{MgO}}$ cross section), the formation of the Type-I twin pair can well cancel these shear deformations at the macroscopic scale. On the contrary, the formation of the Type-II twin pair further enhances the film “peeling” deformation at the macroscopic scale, and requires elevated formation energy. Therefore, the formation of Type-II twins is limited. This may be the reason why in the low relative contrast zones, Type-I twins appear with much higher frequency compared to the Type-II twins. Moreover, the formation of the Type-I twins does not create any height difference between adjacent variants in the film normal direction ($e_{31}$ and $e_{32}$= 0, and $e_{33}$ is the same for the constituent variants). Thus, a homogenous SE image contrast should be obtained for all the variants.

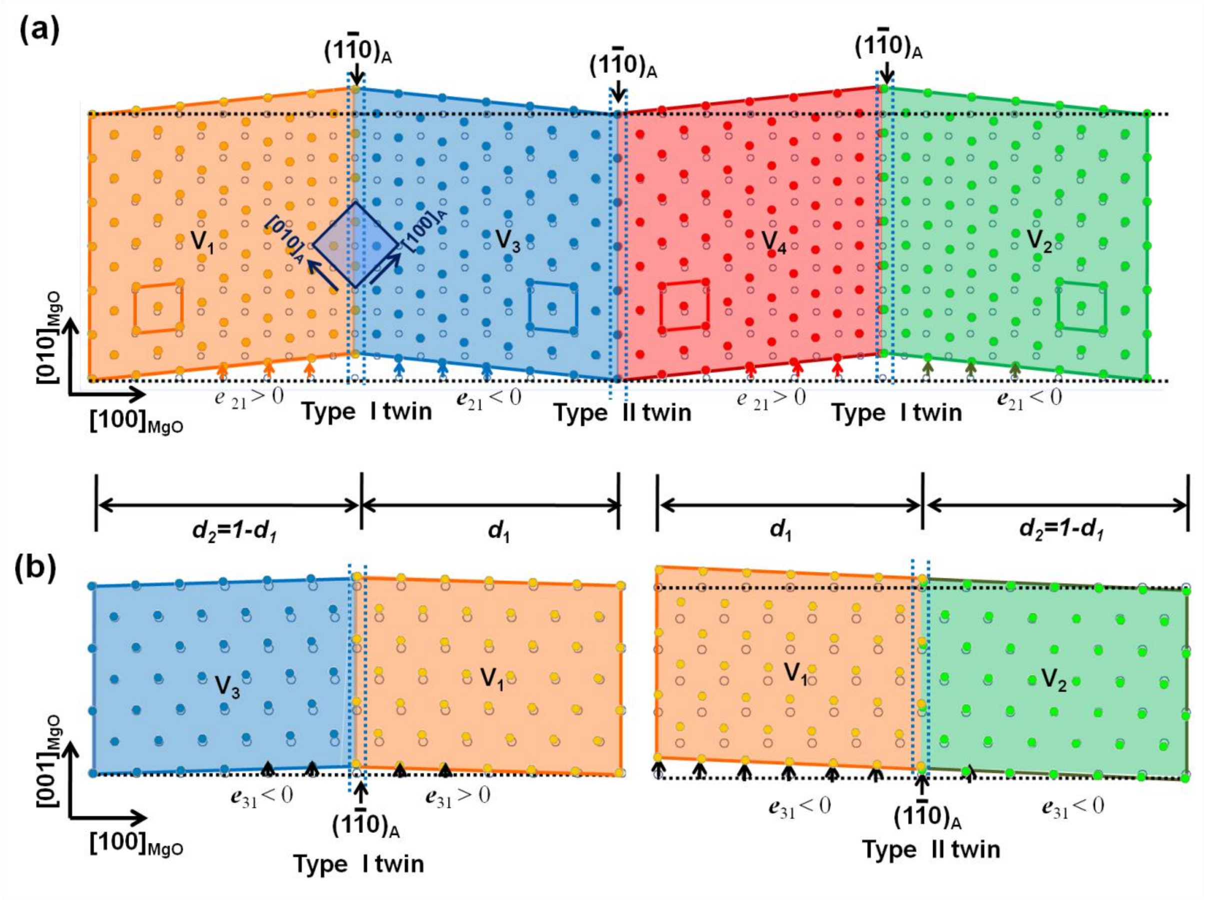

**Fig. 5.16.** Illustration of the shear deformations from austenite to 7M martensite in the low relative contrast zone with respect to the substrate, viewed on (a) the (0 0 1)$_{\mathrm{MgO}}$ plane and (b) the (0 1 0)$_{\mathrm{MgO}}$ plane.

For the high relative contrast zone (Group 2), the displacement gradient tensors of the four 7M variants (V$_A$, V$_B$, V$_C$, V$_D$) in the macroscopic reference frame are:

$$\begin{array}{cccc}
\mathbf{V_A} & \mathbf{V_B} & \mathbf{V_C} & \mathbf{V_D} \\
M_A=\begin{Bmatrix}-0.0289 & -0.0234 & -0.0427\\ -0.0382 & -0.0279 & -0.0524\\ 0.0474 & 0.0363 & \mathbf{0.0672}\end{Bmatrix}_{\mathrm{MgO}} &
M_B=\begin{Bmatrix}0.0422 & 0.0320 & 0.0468\\ 0.0329 & 0.0275 & 0.0370\\ -0.0531 & -0.0420 & -\mathbf{0.0592}\end{Bmatrix}_{\mathrm{MgO}} &
M_C=\begin{Bmatrix}0.0275 & 0.0329 & 0.0370\\ 0.0320 & 0.0422 & 0.0468\\ -0.0420 & -0.0531 & -\mathbf{0.0592}\end{Bmatrix}_{\mathrm{MgO}} &
M_D=\begin{Bmatrix}-0.0279 & -0.0382 & -0.0524\\ -0.0234 & -0.0289 & -0.0427\\ 0.0363 & 0.0474 & \mathbf{0.0672}\end{Bmatrix}_{\mathrm{MgO}}
\end{array} \tag{5-3}$$

$$\underbrace{M_A\times d_1+M_B\times(1-d_1)}_{\textbf{type II twin}} \qquad \underbrace{M_A\times d_1+M_C\times(1-d_1)}_{\textbf{type I twin}}$$

Here, all the components in each displacement gradient tensor are not zero and their absolute values are in the same order of magnitude. The maximum deformation appears as a dilatation in the $[0\,0\,1]_{\mathrm{MgO}}$ direction ($e_{33}$), as highlighted in bold in the matrices in Eq. (5-3).

Following the above analysis scheme for the low relative contrast zones, the non-zero $e_{ij}$ components in the matrix $M$ ($M = M_A \times d_1 + M_{B\,\mathrm{or}\,C} \times (1-d_1)$) were calculated as a function of the volume fraction $d_1$ of variant $V_A$, as shown in Figs. 5.17(a-b) (Type-I twin pair) and Figs. 5.17(c-d) (Type-II twin pair). For the Type-I twin pair, it is seen from Fig. 5.17(a) that the dilatation deformations can be accommodated to some extent through variant volume change, but they cannot be accommodated at one single volume ratio. Indeed, the $e_{11}$ and $e_{22}$ terms are nearly cancelled out at $d_1$ = 0.4876, but the $e_{33}$ term at $d_1$ = 0.5935. Similarly, shear deformation accommodation exists but cannot be achieved at one single volume ratio, as shown in Fig. 5.17(b). The $e_{13}$, $e_{21}$, $e_{23}$ and $e_{31}$ terms are roughly cancelled at $d_1$ = 0.4698 but the $e_{12}$ and $e_{32}$ terms at $d_1$ = 0.5940. If we consider that the $e_{3j}$ terms are the most important components to be accommodated due to the constraints from the rigid substrate, no volume ratio can be reached to cancel these components. When the $e_{31}$ component of the Type-I twin pair equals to zero, the $e_{32}$ component is -0.0111; when the $e_{32}$ component of the Type-I twin equals to zero, the component $e_{31}$ is 0.0111. Therefore, the formation of Type-I twins in the high relative contrast zone is energetically costly.

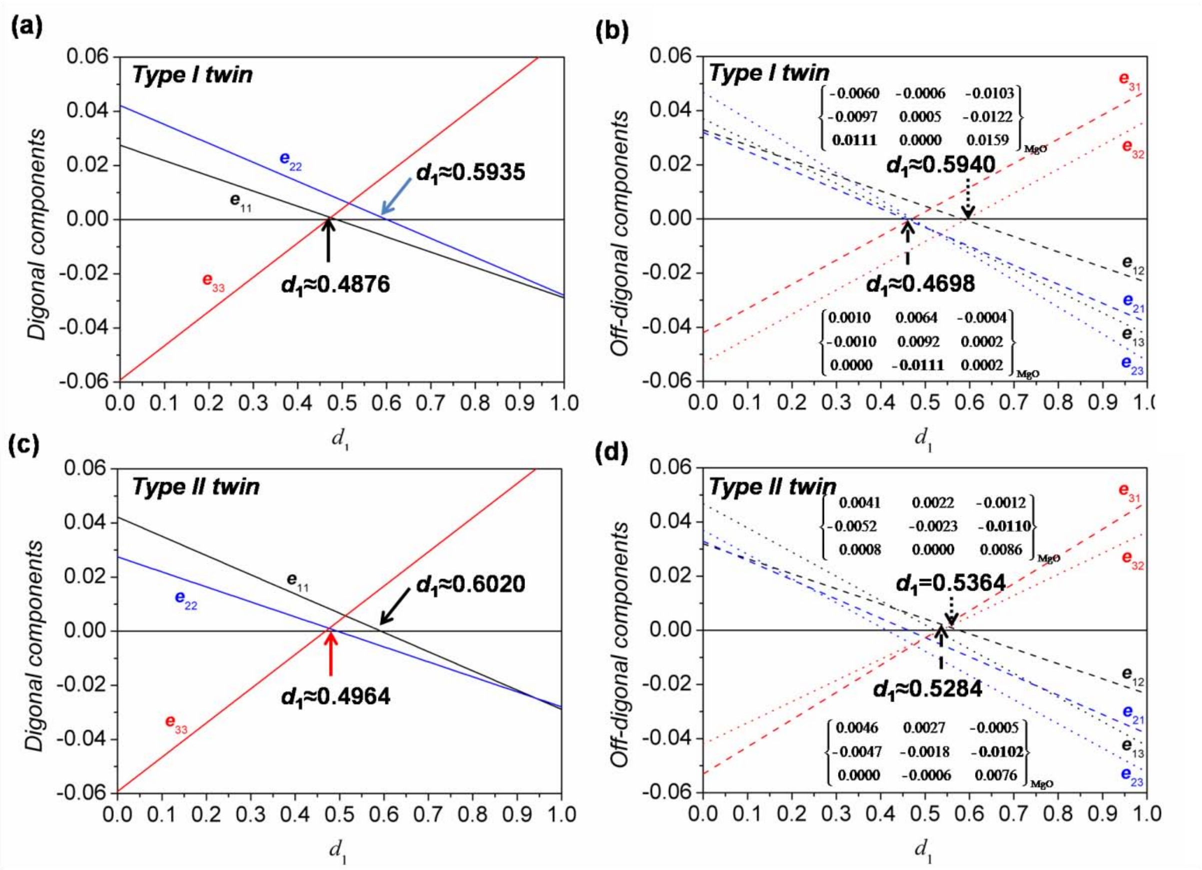

**Fig. 5.17.** Displacement gradient tensor components of (a-b) Type-I twins and (c-d) Type-II twins in the high relative contrast zone, averaged with the volume fractions of two constituent variants.

When the Type-II twin pair forms, the situation for the dilatation deformations is similar to that for the Type-I twin pair. Fig. 5.17(c) shows that the $e_{22}$ and $e_{33}$ terms are nearly cancelled at $d_1$ = 0.4964, whereas the $e_{11}$ term at $d_1$ = 0.6020. For the shear deformations, all the components converge towards zero around $d_1$ = 0.5 (Fig. 5.17d). The $e_{3j}$ term can nearly be cancelled at two volume ratios that are very close, $d_1$ = 0.5284 and $d_1$ = 0.5364. When the $e_{31}$ equals to zero, the $e_{32}$ is -0.0006; when the $e_{32}$ equals to zero, the $e_{31}$ is 0.0008. This indicates that the formation of the Type-II twins in the high relative contrast zone could effectively eliminate the shear deformation along $[0\,0\,1]_{\mathrm{MgO}}$ direction. Moreover, at these volume ratios, the other components have relatively small values as shown in the matrices in Fig. 5.17(d). These volume ratios are very close to the effectively observed thickness ratio and close to the values reported in the literature [43, 44]. In this connection, the formation of the

Type-II twins in high relative contrast zones is energetically favorable and thus, the Type-II twins should appear with higher frequency that is in accordance with our experimental observation. In addition, there exist height differences between adjacent variants, as presented by the $e_{33}$ component of the matrix in Eq. (5-3) for the four 7M variants. This accounts for the high relative contrast between the pairs of variants in the SE images.

### 5.3.4 Crystallography and sequence of martensitic transformation

As mentioned above, the local microscopic microstructural and local crystallographic features in specific martensite variant groups were correlated by EBSD. To obtain the macroscopic crystallographic features, several martensite variant groups in the present NiMnGa thin films were analyzed by EBSD.

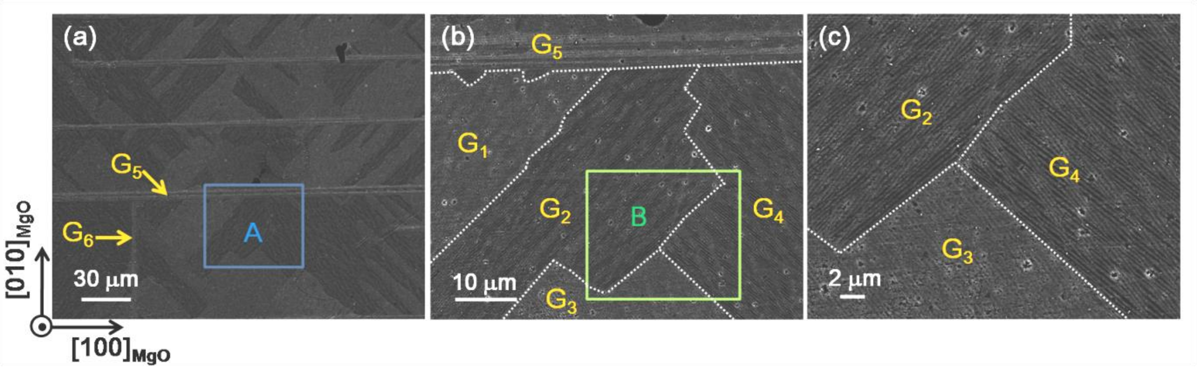

**Fig.5.18** the BSE image of the NiMnGa thin films (a), (b) is the magnification view of area A and (c) is the magnification view of area B. The dotted lines are the variant group boundaries.

Fig.5.18 presents the BSE images of NiMnGa thin films after slight electrolytic polishing. It is seen that macroscopically, martensite variants are organized in colonies or groups, demonstrated by different brightnesses in Fig. 5.18. There are two differently oriented bright long straight strips parallel to the substrate edges ($[100]_{\mathrm{MgO}}$ or $[010]_{\mathrm{MgO}}$) that correspond to the low relative contrast zones mentioned in section 5.3.2. Adjacent to the long strips ($G_5$ and $G_6$), there are several either bright or dark polygonal zones, which are the corresponding high relative contrast zones. Fig.5.18(b) and Fig.5.18(c) are the magnified view that presents the martensite groups. As shown in Fig.5.18(c), although the traces of plate interface in $G_3$ are close to those in $G_4$, the image brightness of the two martensite variant groups ($G_3$ and $G_4$) are different, indicating that group $G_3$ and $G_4$ possess different crystallographic features. As the contrast of a BSE image for a monophase microstructure with homogenous chemical composition originates from the orientation differences of the microstructural components, the difference in contrast between two martensite variant groups indicates the difference in their crystallographic orientations.

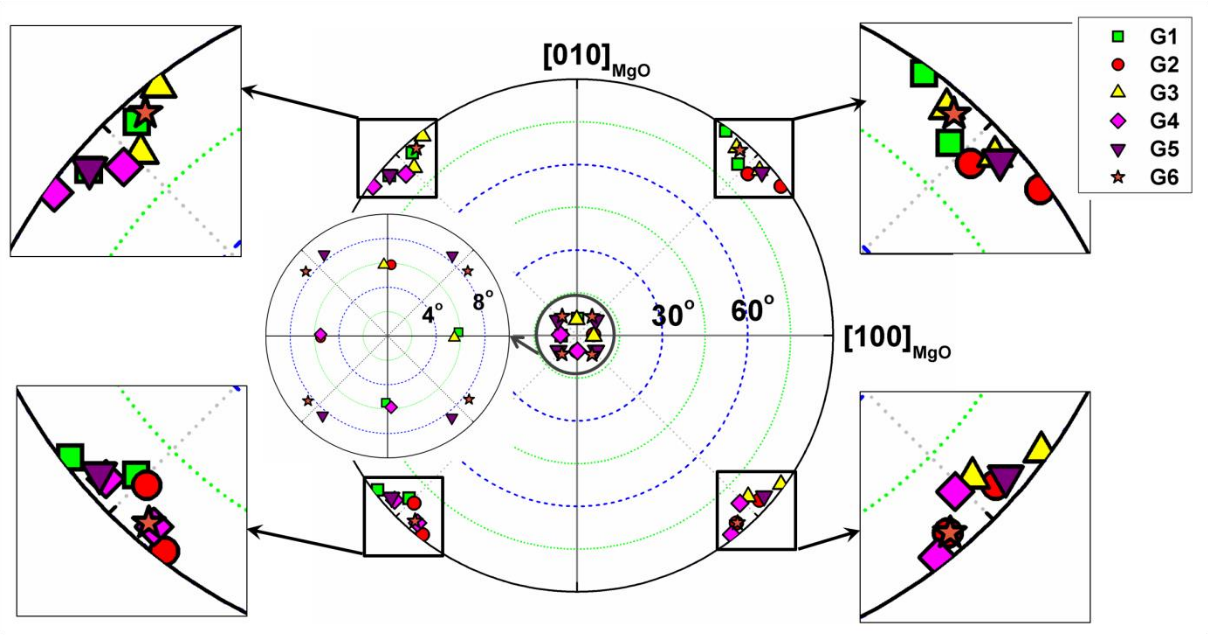

**Fig. 5.19** $(004)_{\mathrm{Tetr}}$ pole figure of NM martensite from the six variant groups determined by EBSD

Large scaled EBSD orientation determination revealed that there are six distinct orientation NM martensite variant groups (G1 – G6), each containing eight orientation NM martensite variants. Therefore, there are in total forty-eight NM martensite variants in the present NiMnGa thin films. To see the forty-eight NM martensite variants, the complete $(004)_{\mathrm{Tetr}}$ pole figure were plotted in Fig.5.19, since only the $(00l)_{Tetr}$ planes have one equivalent plane in terms of the tetragonal symmetry. It is seen from the pole figure in Fig. 5.19, the corresponding 004 poles are mainly located in the central area and the four periphery areas. The macroscopic localization of the variants in each group presented by their geometrical area in the pole figure is summarized in Table 5.7. In the central part there are sixteen NM martensite variants. In the periphery part, each quadrant contains eight NM martensite variants and total thirty-two NM martensite variants.

**Table 5.7** The variant numbers and localization of NM martensite in Fig.5.19

| | | periphery part | | | | |
|---|---|---|---|---|---|---|
| | center | 1st quadrant | 2nd quadrant | 3rd quadrant | 4th quadrant | total |
| $G_1$ | 2 | 2 | 2 | 2 | 0 | 8 |
| $G_2$ | 2 | 2 | 0 | 2 | 2 | 8 |
| $G_3$ | 2 | 2 | 2 | 0 | 2 | 8 |
| $G_4$ | 2 | 0 | 2 | 2 | 2 | 8 |
| $G_5$ | 4 | 1 | 1 | 1 | 1 | 8 |
| $G_6$ | 4 | 1 | 1 | 1 | 1 | 8 |
| Sum | 16 | 8 | 8 | 8 | 8 | 48 |

### 5.3.4.1 Crystallographic orientation of 7M martensite variant

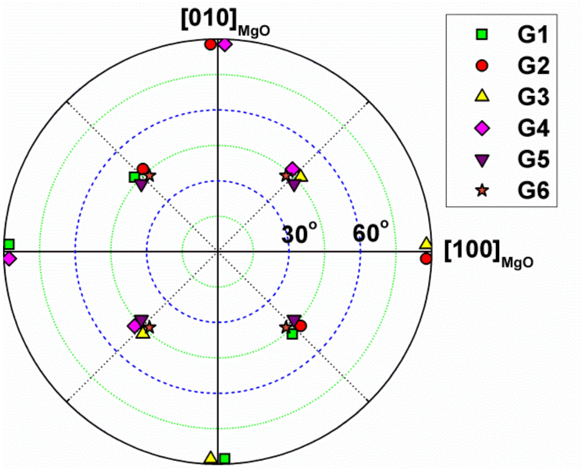

**Fig.5.20** $(001)_{mono}$ pole figure of 7M martensite variants in six variant groups calculated based on the orientation of NM martensite variants.

With the crystallographic orientations of the NM martensite variants in the six variant groups, the crystallographic orientations of 7M martensite variants can be calculated based on the published orientation relationship between 7M and NM martensites [71]. Fig.5.20 presents the $(001)_{mono}$ pole figures of the 7M martensite calculated based on the orientation of the NM martensite variants. As shown in Fig.5.20, there are also six 7M martensite variant groups, each containing 4 distinct variants. Then in total twenty-four 7M martensite variants.

The calculated crystallographic orientation of 7M martensite variants are consistent with that acquired by EBSD in part 5.3.3. It is indicated that the intermartensitic transformation from 7M martensite to NM martensite follows the orientation relationship determined by Li *et.al* [71]. In order to compare the pole figures obtained by EBSD with those by XRD (Fig.4.3) in the present study and previous studies [42, 89], the $(2\ 0\ 20)_{mono}$, $(2\ 0\ \overline{20})_{mono}$, $(0\ 4\ 0)_{mono}$

pole figures of 7M martensite and (2 2 0)$_{Tetr}$, (0 0 4)$_{Tetr}$ pole figures of NM martensite were calculated based on the crystallographic orientations of the variants in the six groups of the respective 7M and NM martensite and displayed in incomplete pole figures in Fig.5.21. Now, the orientation of variants determined by XRD can be explained and correlated with microstructure.

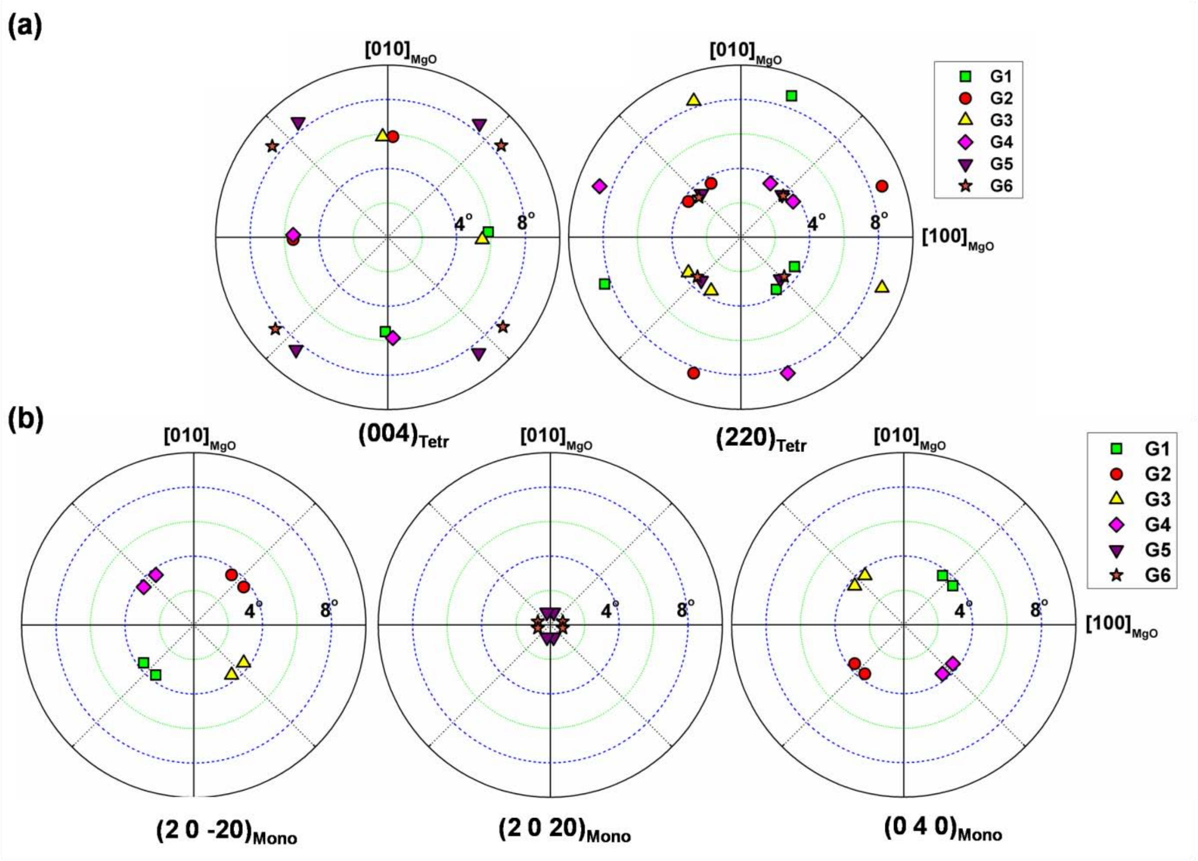

**Fig.5.21** Incomplete pole figures of (a) NM martensite and (b) 7M martensite variants from the six variant groups.

It should be note that for the low contrast zones (G$_5$ and G$_6$), each variant group is composed of four 7M martensite variants with (2 0 20)$_{mono}$ plane parallel to the substrate surfaces, or four major NM martensite variants with their (220)$_{Tetr}$ plane parallel to the substrate surfaces and four minor NM martensite variants with their (004)$_{Tetr}$ plane parallel to the substrate surfaces. It can be concluded that one 7M martensite (2 0 20)$_{mono}$ variant transforms into one NM martensite (2 2 0)$_{Tetr}$ variant and one NM martensite (0 0 4)$_{Tetr}$ variant.

$$\text{7M } (2\ 0\ 20)_{mono} \rightarrow \text{ major NM } (2\ 2\ 0)_{Tetr} + \text{minor NM } (0\ 0\ 4)_{Tetr} \qquad (5\text{-}4)$$

For the high contrast zones ($G_1$, $G_2$, $G_3$, $G_4$), each variant group is composed of two 7M martensite variants with $(2\ 0\ \overline{20})_{mono}$ plane parallel to the substrate surface and two 7M martensite variants with $(0\ 4\ 0)_{mono}$ plane parallel to the substrate surface. The 7M $(2\ 0\ \overline{20})_{mono}$ variant transforms into one major NM $(0\ 0\ 4)_{Tetr}$ variant and one minor NM $(2\ 2\ 0)_{Tetr}$ variant, whereas, the 7M martensite $(0\ 4\ 0)_{mono}$ variant transforms into two NM $(2\ 2\ 0)_{Tetr}$ variants. One is major and the other is minor, as presented in Eq. (5-5) and Eq. (5-6).

$$\text{7M } (2\ 0\ \overline{20})_{mono} \rightarrow \text{major NM } (0\ 0\ 4)_{Tetr} + \text{minor NM } (2\ 2\ 0)_{Tetr} \tag{5-5}$$

$$\text{7M } (0\ 4\ 0)_{mono} \rightarrow \text{major NM } (2\ 2\ 0)_{Tetr} + \text{minor NM } (2\ 2\ 0)_{Tetr} \tag{5-6}$$

### 5.3.4.2 Martensitic transformation sequence

Generally, there are several sequences for the transformation from austenite to NM martensite in NiMnGa alloys that are dependent on the chemical composition. There exist one step transformation and two step transformation. In one step transformation, austenite directly transforms into martensite (NM). In the two step transformation, austenite transform into NM martensite via 7M martensite. In the present study, the transformation sequence from austenite to NM martensite was also verified, based on the published orientation relationship of martensitic and intermartensitic transformation in NiMnGa alloys, as shown in table 5.8.

**Table 5.8** The published orientation relationships of martensitic and intermartensitic transformation in NiMnGa alloys

| Orientation relationship | Austenite | | Martensite | |
|---|---|---|---|---|
| | Plane | direction | Plane | direction |
| Bain | $(001)_A$ | $[100]_A$ | $(001)_{Tetr}$ | $[1\bar{1}0]_{Tetr}$ |
| Kurdjumov-Sachs(K-S) | $(111)_A$ | $[1\bar{1}0]_A$ | $(101)_{Tetr}$ | $[11\bar{1}]_{Tetr}$ |
| Nishiyama-Wassermann(N-W) | $(111)_A$ | $[\bar{2}11]_A$ | $(101)_{Tetr}$ | $[10\bar{1}]_{Tetr}$ |
| Pitsch | $(110)_A$ | $[1\bar{1}0]_A$ | $(1\bar{1}\bar{2})_{Tetr}$ | $[1\bar{1}1]_{Tetr}$ |
| A→7M | $(110)_A$ | $[1\bar{1}0]_A$ | $(1\bar{2}\ \overline{10})_{mono}$ | $[\overline{10}\ \overline{10}\ 1]_{mono}$ |
| 7M→NM | $(001)_{mono}$ | $[100]_{mono}$ | $(112)_{Tetr}$ | $(11\bar{1})_{Tetr}$ |
| or 7M→NM | $(001)_{mono}$ | $[\bar{1}00]_{mono}$ | $(112)_{Tetr}$ | $(11\bar{1})_{Tetr}$ |

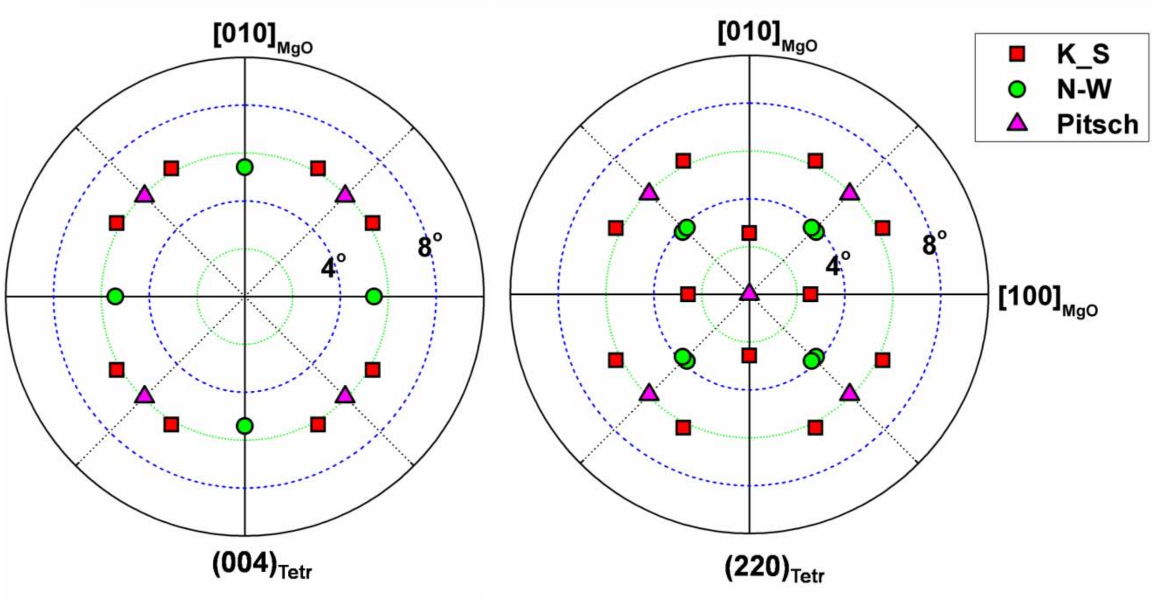

**Fig.5.22** Pole figures of NM martensite variants in the six variant groups

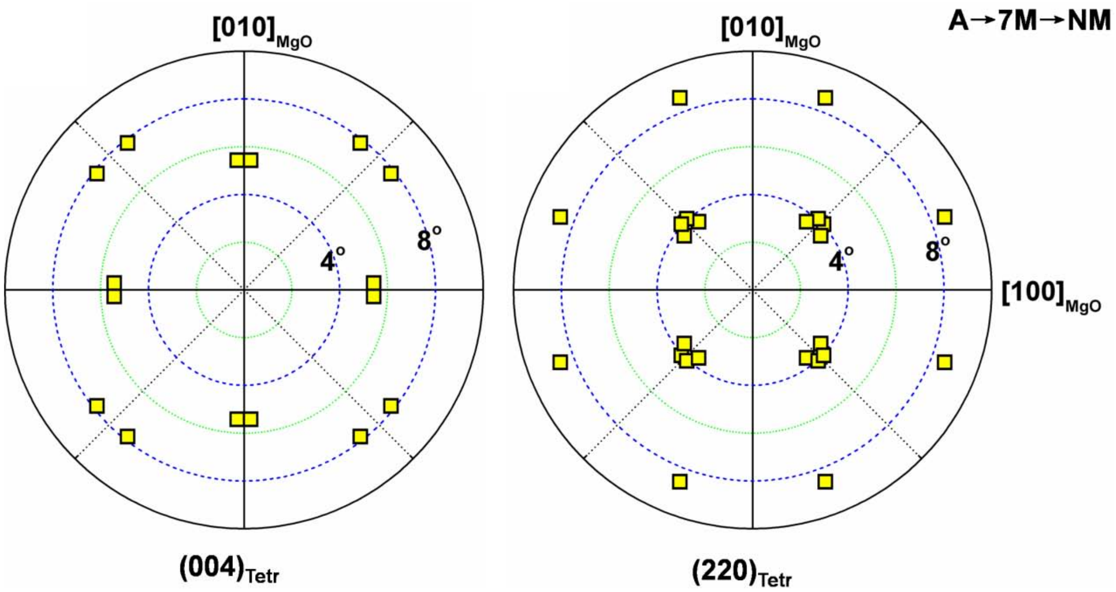

**Fig.5.23** Pole figure of 7M martensite variants in six variant groups

Using the calculation method described in chapter 2 and orientation of austenite determined by STM in the previous work, the crystallographic orientation of NM martensite can be calculated. Fig. 5.22 and Fig.5.23 present the pole figures of NM martensite based on the theoretically calculated crystallographic orientation. As shown in Fig.5.22, the orientations of NM martensite calculated with Pitsch, K-S and N-W orientation relationships for one step transformation are not consistent with those determined by EBSD. This indicates that the NM martensite is not directly transformed from austenite. However, the orientations of NM martensite variants calculate with the transformation sequence from austenite to 7M martensite and then to NM martensite, are consistent with those determined by EBSD. This indicates that the martensitic transformation sequence in the present NiMnGa thin films is from Austenite to 7M martensite and then transform into NM martensite (A→7M→NM).

## 5.4 Summary

Microstructure characterization shows that both the 7M martensite and NM martensite are of plate morphology and organized into two characteristic zones featured with low and high relative SEM second electron image contrast. Local martensite plates with similar plate morphology orientation are organized into variant groups or variant groups. Low relative contrast zones consists of long straight plates running with their length direction parallel to the substrate edges, whereas the high relative contrast zones consists of shorter and bent plates with the length direction roughly in 45 °against the substrate edges.

SEM-EBSD in film depth analyses further verified the co-existence of the three constituent phases: austenite, 7M martensite and NM martensite. NM martensite is located near the free surface of the film, austenite above the substrate surface, and 7M martensite in the intermediate layers between austenite and NM martensite.

Further EBSD characterization indicates that there are four distinct martensite plates in each variant group for both NM and 7M martensite. Each NM plate is composed of paired major and minor lamellar variants (*i.e.* $(112)_{\mathrm{Tetr}}$ compound twins) in terms of their thicknesses having a coherent interlamellar interface, whereas, each 7M martensite plate contains one orientation variant. Thus, there are four orientation 7M martensite variants and eight orientation NM martensite variants in one variant group.

For NM martensite, in the low relative contrast zones, the long and straight inter-plate interfaces between adjacent NM plates result from the configuration of the counterpart $(112)_{\mathrm{Tetr}}$ compound twins that have the same orientation combination and are distributed symmetrically to the macroscopic plate interfaces. As there are no microscopic height misfits across plate interfaces in the film normal direction, the relative contrasts of adjacent NM plates are not distinct in the SE image. However, in the high relative contrast zones, the asymmetrically distributed $(112)_{\mathrm{Tetr}}$ compound twins in adjacent NM plates lead to the change of inter-plate interface orientation. The pronounced height misfits across inter-plate interfaces in the film normal direction give rise to the surface reliefs, hence high relative contrast between adjacent plates.

For 7M martensite, both Type-I and Type-II twin interfaces are nearly perpendicular to the substrate surface in the low relative contrast zones. The Type-I twin pairs appear with much higher frequency, as compared with that of the Type-II twin pairs. However, there are two Type-II twin interface trace orientations and one Type-I twin interface trace orientation in the high relative contrast zones. The Type-II twin pairs are more frequent than the Type-I twin pairs. The inconsistent occurrences of the different types of twins in different zones are originated from the substrate constrain.

The crystallographic calculation also indicates that the martensitic transformation sequence is from Austenite to 7M martensite and then to NM martensite (A→7M→NM). The present study intends to offer deep insights into the crystallographic features and martensitic transformation of epitaxial NiMnGa thin films.

# Chapter 6 Conclusions

## 6.1 Conclusions

In conclusion, both NiMnGa thin films with column and continuous microstructures were successfully fabricated by DC magnetron sputtering, after the optimization of sputtering parameters such as substrate temperature, sputtering power, substrate, seed-layer, film composition and thickness.

X-ray diffraction analysis demonstrates that three different phases, *i.e.* austenite, 7M modulated martensite, and NM martensite, co-exist in the as-deposited epitaxial $Ni_{50}Mn_{30}Ga_{20}$ thin films. The austenite phase has a cubic $L2_1$ crystal structure ($Fm\overline{3}m$, No. 225) with lattice constant $a_A$ = 0.5773 nm. The 7M martensite phase has an incommensurate monoclinic crystal structure ($P2/m$, No. 10) with lattice constants $a_{7M}$ = 0.4262 nm, $b_{7M}$ = 0.5442 nm, $c_{7M}$ = 4.1997 nm, and $\beta = 93.7^o$. The NM martensite phase is of tetragonal crystal structure ($I4/mmm$, No. 139) with lattice constants $a_{NM}$ = 0.3835 nm and $c_{NM}$ =0.6680 nm.

By the combined the XRD and EBSD orientation characterizations, it is revealed that the as-deposited microstructures is mainly composed of the tetragonal NM martensite at the film surface and the monoclinic 7M martensite beneath the surface layer. For the NM martensite, there are two characteristic zones featured respectively with low and high relative SE image contrast. The NM martensite in the low relative contrast zones consists of long straight plates running with their length direction parallel to the substrate edges, whereas the NM martensite in the high relative contrast zones consists of shorter and bent plates with the length direction roughly in 45 ° against the substrate edges.

Each NM plate is composed of paired major and minor lamellar variants (*i.e.* $(112)_{Tetr}$ compound twins) having a coherent interlamellar interface. There are in total eight orientation variants in one variant group. Indeed, in the low relative contrast zones, the long and straight inter-plate interfaces between adjacent NM plates result from the configuration of the counterpart $(112)_{Tetr}$ compound twins that have the same orientation combination and are distributed symmetrically to the macroscopic plate interfaces. As there are no microscopic height misfits across plate interfaces in the film normal direction, the relative contrasts of adjacent NM plates are not distinct in the SE image. However, in the high relative contrast zones, the asymmetrically distributed $(112)_{\mathrm{Tetr}}$ compound twins in adjacent NM plates lead to the change of inter-plate interface orientation. The pronounced height misfits across inter-plate interfaces in the film normal direction give rise to the surface reliefs, hence high relative contrast between adjacent plates.

The plate-like microstructures of the 7M martensite are composed of two distinct kinds of plate groups too. Each 7M martensite plate contains one orientation variant. There are four orientation variants in one plate group. The inter-plate interfaces are either Type-I or Type-II twin interfaces. The Type-I twin pairs appear with much higher frequency, as compared with the Type-II twin pairs. The rigid constraint from the substrate accounts for this preference. Due to the fact that the formation of Type-I twin pair can cancel the shear deformation in the film normal direction at macroscopic scale (this shear tends to “peel” the film off the substrate) and requires much lower effort.

In the high relative contrast zones, there exists one interface trace orientation for Type-I twins but two interface trace orientations for Type-II twins on the film surface. In contrast to the low relative contrast zones, the Type-II twin pairs are more frequent than the Type-I twin pairs, due to the constraint from the rigid substrate. The formation of Type-II twin pair allows cancelling the shear deformation in the film normal direction at macroscopic scale. Large relative height differences between adjacent variants account for the high relative contrast.

Crystallographic calculation indicates that the martensitic transformation sequence is from Austenite to 7M martensite and then to NM martensite (A→7M→NM). The present study intends to offer deep insights into the crystallographic features and martensitic transformation of epitaxial NiMnGa thin films.

# Bibliography

[1] Gibbs M R J, Hill E W, Wright P. *Chapter Six Magnetic Microelectromechanical Systems: MagMEMS*, In: Buschow KHJ, editor. **Handbook of Magnetic Materials**, vol. Volume 17. Elsevier, 2007:457-526.

[2] Zhu Y, Yu K. *A model considering mechanical anisotropy of magnetic-field-induced superelastic strain in magnetic shape memory alloys,* **Journal of Alloys and Compounds**, 2013, 550 (0): 308-313.

[3] Bhattacharya K, James R D. *A theory of thin films of martensitic materials with applications to microactuators*, **Journal of the Mechanics and Physics of Solids**, 1999, 47 (3): 531-576.

[4] Ripka P, Závěta K. *Chapter Three Magnetic Sensors: Principles and Applications*, In: Buschow KHJ, editor. **Handbook of Magnetic Materials**, vol.18. Elsevier, 2009:347-420.

[5] Barthélémy A, Fert A, Petroff F. *Chapter 1 Giant magnetoresistance in magnetic multilayers*, In: Buschow KHJ, editor. **Handbook of Magnetic Materials**, vol.12. Elsevier, 1999:1-96.

[6] Söderberg O, Sozinov A, Ge Y, *et al. chapter 1 Giant Magnetostrictive Materials*, In: Buschow KHJ, editor. **Handbook of Magnetic Materials**, vol.16. Elsevier, 2006:1-39.

[7] Wu R Q. *Origin of large magnetostriction in FeGa alloys,* **Journal of Applied Physics**, 2002, 91 (10): 7358-7360.

[8] Kokorin V V, Wuttig M. *Magnetostriction in ferromagnetic shape memory alloys*, **Journal of Magnetism and Magnetic Materials**, 2001, 234 (1): 25-30.

[9] Fukuda T, Nakamura Y, Tabata T, *et al. Giant magnetostriction in Fe-based ferromagnetic shape memory alloys*, **Pricm 4: Forth Pacific Rim International Conference on Advanced Materials and Processing, Vols I and Ii**,Sendai*:* Japan Inst Metals, 2001: 1699-1702.

[10] O'Handley R C. *Modern magnetic materials: principles and applications*,New York*:* John Wiley & Sons 2000: 1-740.

[11] Manfred Kohl, Berthold Krevet, Makoto Ohtsuka, *et al. Ferromagnetic Shape Memory Microactuators*, **Materials Transactions**, 2006, 47 (3): 639-644.

[12] Faehler S. *An Introduction to Actuation Mechanisms of Magnetic Shape Memory Alloys,* **ECS Transactions**, 2007, 3 (25): 155-163.

[13] Mohd Jani J, Leary M, Subic A, *et al. A review of shape memory alloy research, applications and opportunities*, **Materials & Design**, 2014, 56: 1078-1113.

[14] Jiles D C. *Recent advances and future directions in magnetic materials,* **Acta Materialia**, 2003, 51 (19): 5907-5939.

[15] Wilson S A, Jourdain R P J, Zhang Q, *et al. New materials for micro-scale sensors and actuators: An engineering review*, **Materials Science and Engineering: R: Reports**, 2007, 56 (1–6): 1-129.

[16] Nespoli A, Besseghini S, Pittaccio S, *et al. The high potential of shape memory alloys in developing miniature mechanical devices: A review on shape memory alloy mini-actuators*, **Sensors and Actuators A: Physical**, 2010, 158 (1): 149-160.

[17] Hauser H, Chabicovsky R, Riedling K. *Chapter 8 - Thin magnetic films*, In: Hari Singh N, M.Sc, Ph.D.A2 - Hari Singh Nalwa MSPD, editors. **Handbook of Thin Films**. Burlington: Academic Press, 2002:375-437.

[18] Acet M, Mañosa L, Planes A. *Chapter Four - Magnetic-Field-Induced Effects in Martensitic Heusler-Based Magnetic Shape Memory Alloys*, In: Buschow KHJ, editor. **Handbook of Magnetic Materials**, vol.19. Elsevier, 2011:231-289.

[19] Sozinov A, Lanska N, Soroka A, *et al. 12% magnetic field-induced strain in Ni-Mn-Ga-based non-modulated martensite*, **Applied Physics Letters**, 2013, 102 (2): 021902-1-5.

[20] Sozinov A, Likhachev A A, Lanska N, *et al. Giant magnetic-field-induced strain in NiMnGa seven-layered martensitic phase*, **Applied Physics Letters**, 2002, 80 (10): 1746-1748.

[21] Kohl M, Reddy Y S, Khelfaoui F, *et al. Recent Progress in FSMA Microactuator Developments,* **Materials Science Forum**, 2009, 635: 145-154.

[22] Xu H, Wang J, Jiang C, *et al. Ni–Mn–Ga shape memory alloys development in China*, **Current Opinion in Solid State and Materials Science**, 2005, 9 (6): 319-325.

[23] Cong D Y, Wang Y D, Peng R L, *et al. Crystal structures and textures in the hot-forged Ni-Mn-Ga shape memory alloys,* **Metallurgical and Materials Transactions a-Physical Metallurgy and Materials Science**, 2006, 37A (5): 1397-1403.

[24] Cong D Y, Zetterstrom P, Wang Y D, *et al. Crystal structure and phase transformation in Ni53Mn25Ga22 shape memory alloy from 20 K to 473 K,* **Applied Physics Letters**, 2005, 87 (11): 111906-1-3.

[25] Cong D Y, Wang Y D, Zetterstrom P, *et al. Crystal structures and textures of hot forged Ni48Mn30Ga22 alloy investigated by neutron diffraction technique*, **Materials Science and Technology**, 2005, 21 (12): 1412-1416.

[26] Li Z B, Xu N, Zhang Y D, *et al. Composition-dependent ground state of martensite in Ni–Mn–Ga alloys,* **Acta Materialia**, 2013, 61 (10): 3858-3865.

[27] Li Z B, Llamazares J L S, Sanchez-Valdes C F, *et al. Microstructure and magnetocaloric effect of melt-spun Ni52Mn26Ga22 ribbon,* **Applied Physics Letters**, 2012, 100 (17): 174102-1-4.

[28] Li Z, Zhang Y, Esling C, *et al. Twin relationships of 5M modulated martensite in Ni–Mn–Ga alloy*, **Acta Materialia**, 2011, 59 (9): 3390-3397.

[29] Wang J, Sehitoglu H. *Twinning stress in shape memory alloys: Theory and experiments*, **Acta Materialia**, 2013, 61 (18): 6790-6801.

[30] Pond R C, Muntifering B, Müllner P. *Deformation twinning in Ni2MnGa*, **Acta Materialia**, 2012, 60 (9): 3976-3984.

[31] Matsuda M, Yasumoto Y, Hashimoto K, *et al. Transmission Electron Microscopy of Twins in 10M Martensite in Ni–Mn–Ga Ferromagnetic Shape Memory Alloy*, **Materials Transactions**, 2012, 53 (5): 902-906.

[32] Murray S J, Marioni M, Allen S M, *et al. 6% magnetic-field-induced strain by twin-boundary motion in ferromagnetic Ni--Mn--Ga*, **Applied Physics Letters**, 2000, 77 (6): 886-888.

[33] Backen A, Yeduru S R, Diestel A, *et al. Epitaxial Ni-Mn-Ga Films for Magnetic Shape Memory Alloy Microactuators*, **Advanced Engineering Materials**, 2012, 14 (8): 696-709.

[34] Eichhorn T, Hausmanns R, Jakob G. *Microstructure of freestanding single-crystalline Ni2MnGa thin films*, **Acta Materialia**, 2011, 59 (13): 5067-5703.

[35] Dunand D C, Müllner P. *Size Effects on Magnetic Actuation in Ni-Mn-Ga Shape-Memory Alloys*, **Advanced Materials**, 2011, 23 (2): 216-232.

[36] Chernenko V A, Anton R L, Kohl M, *et al. Magnetic domains in Ni–Mn–Ga martensitic thin films*, **Journal of Physics: Condensed Matter**, 2005, 17 (34): 5215-5224.

[37] Hakola A, Heczko O, Jaakkola A, *et al. Ni–Mn–Ga films on Si, GaAs and Ni–Mn–Ga single crystals by pulsed laser deposition*, **Applied Surface Science**, 2004, 238 (1-4): 155-158.

[38] Dong J W. *Shape memory and ferromagnetic shape memory effects in single-crystal Ni[sub 2]MnGa thin films*, **Journal of Applied Physics**, 2004, 95 (5): 2593-2600.

[39] Castano F J, Nelson-Cheeseman B, O'Handley R C, *et al. Structure and thermomagnetic properties of polycrystalline Ni--Mn--Ga thin films*, **Journal of Applied Physics**, 2003, 93 (10): 8492-8494.

[40] Dong J W, Chen L C, Xie J Q, *et al. Epitaxial growth of ferromagnetic Ni[sub 2]MnGa on GaAs(001) using NiGa interlayers*, **Journal of Applied Physics**, 2000, 88 (12): 7357-7359.

[41] Dong J W, Chen L C, Palmstrøm C J, *et al. Molecular beam epitaxy growth of ferromagnetic single crystal (001) Ni[sub 2]MnGa on (001) GaAs*, **Applied Physics Letters**, 1999, 75 (10): 1443-1445.

[42] Tillier J, Bourgault D, Odier P, *et al. Tuning macro-twinned domain sizes and the b-variants content of the adaptive 14-modulated martensite in epitaxial Ni–Mn–Ga films by co-sputtering*, **Acta Materialia**, 2011, 59 (1): 75-81.

[43] Leicht P, Laptev A, Fonin M, *et al. Microstructure and atomic configuration of the (001)-oriented surface of epitaxial Ni–Mn–Ga thin films*, **New Journal of Physics**, 2011,

13 (3): 033021-1-14.

[44] Kaufmann S, Niemann R, Thersleff T, *et al. Modulated martensite: why it forms and why it deforms easily*, **New Journal of Physics**, 2011, 13 (5): 053029-1-24.

[45] Tillier J, Bourgault D, Pairis S, *et al. Martensite structures and twinning in substrate-constrained epitaxial Ni–Mn–Ga films deposited by a magnetron co-sputtering process*, **Physics Procedia**, 2010, 10 (0): 168-173.

[46] Kallmayer M, Pörsch P, Eichhorn T, *et al. Compositional dependence of element-specific magnetic moments in Ni 2 MnGa films*, **Journal of Physics D: Applied Physics**, 2009, 42 -(8): 084008-1-8.

[47] Annadurai A, Nandakumar A K, Jayakumar S, *et al. Composition, structure and magnetic properties of sputter deposited Ni–Mn–Ga ferromagnetic shape memory thin films*, **Journal of Magnetism and Magnetic Materials**, 2009, 321 (6): 630-634.

[48] Witherspoon C, Zheng P, Chmielus M, *et al. Texture and training of magnetic shape memory foam*, **Acta Materialia**, 2013, 61 (6): 2113-2120.

[49] Wang J, Steinmann P. *A variational approach towards the modeling of magnetic field-induced strains in magnetic shape memory alloys*, **Journal of the Mechanics and Physics of Solids**, 2012, 60 (6): 1179-1200.

[50] Gaitzsch U, Klauß H, Roth S, *et al. Magnetomechanical training of single crystalline Ni–Mn–Ga alloy*, **Journal of Magnetism and Magnetic Materials**, 2012, 324 (4): 430-433.

[51] Chulist R, Pagounis E, Böhm A, *et al. Twin boundaries in trained 10M Ni−Mn−Ga single crystals*, **Scripta Materialia**, 2012, 67 (4): 364-367.

[52] Chmielus M, Chernenko V A, Knowlton W B, *et al. Training, constraints, and high-cycle magneto-mechanical properties of Ni-Mn-Ga magnetic shape-memory alloys*, **The European Physical Journal Special Topics**, 2008, 158 (1): 79-85.

[53] Liu J, Gottschall T, Skokov K P, *et al. Giant magnetocaloric effect driven by structural transitions*, **Nature Materials**, 2012, 11: 620-626.

[54] Kainuma R, Imano Y, Ito W, *et al. Magnetic-field-induced shape recovery by reverse phase transformation*, **Nature**, 2006, 439 (7079): 957-960.

[55] Thomas M, Heczko O, Buschbeck J, *et al. Magnetically induced reorientation of martensite variants in constrained epitaxial Ni–Mn–Ga films grown on MgO(001)*, **New Journal of Physics**, 2008, 10 (2): 023040-1-20.

[56] Tickle R. *Ferromagnetic Shape Memory Materials*, Minnesota, 2000.

[57] Zhu W, Liu E K, Feng L, *et al. Magnetic-field-induced transformation in FeMnGa alloys*, **Applied Physics Letters**, 2009, 95 (22): 222512 -1-3.

[58] Hernando B, Llamazares J L S, Santos J D, *et al. Thermal and magnetic field-induced martensite-austenite transition in Ni(50.3)Mn(35.3)Sn(14.4) ribbons*, **Applied Physics**

**Letters**, 2008, 92 (4): 042504 -1-3.

[59] Krenke T, Acet M, Wassermann E F, *et al. Martensitic transitions and the nature of ferromagnetism in the austenitic and martensitic states of Ni-Mn-Sn alloys*, **Physical Review B**, 2005, 72 (1): 014412-1-9.

[60] Pons J, Santamarta R, Chernenko V, *et al. Structure of the layered martensitic phases of Ni–Mn–Ga alloys*, **Materials Science and Engineering: A**, 2006, 438-440: 931-934.

[61] Pons J, Chernenko V A, Santamarta R, *et al. Crystal structure of martensitic phases in Ni–Mn–Ga shape memory alloys*, **Acta Materialia**, 2000, 48 (12): 3027-3038.

[62] Banik S, Ranjan R, Chakrabarti A, *et al. Structural studies of Ni_{2+x}Mn_{1−x}Ga by powder x-ray diffraction and total energy calculations*, **Physical Review B**, 2007, 75 (10): 104107-1-9.

[63] Righi L, Albertini F, Villa E, *et al. Crystal structure of 7M modulated Ni–Mn–Ga martensitic phase*, **Acta Materialia**, 2008, 56 (16): 4529-4535.

[64] Righi L, Albertini F, Pareti L, *et al. Commensurate and incommensurate "5M" modulated crystal structures in Ni–Mn–Ga martensitic phases*, **Acta Materialia**, 2007, 55 (15): 5237-5245.

[65] Righi L, Albertini F, Calestani G, *et al. Incommensurate modulated structure of the ferromagnetic shape-memory Ni2MnGa martensite*, **Journal of Solid State Chemistry**, 2006, 179 (11): 3525-3533.

[66] Chulist R, Sozinov A, Straka L, *et al. Diffraction study of bending-induced polysynthetic twins in 10M modulated Ni-Mn-Ga martensite*, **Journal of Applied Physics**, 2012, 112 (6): 063517-1-7.

[67] Heczko O, Straka L, Seiner H. *Different microstructures of mobile twin boundaries in 10M modulated Ni–Mn–Ga martensite*, **Acta Materialia**, 2013, 61 (2): 622-631.

[68] Chulist R, Straka L, Lanska N, *et al. Characterization of mobile type I and type II twin boundaries in 10M modulated Ni–Mn–Ga martensite by electron backscatter diffraction*, **Acta Materialia**, 2013, 61 (6): 1913-1920.

[69] Cong D Y, Zhang Y D, Esling C, *et al. Microstructural and crystallographic characteristics of interpenetrating and non-interpenetrating multiply twinned nanostructure in a Ni–Mn–Ga ferromagnetic shape memory alloy*, **Acta Materialia**, 2011, 59 (18): 7070-7081.

[70] Cong D Y, Zhang Y D, Wang Y D, *et al. Experiment and theoretical prediction of martensitic transformation crystallography in a Ni-Mn-Ga ferromagnetic shape memory alloy*, **Acta Materialia**, 2007, 55 (14): 4731-4740.

[71] Li Z, Yang B, Zhang Y, *et al. Crystallographic insights into the intermartensitic transformation in Ni–Mn–Ga alloys*, **Acta Materialia**, 2014, 74: 9-17.

[72] Li Z B, Zhang Y D, Esling C, *et al. Evidence for a monoclinic incommensurate*

*superstructure in modulated martensite*, **Acta Materialia**, 2012, 60 (20): 6982-6990.

[73] Li Z B, Zhang Y D, Esling C, *et al. Determination of the orientation relationship between austenite and incommensurate 7M modulated martensite in Ni-Mn-Ga alloys*, **Acta Materialia**, 2011, 59 (7): 2762-2772.

[74] Li Z B, Zhang Y D, Esling C, *et al. New approach to twin interfaces of modulated martensite*, **Journal of Applied Crystallography**, 2010, 43 (3): 617-622.

[75] Thomas M, Heczko O, Buschbeck J, *et al. Stress induced martensite in epitaxial Ni–Mn–Ga films deposited on MgO(001)*, **Applied Physics Letters**, 2008, 92 (19): 192515-1-3.

[76] Hakola A, Heczko O, Jaakkola A, *et al. Pulsed laser deposition of NiMnGa thin films on silicon*, **Applied Physics a-Materials Science & Processing**, 2004, 79 (4-6): 1505-1508.

[77] Yeduru S R, Backen A, Kübel C, *et al. Microstructure of free-standing epitaxial Ni–Mn–Ga films before and after variant reorientation*, **Scripta Materialia**, 2012, 66 (8): 566-569.

[78] Jetta N, Ozdemir N, Rios S, *et al. Phase transformations in sputtered Ni-Mn-Ga magnetic shape memory alloy thin films*, **Thin Solid Films**, 2012, 520 (9): 3433-3439.

[79] Heczko O, Thomas M, Buschbeck J, *et al. Epitaxial Ni–Mn–Ga films deposited on SrTiO[sub 3] and evidence of magnetically induced reorientation of martensitic variants at room temperature*, **Applied Physics Letters**, 2008, 92 (7): 072502-1-3.

[80] Khelfaoui F, Kohl M, Buschbeck J, *et al. A fabrication technology for epitaxial Ni-Mn-Ga microactuators*, **The European Physical Journal Special Topics**, 2008, 158 (1): 167-172.

[81] Ranzieri P, Fabbrici S, Nasi L, *et al. Epitaxial Ni–Mn–Ga/MgO(100) thin films ranging in thickness from 10 to 100nm*, **Acta Materialia**, 2013, 61 (1): 263-272.

[82] Jakob A M, Müller M, Rauschenbach B, *et al. Nanoscale mechanical surface properties of single crystalline martensitic Ni–Mn–Ga ferromagnetic shape memory alloys*, **New Journal of Physics**, 2012, 14 (3): 033029-1-16.

[83] Luo Y, Leicht P, Laptev A, *et al. Effects of film thickness and composition on the structure and martensitic transition of epitaxial off-stoichiometric Ni–Mn–Ga magnetic shape memory films*, **New Journal of Physics**, 2011, 13 (1): 013042-1-14.

[84] Kauffmann-Weiss S, Gruner M E, Backen A, *et al. Magnetic Nanostructures by Adaptive Twinning in Strained Epitaxial Films*, **Physical Review Letters**, 2011, 107 (20): 206105-1-5.

[85] Ge Y, Heczko O, Hannula S P, *et al. Probing structure and microstructure of epitaxial Ni–Mn–Ga films by reciprocal space mapping and pole figure measurements*, **Acta Materialia**, 2010, 58 (20): 6665-6671.

[86] Backen A, Yeduru S R, Kohl M, *et al. Comparing properties of substrate-constrained and freestanding epitaxial Ni-Mn-Ga films*, **Acta Materialia**, 2010, 58 (9): 3415-3421.

[87] Thomas M, Heczko O, Buschbeck J, *et al. Stray-Field-Induced Actuation of Free-Standing Magnetic Shape-Memory Films*, **Advanced Materials**, 2009, 21 (36): 3708-3711.

[88] Buschbeck J, Niemann R, Heczko O, *et al. In situ studies of the martensitic transformation in epitaxial Ni–Mn–Ga films*, **Acta Materialia**, 2009, 57 (8): 2516-2526.

[89] Kaufmann S, Rößler U K, Heczko O, *et al. Adaptive Modulations of Martensites*, **Physical Review Letters**, 2010, 104 (14): 145702-1-4.

[90] Niemann R, Rößler U K, Gruner M E, *et al. The Role of Adaptive Martensite in Magnetic Shape Memory Alloys*, **Advanced Engineering Materials**, 2012, 14 (8): 562-581.

[91] Backen A, Kauffmann-Weiss S, Behler C, *et al. Mesoscopic twin boundaries in epitaxial Ni-Mn-Ga films*. http://arxiv.org/abs/1311.5428., 2013: 1-17.

[92] Bunge H J, Esling C, Muller J. *The role of the inversion centre in texture analysis*, **Journal of Applied Crystallography**, 1980, 13: 544-554.

[93] Bunge H J. *Texture analysis in materials science-mathematical methods.* ,Gottingen*:* Cuvillier Press, 1993: 1-593.

[94] Humbert M, Wagner F, Moustahfid H, *et al. Determination of the Orientation of a Parent [beta] Grain from the Orientations of the Inherited [alpha] Plates in the Phase Transformation from Body-Centred Cubic to Hexagonal Close Packed*, **Journal of Applied Crystallography**, 1995, 28 (5): 571-576.

[95] Zhang Y D, Li Z B, Esling C, *et al. A general method to determine twinning elements*, **Journal of Applied Crystallography**, 2010, 43: 1426-1430.

[96] Bain E C. *the nature of martensite*, **Trans. AIME**, 1924, 70: 25-46.

[97] Kurdjumov G, Sachs G. **Z. Phys**, 1930, 64: 325-343.

[98] Nishyama Z. *X-ray investigation on the mechanism of tranformation from face-centered cubic lattive to body-centered cubic lattice*, **Sci. Rep. Tohoku Imp. Univ.**, 1934, 23: 637-664.

[99] Wassermann G. *Ueber den mechanismus der alpha-gama-umwandlung des sisens*, **Mitt.K.-Wilh-Inst. Eisenforsch.**, 1935, 17: 149-155.

[100] Pitsch W. *Der Orientierungszusammenhang zwischen Zementit und Austenit*, **Acta Metallurgica**, 1962, 10 (9): 897-900.

[101] C. Charpentier, P. Prod'homme, I. Maurin, *et al. X-Ray diffraction and Raman spectroscopy for a better understanding of ZnO:Al growth process*, **EPJ Photovoltaics**, 2011, 2: 25002-1-8.

[102] Zhang Y D, Esling C, Zhao X, *et al. Indirect two-trace method to determine a faceted low-energy interface between two crystallographically correlated crystals*, **Journal of Applied Crystallography**, 2007, 40: 436-440.

[103] M.S. Wechsler, D.S. Liberman, T.A. Read. *On the Theory of the Formation of*

*Martensite*, **Trans. AIME**, 1953, 197: 1503-1515.

[104] Wayman C M. *The phenomenological theory of martensite crystallography: Interrelationships*, **Metallurgical and Materials Transactions A**, 1994, 25 (9): 1787-1795.

[105] Cong D Y, Zhang Y D, Wang Y D, *et al. Determination of microstructure and twinning relationship between martensitic variants in 53 at.%Ni–25 at.%Mn–22 at.%Ga ferromagnetic shape memory alloy*, **Journal of Applied Crystallography**, 2006, 39 (5): 723-727.

[106] Hane K F, Shield T W. *Microstructure in the cubic to monoclinic transition in titanium-nickel shape memory alloys*, **Acta Materialia**, 1999, 47 (9): 2603-2617.

[107] Yang J H, Wayman C M. *Self-accomodation and shape memory mechanism of* $\epsilon$*-martensite — II. Theoretical considerations*, **Materials Characterization**, 1992, 28 (1): 37-47.

[108] Bhattacharya K. *Wedge-like microstructure in martensites*, **Acta Metallurgica et Materialia**, 1991, 39 (10): 2431-2444.

# List of Publications

## I. Publications in international journals

1. B. Yang, Y. D. Zhang, Z. B. Li, G. W. Qin, C. Esling, X. Zhao, L. Zuo. *Substrate constraint induced variant selection of 7M martensite in epitaxial NiMnGa thin films,* **Acta Mater.**, 2014 (under review).
2. Z. B. Li, B. Yang, Y. D. Zhang, C. Esling, N. F. Zou, X. Zhao, L. Zuo. *Crystallographic insights into the intermartensitic transformation in Ni–Mn–Ga alloys,* **Acta Mater.**, 2014, 74: 9-17.
3. B. Yang, Z. B. Li, Y. D. Zhang, G. W. Qin, C. Esling, O. Perroud, X. Zhao, L. Zuo. *Identification of Crystal Structure and Crystallographic Features of NiMnGa Thin Films by Combination of X-Ray Diffraction (XRD) and Electron Backscatter Diffraction (EBSD),* ***Materials Science Forum*** *.2014,* 783:2561-2566.
4. B. Yang, Z. B. Li, Y. D. Zhang, G. W. Qin, C. Esling, O. Perroud, X. Zhao, L. Zuo. *Microstructural features and orientation correlations of non-modulated martensite in Ni–Mn–Ga epitaxial thin films,* **Acta Mater.**, 2013, 61(18): 6809-6820.
5. J. S. Wang, B. Yang, W. L. Pei, G. W. Qin, Y. D. Zhang, C. Esling, X. Zhao, L. Zuo. *Structural and magnetic properties of* $L1_0$*-FePt/Fe exchange coupled nano-composite thin films with high energy product.* **J. Magn. Magn. Mater.** 2013, 345:165.
6. B. Yang, G. W. Qin, W. L. Pei, S. Li, Y. P. Ren, S. Ishio. *Effect of Phosphor Addition on Intergranular Exchange Coupling of Co-Pt Thin Films.* **J. Mater. Sci. Technol.** 2011, 27:398.
7. B. Yang, G. W. Qin, W. L. Pei, S. Li, Y. P. Ren, N. Xiao. *Sputtered amorphous Co-Pt-P thin films for soft underlayer of perpendicular magnetic recording.* **J. Magn. Magn. Mater.** 2010, 322:1854.
8. B. Yang, G. W. Qin, W. L. Pei, Y. P. Ren, N. Xiao, X. ZHAO, K. Oikawa, *Abnormal saturation magnetization dependency on W content for Co-W thin films,* **Acta Metallurgica Sinica(English Letters)**, 2010, 23 (1): 8-12.

## II. Contributions to International Conferences

1. B. Yang, Y. D. Zhang, Z. B. Li, G. W. Qin, C. Esling, X. Zhao, L. Zuo., *EBSD characterization of local crystallographic orientation and twin interfaces of modulated martensite in epitaxial NiMnGa thin film.* **17th International Conference on Textures of Materials (ICOTOM)**, 2014.08, Dresden, German. (**Plenary lecture**).
2. B. Yang, Y. D. Zhang, Z. B. Li, G. W. Qin, C. Esling, X. Zhao, L. Zuo., *Local crystallographic orientation of martensites in epitaxial NiMnGa thin film*. **The 7th International Conference on Technological Advances of Thin Films & Surface Coatings**, 2014.07, Chongqing, China. (**Oral presentation**)
3. B. Yang, Y. D. Zhang, Z. B. Li, G. W. Qin, C. Esling, X. Zhao, L. Zuo. *Correlate crystallographic features and microstructure of martensites in epitaxial NiMnGa thin films.* **8th international conference on Processing & Manufacturing of advanced materials (Thermec)**, 2013.12, Las Vegas, USA. (**Invited lecture**).
4. B. Yang, Y. D. Zhang, Z. B. Li, G. W. Qin, C. Esling, X. Zhao, L. Zuo. *Identification of crystal structure and crystallographic features of NiMnGa thin films by combination of x-ray diffraction (XRD) and electron backscatter diffraction (EBSD).* **French and German symposium on Textures and Anisotropy**, 2013.04, Hamburg. (**Invited lecture**).